Spring 2019

A Model Independent Measurement of the Cross Section Ratio, R_σ = σ(ν_μ n → μ^− p) / σ(ν_μ n → 2track)

Barnali Chowdhury

Recommended Citation

Chowdhury, B.(2019). *A Model Independent Measurement of the Cross Section Ratio, R_σ = σ(ν_μ n → μ^− p) / σ(ν_μ n → 2track).* (Doctoral dissertation). Retrieved from https://scholarcommons.sc.edu/etd/5326

A MODEL INDEPENDENT MEASUREMENT OF THE CROSS SECTION RATIO, $R_\sigma = \frac{\sigma(\nu_\mu n \rightarrow \mu^- p)}{\sigma(\nu_\mu n \rightarrow 2track)}$.

by

Barnali Chowdhury

Bachelor of Science
University of Calcutta, 2009

Master of Science
Florida State University, 2012

Submitted in Partial Fulfillment of the Requirements

for the Degree of Doctor of Philosophy in

Physics

College of Arts and Sciences

University of South Carolina

2019

Accepted by:

Carl Rosenfeld, Major Professor

Rick Tesarek, Major Professor

Frank Avignone, Committee Member

Steven Rodney, Committee Member

Sophya Garashchuk, Committee Member

Cheryl L. Addy, Vice Provost and Dean of the Graduate School

DEDICATION

To my grandparents, parents, Nikhil and Tandra, Bob and my brother, Tamal . . .

ACKNOWLEDGMENTS

A cluster of scientific personalities and a good number of different circumstances as well have played substantial roles in my life to culminate this moment of completion of this thesis. I take this opportunity to express my deep gratitude to all those for shaping my career as a physicist.

I would like to begin with thanking my uncle, Bob Roy Chowdhury, for steering me towards studying physics. Had he not been there I would never cherish the amazing world of physics. I am thankful to my advisers, Rick Tesarek and Carl Rosenfeld for their continuous guidance during my research work and also for their patience and motivation. Rick Tesarek, my supervisor at Fermilab, has critically taught me how with minute details of experimental techniques a nascent idea can be given a valuable worthy shape to contribute to science. This thesis would not have been possible without the countless hours of discussion and support from my advisers.

Thanks to the rest of the members of my thesis committee: Frank Avignone, Steven Rodney, Milind Purohit, Sophya Garashchuk for reviewing my yearly progress and for those questions that incited me to widen my research from various perspective. Finally I thank them for reading my dissertation and giving me their insightful comments. A special thanks to Frank Avignone, Carl Rosenfeld, Richard Creswick and Milind Purohit for standing rock solid behind me and inspiring me to overcome challenges unperturbed.

I would like to thank every single member of the NOνA collaboration for their contribution towards my graduation. I owe a lot in my learnings to Martin Frank, Gavin Davies, Kirk Bays, James Musser, Alex Himmel, Chris Backhouse, Evan Niner, Michael Baird, Keith Matera. My special gratitude goes to Ralf Ehrlich, Shih-Kai Lin, Patrick Lukens, Matt Strait, Chris Green, Paul Russo and Ting Miao for igniting thought provoking discussions and for teaching me the art of coding. Thanks to the wonderful fellow graduate students and post docs I met during my stay at Fermilab: Serdar, Nitin, José, Stefano, Shaokai, Steven, Ivan, Matt, Biswaranjan, Sijith, Rijeesh, Prabhjot, Travis, Filip, Erika, Shiqi, Daisy, Frank, Michael, Leo, Ashley, Karl and Reddy. I would not have made it to the end without their companionship.

Thanks to my fellow graduate students at the University of South Carolina, Kevin, Gary, Rasha, Katia, Nahid, Alyssa, Nick, Lei for holding my hand through the thick and thin of graduate years.

My sincere thanks go to George McNulty, a professor of Mathematics at U.Sc., for teaching me the nitty-gritty of latex in shaping up this final thesis during the last phase.

I also express my gratitude to Steffanie Schuller, Etta Johnson, Donald Grigg, Jerona Tate, Andrei Caretnic, my friends, who rejuvenate me with their deep wisdom and cheerful personality.

Above all I am ever grateful to my graceful parents and my brother for being my joy, strength, inspiration and for showering me with love unconditionally.

ABSTRACT

NOνA (NuMI Off-Axis ν_e Appearance) experiment is a long-baseline neutrino and anti-neutrino oscillation experiment, designed to study the neutrino mass ordering and to search for the effects of the CP violating phase angle δ. Extraction of the ν_μ and ν_e oscillation parameters requires knowledge of the energy of the neutrino interacting in the detector. The reactions of neutrinos with matter produce charged and neutral particles in the detector. How well we are able to measure the energy of the incoming neutrino is directly related to the final state particles, seen in the detector. Inaccurate knowledge of neutrino-nucleon interaction obscures the energy measurement of incoming neutrino. Models that predict these interactions must be tuned to match the available cross section data. Further, most cross section measurements often include one of these models in their determination of the detector acceptance and efficiency for the specific process under consideration making the cross section measurements model dependent. We present here a model independent measurement of the cross section ratio, $R_\sigma = \frac{\sigma(\nu_\mu n \to \mu^- p)}{\sigma(\nu_\mu n \to 2\text{track})}$. Using data taken from the NOνA near detector between August, 2014 and February, 2017, approximately 8800 $\nu_\mu n \to \mu^- p$ interaction and approximately 12,000 $\nu_\mu n \to$ 2track events are found. We measure $R_\sigma = 0.798 \pm 0.024$ (stat) ± 0.009 (syst). We also measure the kinematic dependence of the cross section ratio on T_μ and $\cos\theta_\mu$. These results may be used to compare various theoretical models for the above nuclear interactions and to improve the neutrino energy measurements in neutrino oscillation analyses.

TABLE OF CONTENTS

DEDICATION iii

ACKNOWLEDGMENTS iv

ABSTRACT vi

LIST OF TABLES x

LIST OF FIGURES xi

CHAPTER 1 NEUTRINOS IN THE STANDARD MODEL 1

1.1 The Weak Force 3

1.2 Neutrino Oscillation 4

1.3 Experimental Evidence for Neutrino Oscillations 12

1.4 Unknown Parameters in Neutrino Oscillations 17

1.5 Importance of Cross-section 20

1.6 Relevance of the Thesis Work 21

1.7 Chapter Summary 22

CHAPTER 2 NOνA EXPERIMENT 23

2.1 NuMI Beam 23

2.2 NOνA Detectors 29

2.3 Overview of Data Acquisition (DAQ) System 38

2.4 Near Detector Timing Peak 41

2.5 Chapter Summary 42

CHAPTER 3 RECONSTRUCTION 43

3.1 DAQ2RawDigit 44

3.2 CalHit 44

3.3 Slicer4D 45

3.4 Tracking 47

3.5 Chapter Summary 50

CHAPTER 4 CALIBRATION 51

4.1 Calibration 51

4.2 Attenuation Calibration 51

4.3 Absolute Calibration 53

4.4 Timing Calibration 55

4.5 Chapter Summary 56

CHAPTER 5 EVENT SELECTION 58

5.1 Analysis Period 58

5.2 Data Quality Cuts 59

5.3 Reconstruction and Analysis Cuts 62

5.4 Selection for Stopping Rock Muons 71

5.5 Reconstruction and Analysis Cuts for Rock Muons 71

CHAPTER 6 PARTICLE IDENTIFICATION 74
6.1 Calibration Sample from Rock Muon Data 74
6.2 Performance of MID in Confirmation Sample 78
6.3 Particle Detection using Log-likelihood 80
6.4 Chapter Summary 90

CHAPTER 7 ANALYSIS RESULT 91
7.1 Measurement of Cross-section Ratio 91
7.2 Kinematic Dependence of Cross-section Ratio 97
7.3 Systematic Uncertainties 98
7.4 Result 102
7.5 Summary 104

BIBLIOGRAPHY 108

LIST OF TABLES

Table 2.1 Hardware specifics about NOνA detectors. 38

Table 5.1 Beam Quality Spill Cuts 60

Table 5.2 Containment and Fiducial selection criteria 69

Table 7.1 Interactions that contribute to 2 tracks in the final state 92

Table 7.2 Characterizing $\mu^- p$ events. 94

Table 7.3 Related numbers on $\mu^- p$ selection. 95

Table 7.4 Characterizing $\mu^- \pi^+$ events. 95

Table 7.5 Numbers on $\mu^- \pi^+$ selection. 96

Table 7.6 Efficiencies of identified particles 97

Table 7.7 Reported is the measured cross-section ratio values for variable T_μ bins and the corresponding uncertainties. 99

Table 7.8 Reported is the measured cross-section ratio values for different $\cos\theta_\mu$ bins and the corresponding uncertainties. 100

Table 7.9 Reported is the measured cross-section ratio and the systematic uncertainties in variable bin width of T_μ. 102

Table 7.10 Reported is the measured cross-section ratio and the systematic uncertainties in variable bin width of $\cos\theta_\mu$. 103

Table 7.11 Reported is the cross-section ratio measurement in variable bin width of T_μ. 105

Table 7.12 Reported is the measured cross-section ratio in variable bin width of $\cos\theta_\mu$. 107

List of Figures

Figure 1.1 Standard Model. 1

Figure 1.2 Weak interaction three particle vertex. 3

Figure 1.3 (a) Charged current scattering of ν_e on an electron. (b) Neutral current scattering of any flavor of neutrino on an electron. 10

Figure 1.4 Neutrino flux from the Sun. 12

Figure 1.5 Flux of $\nu_{\mu,\tau}$ vs ν_e from SNO. 14

Figure 1.6 Survival probability as a function of $L/E_{\bar{\nu}}$ form the KamLAND experiment. 15

Figure 1.7 Best fit results on Δm^2_{21} and θ_{12} from the solar neutrino experiments. 16

Figure 1.8 NOνA joint fit analysis result. 17

Figure 1.9 NOνA joint fit analysis result. 18

Figure 1.10 Possible mass hierarchy scenario among 3 neutrino mass eigenstates. 19

Figure 1.11 χ^2 vs CP violation phase as measured at T2K. 20

Figure 2.1 A schematic diagram of the current Fermilab accelerator complex. 24

Figure 2.2 Diagram showing NuMI beam components. 25

Figure 2.3 Off-axis neutrino beam schematics. 26

Figure 2.4 Neutrino energy distribution as a function of parent pion energy at different off-axis angle. 28

Figure 2.5 The off-axis beam at $\theta = 14.6$ mrad results in relatively narrower energy distribution of neutrinos. 28

Figure 2.6 The diagram shows the geographical location of two NOνA detectors. 30

Figure 2.7 Cross section view of an extrusion (16 cells) in NOνA with a width of 63.5 cm and depth of 6.6 cm. 31

Figure 2.8 A side on view of an extrusion module constructed from two extrusions of a total of 32 cells, an end plate, a side seal, a manifold cover, a snout and an electronics box. 32

Figure 2.9 A schematic view of a NOνA cell, filled with liquid scintillator and a flourescent green wavelength-shifting fiber. 34

Figure 2.10 Fiber absorption and emission shape is shown as a function of wavelength. 35

Figure 2.11 An APD containing an array of 32 pixels. 35

Figure 2.12 The alternating orientation of the cells within the stacked planes of NOνA detector. 36

Figure 2.13 NOνA detectors are made up of planes, made of cells, put in alternate fashion. Two 2-D views of an event can be reconstructed from alternate planes as shown on the right hand side of the diagram. 37

Figure 2.14 NOνA detectors - Far detector and near detector. 39

Figure 2.15 A schematic of the NOνA front end electronics. 40

Figure 2.16 A cartoon of DAQ data flow. 41

Figure 2.17 Near Detector timing peak, the left plot is over the full $500\mu s$ beam window and the right one is zoomed to show the NuMI beam structure. 42

Figure 3.1 The event display of ND and FD after slicing. 46

Figure 3.2 A diagram of Cosmic tracking approach. 48

Figure 3.3 Diagram of tracking approach of 2D Kalman tracks. 49

Figure 4.1 Diagram of a tricell hit. 53

Figure 4.2 The figure shows the 2D distribution of PE/cm vs W for through going cosmic muons. 54

Figure 4.3 The diagram plots the mean PE/cm vs W profile. 55

Figure 4.4 Displayed is the corrected detector response ($PECorr/cm$) as a function of distance from the track end. 56

Figure 4.5 The plots show the distribution of $PECorr/cm$ between data and MC before and after applying absolute calibration. 57

Figure 5.1 A sketch of the orthogonal structure of the NOνA detectors. . . . 64

Figure 5.2 The figure displays the start co-ordinates of cosmic muons in the far detector. 65

Figure 5.3 The figure displays the fit parameters for various plots in Figure 5.2. 66

Figure 5.4 Near Detector containment and fiducial region in x-z view. The numbers are not representative of x and z scales. 68

Figure 5.5 Near Detector containment and fiducial region in y-z view. The numbers are not representative of y and z scales. 68

Figure 5.6 Cut progression for Data. The lines illustrate the remaining tracks after a cut. 70

Figure 5.7 Selected events / POT vs run number 71

Figure 5.8 Cut progression for Data. The lines illustrate the remaining tracks after a cut. 73

Figure 6.1 The Δt distribution for reconstructed Michel clusters. 76

Figure 6.2 The distribution of muon dE/dx for last 5 planes is shown in the figure. 78

Figure 6.3 dE/dx LL_{total} distribution for calibration sample is overlaid on that of confirmation sample. 81

Figure 6.4 The distribution shows "short track" dE/dx for different planes. . 83

Figure 6.5 Left: Presented is the diagram of LL_{total} for calibration sample. Right: The plot in red represents LL_{total} for short track data. . . 84

Figure 6.6 The left diagram displays the LL_{total} for short track sample overlaid with that of calibration sample. The right diagram showcases LL_{total} for proton. 85

Figure 6.7 The figure displays the LL_{total} of short track overlaid with that of calibration and proton sample. 86

Figure 6.8 The distribution shows “long track” dE/dx for different planes. . 87

Figure 6.9 The muon curve (black line) is scaled down to fit the long track (blue curve). The red dashed vertical line separates the muons on the right side from other candidates on the left. 88

Figure 7.1 Characterizing $\mu^- p$ events. 94

Figure 7.2 Characterizing $\mu^- \pi^+$ events. 96

Figure 7.3 The figure displays the cross-section ratio measurement as a function of muon kinetic energy in variable bin width. 99

Figure 7.4 The figure shows the cross-section ratio measurement as a function of muon cosine theta in variable bin width. 100

Figure 7.5 Shown here is the cross-section ratio measurements as a function of variable bin width of muon kinetic energy. 104

Figure 7.6 Shown here is the cross-section ratio measurement as a function of variable bin width of muon angle w.r.t. the beam axis. 106

CHAPTER 1

NEUTRINOS IN THE STANDARD MODEL

The standard model (SM) is the theory describing the elementary particles that interact through the fundamental strong, weak, and electro-magnetic forces. The basic particles and forces described by the standard model are summarized in Figure 1.1. Two kinds of particles exist in the standard model, fermions and bosons, shown in Figure 1.1. The fermions exist in two basic types called quarks and leptons. Each category contains 6 particles. The six leptons are arranged in three generations – the "electron" and the "electron neutrino", the "muon" and the "muon neutrino", and the "tau" and the "tau neutrino". The neutrinos are electrically neutral and particles of spin 1/2.

The existence of neutrinos was first postulated by Wolfgang Pauli as a "desperate remedy" to the nuclear β decay [1, 2] puzzle in 1930. He suggested an additional

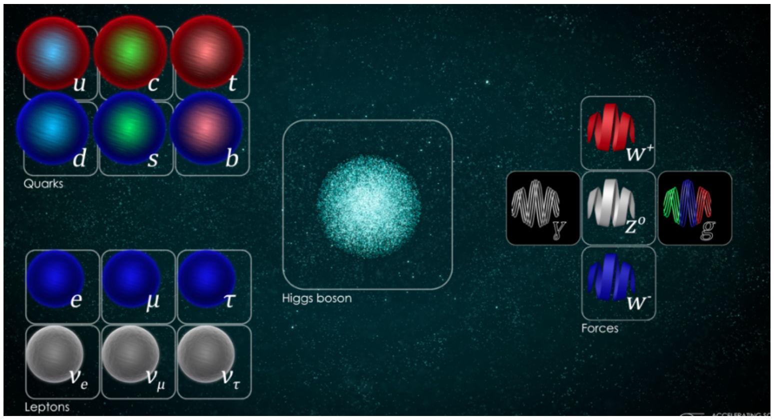

Figure 1.1 Standard Model.

neutral and extremely light particle to resolve the β decay puzzle. In 1934 Fermi proposed a formal a theory of β decay and renamed the particle suggested by Pauli as “Neutrino”. The first direct evidence for the existence of neutrinos [3] was found in the Cowan-Reines experiment in 1956. In their experiment, the source of neutrinos was β decays produced by neutron decays in a nuclear reactor through the reaction Equation 1.1. The neutrinos were detected via inverse β decay via Equation 1.2 through a characteristic signal of a pair of photons and a delayed photon from neutron capture.

$$n \to p + e^- + \bar{\nu} \tag{1.1}$$

$$\bar{\nu} + p \to n + e^+ \tag{1.2}$$

The previously observed neutrinos turned out to be what we now call electron neutrinos. At first it was the only type of neutrino believed to exist. Decades later two more flavors of neutrino were discovered . In 1962 Leon Lederman, Melvin Schwartz, and Jack Steinberger discovered the muon neutrino in an experiment at Brookhaven [4] that awarded them a Nobel Prize in 1988. Finally, in 2000, the DONUT collaboration at Fermilab reported an observation of four tau neutrinos [5]. This trio completes the set of the three standard model neutrinos.

In 1933, three years after Pauli postulated the existence of the neutrino, a particle that he feared “can not be detected”, Enrico Fermi proposed a theory of beta decay which involved the interaction of four fermions at a single point in space. One of these was a massless neutrino. Fortunately, neutrinos only proved to be elusive, but not undetectable. They were experimentally observed in inverse beta decay interactions, in an experiment led by Cowan and Reines in 1956. Experimental work over the next half century revealed that they are not massless either. In the following sections we review how neutrinos fit into the current Standard Model of particle physics,

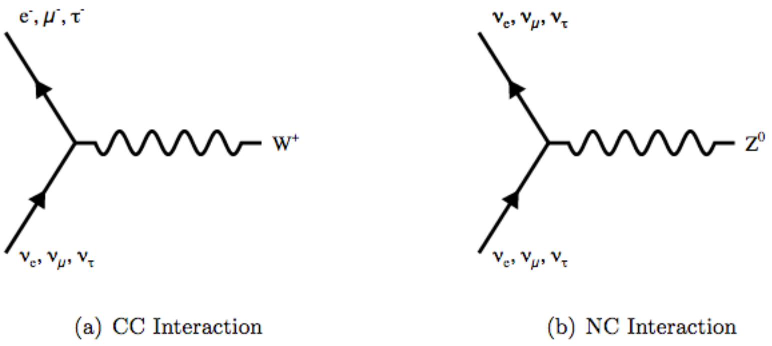

(a) CC Interaction (b) NC Interaction

Figure 1.2 Weak interaction three particle vertex.

focusing on the Electroweak sector, since leptons are altogether indifferent to the Strong interaction.

1.1 THE WEAK FORCE

There are four fundamental forces at work in the SM: the strong force, the weak force, the electromagnetic force. Neutrinos interact with matter only through the weak force. The weak force is mediated by the $W^{\pm}$ and Z^0 exchanges. Because neutrinos only interact weakly, all neutrino interactions can be categorized into charged-current (CC) interactions and neutral current (NC) interactions by the exchanges shown in the Feynman diagrams in Figure 1.2.

As shown in Figure 1.2a, a neutrino interacts with matter exchanging the $W^{\pm}$ boson and produce a charged lepton corresponding to the lepton flavour, “l”, of the incoming neutrino. Such process involving a W boson are known as charged current interactions. As shown in Figure 1.2b, a neutrino interacting with matter through the Z boson will produce a neutrino with the same lepton flavour, “l”, as the incoming neutrino. Interactions involving the Z boson are known as neutral current interactions. In CC interactions, one would typically observe a charged lepton created by the incoming neutrino and hadronic energy from the interacting nucleus.

By determining the type of the charged lepton, one can measure the flavor of the incoming neutrino. In NC interactions, outgoing neutrino would invisibly carry away much of the energy of the initial neutrino and one would only expect to see the hadronic energy resulting from the nuclear interaction.

1.2 NEUTRINO OSCILLATION

We have learned in the previous section there exist three flavors of neutrinos: electron neutrino (ν_e), muon neutrino (ν_μ) and tau neutrino (ν_τ). The SM assumes the neutrinos are massless. But if neutrinos do have mass, then a neutrino of given flavor could convert to a neutrino of a different flavor, called neutrino oscillation. In 1957, Bruno Pontecorvo first hypothesized the possibility that the neutrino oscillation could occur between electron neutrinos and electron anti-neutrinos [6]. Note only one flavor of neutrino, ν_e existed at that time. As knowledge of multiple flavors of neutrinos developed, Ziro Maki, Masami Nakagawa, and Shoichi Sakata, in 1962, described the oscillation between electron and muon flavors by extending Pontecorvo's framework for two neutrino state oscillation to three neutrinos [7].

1.2.1 **Neutrino Eigenstates**

Other than the three neutrino flavor states (mentioned earlier), a neutrino also has three mass states, $m1$, $m2$ and $m3$. These flavor and mass states are called neutrino eigen states. The flavor states and mass states are not equivalent, instead, they are superposition of each other. This means when a neutrino is created from a weak force interaction, it is created in a definite state of flavor. This definite flavor state, say ν_α, is a superposition of the mass states, ν_i and thus, can be written as a linear combination of the mass states as follows,

$$|\nu_\alpha\rangle = \sum_k U^*_{\alpha k} |\nu_k\rangle, \tag{1.3}$$

where $\alpha = e, \mu, \tau$ and $U^*_{\alpha k}$ is the 3×3 unitary matrix, since there are only three types of neutrinos discovered so far. The unitary matrix is referred to as "Pontecorvo–Maki–Nakagawa–Sakata" (PMNS) matrix [8]. This matrix describes the coupling strength between the flavor state α the mass state i. The PMNS matrix is represented as:

$$U^*_{\alpha k} = \begin{pmatrix} 1 & 0 & 0 \\ 0 & c_{23} & s_{23} \\ 0 & -s_{23} & c_{23} \end{pmatrix} \begin{pmatrix} c_{13} & 0 & s_{13}e^{-i\delta} \\ 0 & 1 & 0 \\ -s_{13}e^{-i\delta} & 0 & c_{13} \end{pmatrix} \begin{pmatrix} c_{12} & s_{12} & 0 \\ -s_{12} & c_{12} & 0 \\ 0 & 0 & 1 \end{pmatrix} \tag{1.4}$$

$$U^*_{\alpha k} = \begin{pmatrix} c_{12}c_{13} & s_{12}c_{13} & s_{13}e^{-i\delta} \\ -s_{12}c_{23} - c_{12}s_{23}s_{13}e^{i\delta} & c_{12}c_{23} - s_{12}s_{23}s_{13}e^{i\delta} & s_{23}c_{13} \\ s_{12}s_{23} - c_{12}c_{23}s_{13}e^{i\delta} & -c_{12}s_{23} - s_{12}c_{23}s_{13}e^{i\delta} & c_{12}c_{23} \end{pmatrix} \tag{1.5}$$

where $s_{ij} = \sin\theta_{ij}$ and $c_{ij} = \cos\theta_{ij}$ are the mixing angles and δ is the Dirac CP phase. The unitary matrix is described in terms of three mixing angles, $\theta_{12}, \theta_{23}, \theta_{13}$ and a CP-violating phase , δ (Dirac phase). When a neutrino travels a long distance, the superposition of mass states evolve with time (changing the relative probabilities of being found in a certain flavor state), and then interact again through the weak force, possibly yielding a different state of flavor.

1.2.2 Neutrino Oscillation Probability in Vacuum

The following derivation of the neutrino oscillation probability follows the quantum formalism from [9], [10], [11] and [12]. A neutrino produced as a flavor eigenstate can be written as ν_α(t= 0) and can be expressed as follows:

$$|\nu_\alpha(t = 0)\rangle = \sum_k U_{\alpha k} |\nu_k(0)\rangle. \tag{1.6}$$

When it travels a long distance, the superposition of mass states evolve with time. At a later time t, we can write the time evolution of flavor states as

$$|\nu_\alpha(t)\rangle = \sum_k U^*_{\alpha k} e^{-iH_k t} |\nu_k(0)\rangle, \tag{1.7}$$

where H is the Hamiltonian. From the equation above, we can see that at time t the left side does not remain same as at time $t = 0$ and this leads to a different flavor of eigenstate at time t. The flavor state α, when weakly interacts with another flavor state β, we can write

$$\langle \nu_\beta | \nu_\alpha \rangle = \sum_k U_{\beta k} U^*_{\alpha k} e^{-iH_k t}. \tag{1.8}$$

The probability of observing the neutrino in flavour state β after traveling some distance, say L and starting with an initial flavor state α, can be found by squaring the transition amplitude $\langle \nu_\beta | \nu_\alpha(t) \rangle$,

$$P_{\nu_\alpha \to \nu_\beta}(t) = |\langle \nu_\beta | \nu_\alpha(t) \rangle|^2 = \sum_{j,k} U^*_{\alpha k} U_{\beta k} e^{-i(H_k - H_j)t} U_{\alpha j} U^*_{\beta j}. \tag{1.9}$$

Using standard quantum mechanics technique we can write

$$H_k(t) = E_k t - p_k \cdot x = (E_k - p_k)L. \tag{1.10}$$

Assuming neutrinos travel at the speed of light, we can approximate x=t=L (where L is length of distance between source and detector) and $E = |p|$,

$$\Big(E_k - p_k\Big)L = \frac{E_k^2 - p_k^2}{E_k + p_k} L = \frac{m_k^2}{E_k + p_k} L \approx \frac{m_k^2}{2E} L. \tag{1.11}$$

Therefore,

$$t(H_k - H_j) \approx \frac{m_k^2 - m_j^2}{2E} \approx \frac{\Delta m_{kj}^2}{2E}, \tag{1.12}$$

where $\Delta m_{kj}^2 = m_k^2 - m_j^2$. Hence the oscillation probability in Eq.1.9 becomes

$$P_{\nu_\alpha \to \nu_\beta}(t) = \sum_{k,j} U^*_{\alpha k} U_{\beta k} U_{\alpha j} U^*_{\beta j} exp\Big(- i\frac{\Delta m_{kj}^2 L}{2E}\Big). \tag{1.13}$$

From here, we can go on to write the above expression in terms of the real and imaginary parts, expanding the exponential into sine and cosine components. Using trigonometry identities we obtain [13]:

$$\begin{aligned} P_{\nu_\alpha \to \nu_\beta}(t) = \delta_{\alpha\beta} - 4\sum_{k>j} Re\Big[U^*_{\alpha k} U_{\beta k} U_{\alpha j} U^*_{\beta j}\Big] sin^2\Big(\frac{\Delta m^2_{kj} L}{2E}\Big) \\ +2\sum_{k>j} Im\Big[U^*_{\alpha k} U_{\beta k} U_{\alpha j} U^*_{\beta j}\Big] sin^2\Big(\frac{\Delta m^2_{kj} L}{2E}\Big). \end{aligned} \tag{1.14}$$

The equation shows that the neutrino oscillation probability depends on the parameters of the PMNS matrices, the values of the mass splitting terms Δm^2_{21}, Δm^2_{31}, Δm^2_{32} and varies with the length of the baseline, L, and the energy of the neutrino beam, E. The first term in the above expression is the Kronecker delta and is only relevant if the neutrino stays in the same flavor state. For the third term, the only complex phase in the PMNS matrix is $e^{i\delta}$. if $\delta = 0$ (i.e. no CP violation), there is no imaginary part leading the third term to drop out of the equation. In that case, the second term dominates in describing oscillations between different flavors. The argument of the sinusoidal term in Equation 1.14 can be written in S.I. units as -

$$\frac{\Delta m^2_{kj} c^4 L}{4E\hbar c}. \tag{1.15}$$

Expressing L in km and E in GeV and Δm^2_{kj} in eV^2, Eq.1.15 can be written as,

$$\frac{1.27 \Delta m^2_{kj} L}{E}. \tag{1.16}$$

Therefore, Eq.1.17 can be written as,

$$\begin{aligned} P_{\nu_\alpha \to \nu_\beta}(t) = \delta_{\alpha\beta} - 4\sum_{k>j} Re\Big[U^*_{\alpha k} U_{\beta k} U_{\alpha j} U^*_{\beta j}\Big] sin^2\Big(\frac{1.27\Delta m^2_{kj} L}{E}\Big) \\ +2\sum_{k>j} Im\Big[U^*_{\alpha k} U_{\beta k} U_{\alpha j} U^*_{\beta j}\Big] sin^2\Big(\frac{1.27\Delta m^2_{kj} L}{E}\Big). \end{aligned} \tag{1.17}$$

1.2.3 Two Flavor Neutrino Approximation

For most of the ongoing long baseline neutrino experiments, one need not consider the full effect of three neutrino flavor mixing, but instead can consider the approximation of two neutrino mixing. Ignoring the relatively smaller term in Equation 1.17 for $\alpha = \beta$, we can write

$$P_{\nu_\mu \to \nu_\mu}(t) \approx 1 - 4 \sum_{k>j} |U_{\mu k}|^2 |U_{\mu j}|^2 \sin^2\left(\frac{1.27 \Delta m_{kj}^2 L}{E}\right). \tag{1.18}$$

Equation 1.18 is the survival probability for a muon neutrino of energy E after traveling a distance of L km.

If neutrinos had only two flavor states and two mass states, we could write two flavor approximation by considering $\theta_{13} = 0$. For the long baseline experiment of ratio of order L/E $\sim$ 500, we can approximate sinusoidal term with $\Delta m_{21}^2 \sim 0$ and $\Delta m_{31}^2 \sim \Delta m_{32}^2 = \Delta m_{atm}^2$. Equation 1.18 now takes the form:

$$P_{\nu_\mu \to \nu_\mu} \approx 1 - \sin^2 2\theta_{23} \sin^2\left(\frac{1.27 \Delta m_{atm}^2 L}{E}\right). \tag{1.19}$$

The above equation is a two flavor neutrino oscillation probability. Long baseline experiments like MINOS [14], T2K[15] and NOνA [16] are sensitive to the following appearance and disappearance channels. The appearance probability for two flavor approximation follows :

$$\begin{aligned} P_{\nu_\mu \to \nu_e} &\approx 1 - 4|U_{\mu 3}|^2 |U_{\mu 3}|^2 \sin^2\left(\frac{1.27 \Delta m_{32}^2 L}{E}\right), \\ &\approx \sin^2 2\theta_{13} \sin^2 \theta_{23} \sin^2\left(\frac{1.27 \Delta m_{32}^2 L}{E}\right). \end{aligned} \tag{1.20}$$

and the disappearance probability follows :

$$\begin{aligned} P_{\nu_\mu \to \nu_\mu} &\approx 1 - 4|1 - U_{\mu 3}|^2 |U_{\mu 3}|^2 \sin^2\left(\frac{1.27 \Delta m_{32}^2 L}{E}\right), \\ &\approx 1 - \cos^2 2\theta_{13} \sin^2 \theta_{23} \sin^2\left(\frac{1.27 \Delta m_{32}^2 L}{E}\right). \end{aligned} \tag{1.21}$$

The reactor based neutrino oscillation experiments like Daya Bay [17, 18], Double Chooz [19] and RENO [20] are sensitive to following disappearance channel:

$$\begin{aligned} P_{\nu_e \to \nu_e} &\approx 1 - 4|U_{e3}|^2 |1 - U_{e3}|^2 \sin^2\left(\frac{1.27\Delta m_{32}^2 L}{E}\right), \\ &\approx 1 - \sin^2\theta_{13} \sin^2\left(\frac{1.27\Delta m_{32}^2 L}{E}\right). \end{aligned} \tag{1.22}$$

1.2.4 **Matter Effect**

Neutrinos propagating through matter experience the weak force through coherent and incoherent forward scattering. The amount of incoherent scattering is negligible due to very long mean free path of interaction in the Earth, so it can be safely ignored. Ordinary matter is partially composed of electrons but not muons or taus. So neutrinos $(\nu_e, \nu_\mu, \nu_\tau)$ interact with matter via neutral currents and not through charge current reaction. However, only ν_e can interact with medium via charged current interactions. Figure 1.3 shows the Feynman diagrams for charged current (left) and neutral current (right) scattering of neutrinos on electrons. Neutral current interactions with matter are independent of any particular flavor of neutrino, so do not affect neutrino oscillation probabilities. But the charged current interactions in the ordinary matter is only caused by electron neutrinos. This additional scattering amplitude causes neutrino oscillations to have different probabilities relative to neutrino oscillation in vacuum [21, 22].

In the case of two-neutrino mixing, the mixing angle in vacuum is replaced by an effective angle in matter. The amount of change in the mixing angle depends on matter density. For certain densities, even a small mixing angle in vacuum, the effective mixing angle can become maximal in matter. This is called as MSW effect after the authors of the theory Mikheev, Smirnov and Wolfenstein [23].

Due to NC and CC interactions, the vacuum Hamiltonian gets modified by the fol-

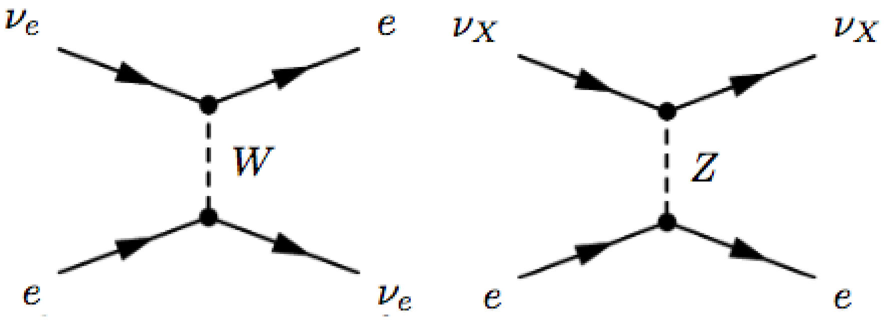

(a) (b)

Figure 1.3 (a) Charged current scattering of ν_e on an electron. (b) Neutral current scattering of any flavor of neutrino on an electron.

lowing terms [23],

$$\begin{aligned} V_{NC} &= -G_F N_n/\sqrt{2} \\ V_{CC} &= G_F N_e/\sqrt{2}, \end{aligned} \tag{1.23}$$

where N_n and N_e represent the neutron and electron density respectively inside the Earth.

In the case of two flavor mixing, the evolution equation for neutrino mass eigenstate can we written as,

$$i\frac{d}{dt}\begin{pmatrix} \nu_1(t) \\ \nu_2(t) \end{pmatrix} = H \begin{pmatrix} \nu_1(t) \\ \nu_2(t) \end{pmatrix}, \tag{1.24}$$

where the Hamiltonian can be written as follows, since, $E \approx |p| + \frac{m^2}{2|p|}$,

$$H = \begin{pmatrix} E_1 & 0 \\ 0 & E_2 \end{pmatrix} \approx |p| + \begin{pmatrix} \frac{m_1^2}{2|p|} & 0 \\ 0 & \frac{m_2^2}{2|p|} \end{pmatrix}. \tag{1.25}$$

Converting it to the mass eigenbasis by using $H_f = UHU^\dagger$, where U is

$$U = \begin{pmatrix} \cos\theta & \sin\theta \\ -\sin\theta & \cos\theta \end{pmatrix} \tag{1.26}$$

and

$$H = |p| + \frac{m_1^2 + m_2^2}{4p} + \frac{\Delta m_{21}^2}{4|p|} \begin{pmatrix} \cos 2\theta & \sin 2\theta \\ -\sin 2\theta & \cos 2\theta \end{pmatrix}. \tag{1.27}$$

The diagonalizing angle is given by

$$\tan 2\theta = \frac{2H_{f12}}{H_{f22} - H_{f11}}. \tag{1.28}$$

With the effect of MSW, H in Equation 1.27 becomes,

$$H = |p| + \frac{m_1^2 + m_2^2}{4p} - \frac{1}{\sqrt{2}} G_F N_n + \begin{pmatrix} -\frac{\Delta m_{21}^2}{4|p|} \cos 2\theta + \sqrt{2} G_F N_e & \frac{\Delta m_{21}^2}{4|p|} \sin 2\theta \\ \frac{\Delta m_{21}^2}{4|p|} \sin 2\theta & \frac{\Delta m_{21}^2}{4|p|} \cos 2\theta \end{pmatrix}, \tag{1.29}$$

where $\frac{1}{\sqrt{2}} G_F N_n$ and $\sqrt{2} G_F N_e$ are from the NC and CC contributionsrespectively. The NC term is written out of the matrix as it is common to all types of neutrinos. However, due to absence of μ, τ in matter, CC term is written with M_{11} entry, as only electron can have this interaction. The diagonalizing angle in this case is,

$$\tan 2\theta_M = \frac{\Delta m_{21}^2 \sin 2\theta}{\Delta m_{21}^2 \cos 2\theta - A}, \tag{1.30}$$

where $A = 2\sqrt{2} G_F N_e E$ and E is the neutrino energy. From the above equation if,

$$\begin{aligned} A &= \Delta m_{21}^2 \cos 2\theta \\ \implies 2\sqrt{2} G_F N_e E &= \Delta m_{21}^2 \cos 2\theta \\ \implies N_e &= \frac{\Delta m_{21}^2 \cos 2\theta}{2\sqrt{2} G_F E} \end{aligned} \tag{1.31}$$

From the equations above, we see that matter effects modify the terms $\sin(\Delta_{31})$ and $\sin(\Delta_{21})$. For the normal ordering, matter effect enhances the appearance probability $\nu_\mu \to \nu_e$ but suppresses the $\bar{\nu}_\mu \to \bar{\nu}_e$. For the inverted ordering the result of the matter effect is opposite. This opposite consequence of matter effect helps to disentangle the CP violation.

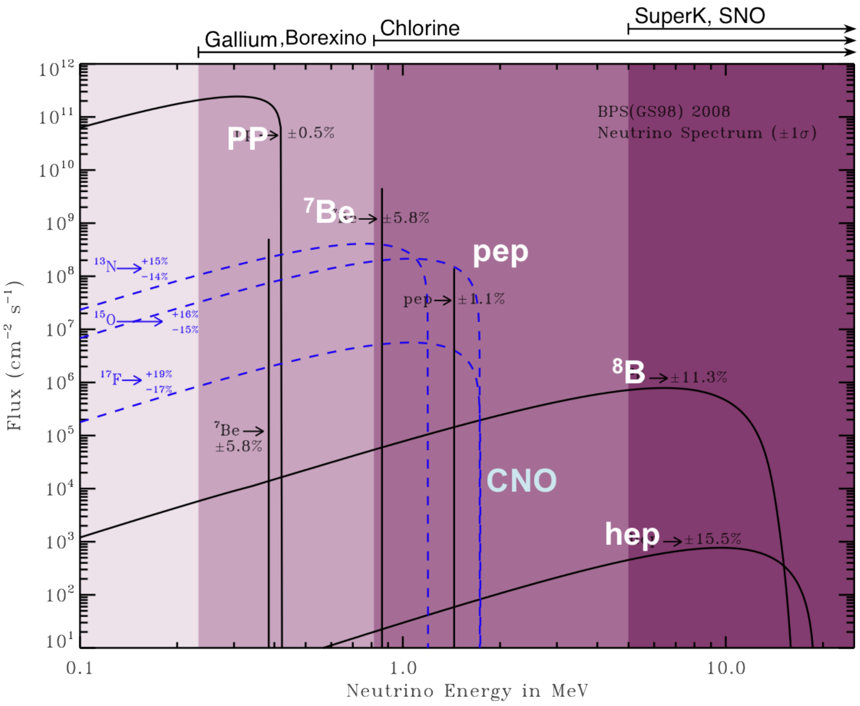

Figure 1.4 Neutrino flux from the Sun.

This figure was taken from [24].

1.3 Experimental Evidence for Neutrino Oscillations

1.3.1 Oscillation Parameters from Solar Neutrinos

The Sun is a great source of neutrinos. It produces a large number of electron flavored neutrinos through the nuclear chain reactions that occur in the core of the Sun. Figure 1.4 shows the flux of neutrinos produced inside the Sun through various fusion reactions [24]. The energy spectrum of those neutrinos depends on the various factors of the Sun and lies in the 0.1 - 10 MeV range [25]. These factors were studied in detail by Bahcall and collaborators in the Standard Solar Model (SSM) [26]. The model predicts a solar neutrino spectrum that can be observed on earth.

There were several experiments designed to detect solar neutrinos. The first experiment was performed by Raymond Davis Jr. and collaborators in an experiment at the Homestake Mine in South Dakota to detect solar neutrinos [27]. The experiment was based on the following reaction,

$$\nu_e +^{37} Cl \rightarrow^{37} Ar + e^- \quad (E_{th} = 0.814\ MeV). \tag{1.32}$$

Due to the reaction threshold, the experiment was sensitive only to the neutrinos produced in proton-proton interaction in the SSM,

$$^8B \rightarrow^8 B^* + e^+ + \nu_e(E_{th} =\sim 10\ MeV). \tag{1.33}$$

A series of other experiments during 1990s, like SAGE [28] and GALLEX, GNO [29] measured the rate of solar neutrinos produced in p-p reaction. In 1996, physicists in Japan performed the Kamiokande [30] experiment using water Cherenkov detectors. The experiment measured the elastic neutrino scattering on electrons.

$$\nu_e + e^- \rightarrow \nu_e + e^-(E_{th} \sim 5\ MeV). \tag{1.34}$$

All of the neutrino experiments above have consistently measured a neutrino flux significantly below the SSM prediction. The rate of solar neutrinos were found to be within 1/3 of the expected rate as predicted by Solar Standard Model (SSM) [26]. This deficit in observed solar neutrinos was termed as Solar Neutrino Anomaly [31].

In 2001, the solar neutrino anomaly was resolved by the Sudbury Neutrino Observatory (SNO) experiment [32]. SNO measured the neutrino flux through different channels, as shown below, with the sensitivity for all kind of neutrino fluxes.

$$\begin{aligned} \nu_e + d \rightarrow p + p + e^- \quad (CC,\ E_{th} > 5\ MeV). \\ \nu_x + d \rightarrow p + n + \nu_x \quad x = e, \mu, \tau \quad (NC,\ E_{th} > 2.2\ MeV). \end{aligned} \tag{1.35}$$

As discussed in section 1.2.4, CC reaction is only sensitive to the electron neutrinos and NC is sensitive to all neutrino flavors. This sensitivity to ν_e charged current

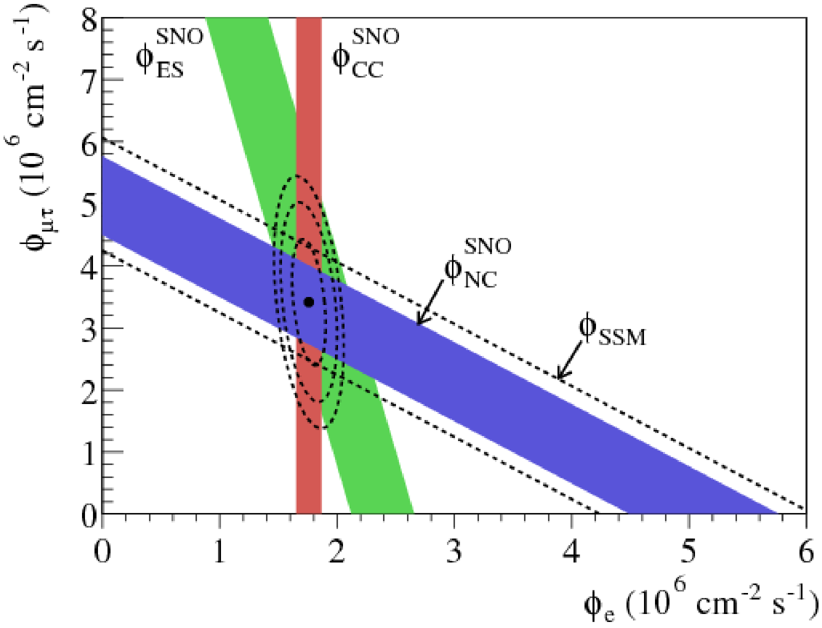

Figure 1.5 Flux of $\nu_{\mu,\tau}$ vs ν_e from SNO.

The dashed line shows the SSM prediction which is in complete agreement with the neutrino flux (blue band) measured with the NC [33].

interaction enabled SNO to measure the electron flavored neutrinos alone. The flavor transition in the solar neutrinos is shown in Figure 1.5.

In 2002, the reactor neutrino experiment, KamLAND, measured the reactor neutrinos ($\bar{\nu}_e$) coming from the nuclear reactor [34]. The neutrinos were detected via inverse β decay:

$$\bar{\nu}_e + p \to e^+ + n \quad (E_{th} > 2.6\ MeV). \tag{1.36}$$

The experiment measured the survival probability of $\bar{\nu}_e$. Figure 1.6 shows the survival probability as a function of $L/E_{\bar{\nu}}$. The figure clearly shows that the neutrinos oscillate. This experiment confirmed the solar neutrino oscillations measured by SNO.

The combined fit (Fig.1.7) of current data from the solar neutrino experiments

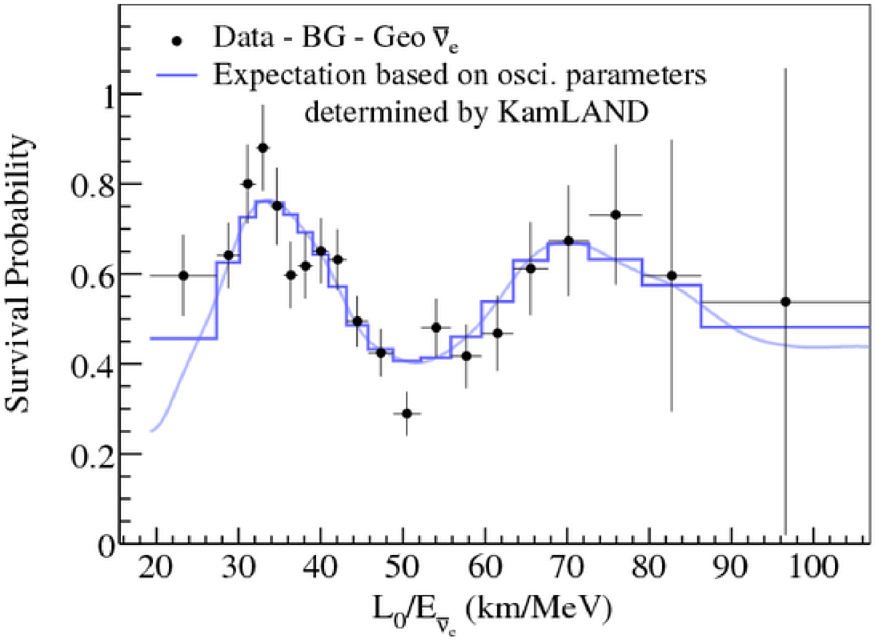

Figure 1.6 Survival probability as a function of $L/E_{\bar{\nu}}$ form the KamLAND experiment.

The experimental data points are in good agreement with the theoretical predictions based on neutrino oscillations [34].

result in the best fit oscillation parameters:

$$\Delta m^2_{21} = 7.54^{+0.26}_{-0.22} \times 10^{-5} eV^2, \quad \tan^2\theta_{12} = 0.307^{+0.018}_{-0.016}, \quad m_2 > m_1.$$

These results mean that the mass eigenstate ν_1 is about 2/3 of ν_e and ν_2 is approximately 1/3 of ν_e.

1.3.2 Oscillation Parameters from Atmospheric Neutrinos

In atmosphere, neutrinos are produced in the collision of cosmic rays with nuclei (air molecule) in the atmosphere. The collision produces secondary particles, mostly pions [35]. Pion decays to a muon and a muon neutrino. The muon subsequently decays to a positron, a muon anti-neutrino and an electron neutrino, shown in the decay chain below. From this decay chain, it is clear that the ratio of ν_μ to ν_e is 2:1.

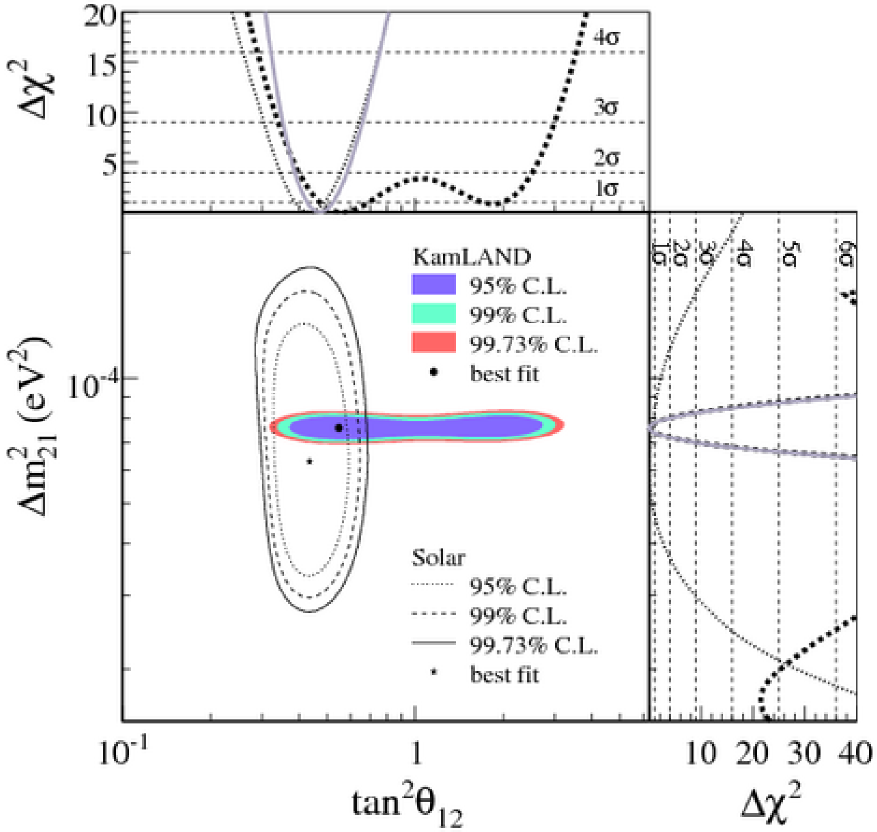

Figure 1.7 Best fit results on Δm^2_{21} and θ_{12} from the solar neutrino experiments.

Results from KamLAND experiment are included [34] in the Figure.

$$\pi^+ \to \mu^+ + \nu_\mu \ , \qquad \mu^+ \to e^+ + \nu_e + \bar{\nu}_\mu . \tag{1.37}$$

Super Kamiokande (SK) experiment measured the neutrino flux coming from the atmosphere. The collaboration measured the ν_μCC and ν_e CC interactions as a function of the zenith angle. They observed that the rate of ν_μCC interactions due to neutrinos coming from below ($\cos_\theta = -1$) is significantly lower than the rate of those coming from above. The interpretation was understood as the disappearance of ν_μ as the neutrinos pass through the matter coming from the other side of the earth. This

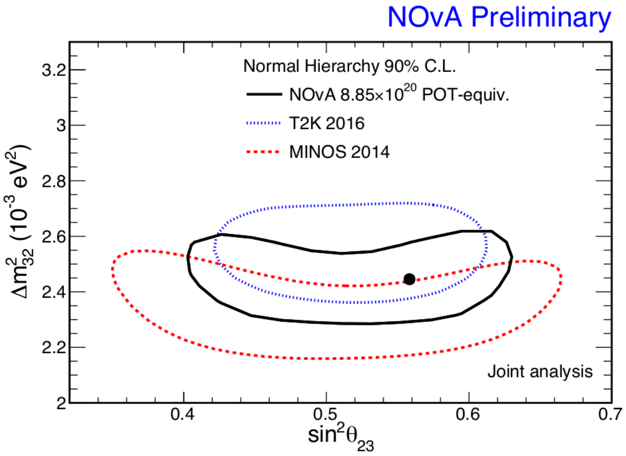

Figure 1.8 NOνA joint fit analysis result.

The result is consistent with the measurements other experiments. Taken from [36].

phenomenon is predominantly due to $\nu_\mu \rightarrow \nu_\tau$ transition.

Measurements of atmospheric muon neutrino disappearance are sensitive to $|\Delta m^2_{32}|$ and $\sin^2 2\theta_{23}$. Figure 1.8 and Figure 1.9 show the latest results of $|\Delta m^2_{32}|$ and $\sin^2 2\theta_{23}$ from NOνA [36]. The upper octant is preferred at 0.2σ and the best fit values are found as shown below in Equation 1.38.

$$\begin{aligned} |\Delta m^2_{32}| &= 2.444^{+0.079}_{-0.077} \times 10^{-3} eV^2 \\ \sin^2\theta_{23} &= 0.558^{+0.041}_{-0.033}, \quad \mathit{Upper\ octant} \\ \sin^2\theta_{23} &= 0.475^{+0.036}_{-0.044}, \quad \mathit{Lower\ octant} \end{aligned} \tag{1.38}$$

1.4 UNKNOWN PARAMETERS IN NEUTRINO OSCILLATIONS

1.4.1 **Mass Hierarchy**

So far scillation experiments have not been able to resolve the sign of the mass square differences, Δm^2_{32} and Δm^2_{31}. As a result, the mass hierarchy of the neutrino mass

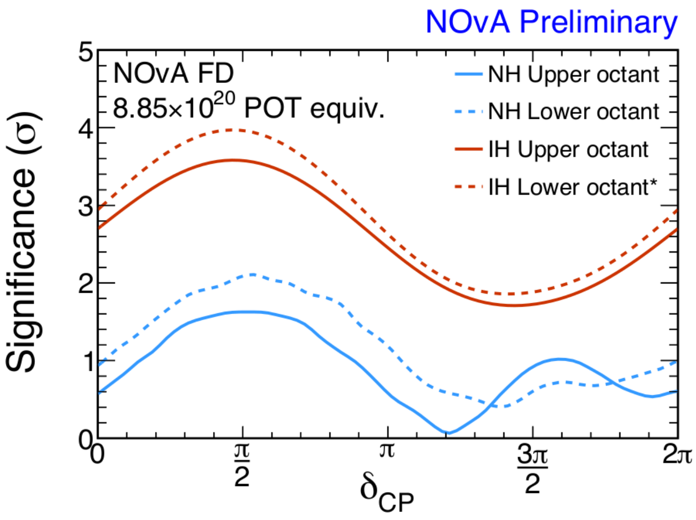

Figure 1.9 NOνA joint fit analysis result.

The IH at $\delta_{CP} = \pi/2$ is disfavored at greater than 3σ. Taken from [36].

eigenstates is yet unknown. To determine whether it is normal hierarchy or inverted (shown in Figure 1.10), future experiments have to be sensitive to the matter effect. Future experiments like DUNE, INO and HyperK are being designed with the goal to resolve the mass hierarchy.

1.4.2 CP Violation

The CP symmetry arises from the complex phase, δ, in thePMNS matrix. If CP is violated, we will have $P(\nu_\alpha \to \nu_\beta) \neq P(\bar{\nu_\alpha} \to \bar{\nu_\beta})$ for $\alpha \neq \beta$. Thus CP violation can be measured in terms of asymmetry A.

$$A_{CP}^{(\alpha,\beta)} = P(\nu_\alpha \to \nu_\beta) - P(\bar{\nu_\alpha} \to \bar{\nu_\beta}). \tag{1.39}$$

Writing the probabilities in Equation 1.39, we get

$$\begin{aligned} P(\nu_\alpha \to \nu_\beta) - P(\bar{\nu}_\alpha - \bar{\nu}_\beta) \quad &= 4\textstyle\sum_{j>k} Im(U^*_{\beta j}U_{\beta k}U_{\alpha j}U^*_{\beta k}) \sin\left(\frac{\Delta m^2_{jk}L}{2E}\right); \\ &\propto \sin\delta, \end{aligned} \tag{1.40}$$

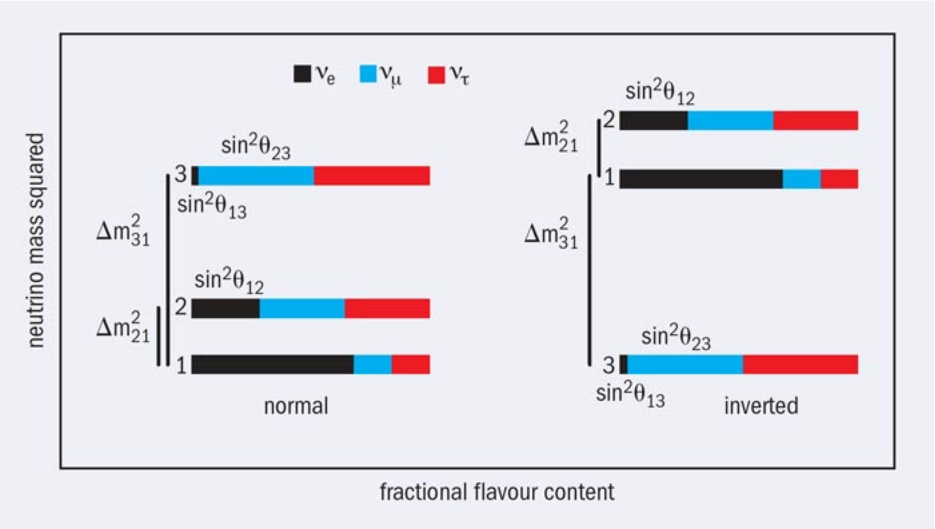

Figure 1.10 Possible mass hierarchy scenario among 3 neutrino mass eigenstates.

where δ is the Dirac phase in the PMNS matrix. The size of the difference between the neutrino and anti-neutrino oscillation probabilities can be obtained from the Equation above. The T2K experiment has given a hint of CP violation, shown in Figure 1.11, in the neutrino sector. Future experiments, such as DUNE and HyperK, are designed to potentially observe the CP violation.

1.4.3 θ_{23} Octant

Whether θ_{23} is $< \pi/4$ or $> \pi/4$ is yet unknown though the current measurements of θ_{23} are consistent with 45°. The precise value of θ_{23} is very important in knowing the admixture of ν_3 mass eigenstate. If $\theta_{23} = 45°$, all mass states will contain contains equal mixture of ν_μ and ν_τ flavor eigenstates. This might indicate a new symmetry [37] in the neutrino sector that has not yet been considered. This scenario is known as maximal mixing.

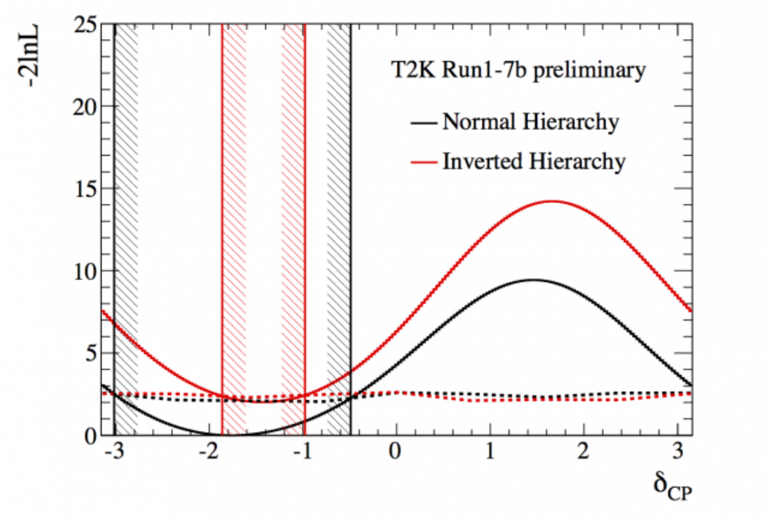

Figure 1.11 χ^2 vs CP violation phase as measured at T2K.

1.5 IMPORTANCE OF CROSS-SECTION

To probe the important questions of neutrino physics (described in section 1.4), yet unknown, the neutrino experiments have entered into the precision era. Neutrino oscillation experiments determine the oscillation probability by measuring the neutrino event rate. So we need to measure the number of neutrinos as a function of neutrino energy in the near and far detector. The number of neutrino events (N) at any detector, in general, can be written as,

$$N_{\nu_\alpha}^{\text{detector}}(E_\nu) \propto \Phi(E_\nu) \times \sigma(E_\nu) \times \epsilon^{\text{detector}}(E_\nu), \tag{1.41}$$

where $\Phi(E_\nu)$ is the number of neutrinos produced by the accelerator per energy per cm^2 for a given number of protons on target, $\sigma(E_\nu)$ is the cross-section of an interaction under consideration and $\Phi(E_\nu)$ is the detector efficiency. To determine the number of neutrinos interacting in a detector, one must understand the $\sigma(E_\nu)$ i.e. what happens when a neutrino interacts inside of a nucleus. This requires us to have an accurate knowledge of neutrino-nucleus interaction. Different neutrino-nucleus interaction model predicts different particle multiplicity in the final state giving rise to uncertainty in the measurement. This uncertainty, in turn, may introduce error in calculating the total number of neutrino events in a detector. This boils down to a point of better understanding the cross section. Thus measuring neutrino cross sections precisely are an essential ingredient in all neutrino experiments. Also the $\epsilon^{\text{detector}}(E_\nu)$ in Equation 1.41 depends on the kinematics of the final state observables in the detector, which is driven by cross-section.

1.6 Relevance of the Thesis Work

Extraction of the ν_μ and ν_e oscillation parameters in my experiment, NOνA (NuMI Off-Axis ν_e Appearance), requires knowledge of the energy of the neutrino interacting in the detector. The reactions of neutrinos with matter produce charged and neutral particles in the detector. How well we are able to measure the energy of the incoming neutrino, is directly related to the the final state particles seen in the detector. Inaccurate knowledge of neutrino-nucleon interaction obscures this energy measurement of incoming neutrino. Models that predict these interactions must be tuned to match the available cross section data. Further, most cross section measurements often include only one of these models in their determination of the detector acceptance and efficiency for the specific process under consideration making the cross section measurements model dependent. The thesis performs a model independent measurement of the cross section ratio, $R_\sigma = \frac{\sigma(\nu_\mu n \rightarrow \mu^- p)}{\sigma(\nu_\mu n \rightarrow 2track)}$. Furthermore, the thesis also determines the kinematic dependence of the cross section ratio on T_μ and $\cos\theta_\mu$. These results may be used to compare various theoretical models for the above nuclear interactions and to improve the neutrino energy measurements in neutrino oscillation analyses.

1.7 CHAPTER SUMMARY

Several important questions of neutrino physics that still need to be answered by current and ongoing neutrino experiments are :

- What is the absolute mass scale of neutrino?
- What is the mass hierarchy?
- What is the δ-CP phase ?
- What is the octant of θ_{23}?
- What is the type of neutrinos, Dirac or Majorana?
- Are there any sterile neutrinos?

This chapter introduces the theory of neutrino oscillation followed by an overview of the recent measurement of the neutrino oscillation parameters. The chapter also includes a short discussion on the importance of cross-section measurement and how the measurement is incorporated in the current picture of neutrino oscillations.

CHAPTER 2

NOνA EXPERIMENT

The NuMI Off-axis ν_e Appearance (NOνA) experiment is designed to make precise measurements of muon neutrino (anti-neutrino) disappearance and electron neutrino (anti-neutrino) appearance using the Neutrinos at the Main Injector (NuMI) beam at Fermilab. The NOvA experiment consists of two detectors, near (ND) and far (FD). The experiment uses FD to measure an oscillated spectrum when ND data is used to constrain systematic uncertainties in the predicted FD spectrum. The experiment is made up of two main components, a beam of neutrinos described in section 2.1 and the detectors used to measure neutrino interactions described in section 2.2. Finally section 2.3 and 2.4 describe the readout electronics and timing system in the context of the NOvA experiment.

2.1 NUMI BEAM

NOνA is an accelerator-based oscillation experiment, so a high intensity neutrino beam is essential to run the experiment. There are three principal beams produced at the Fermilab accelerator campus for several medium-energy and high-intensity experiments. NOνA makes use of Neutrinos at the Main Injector (NuMI) beamline as its neutrino source. We will briefly describe here the process by which the NuMI beam is created. Further details are in [38].

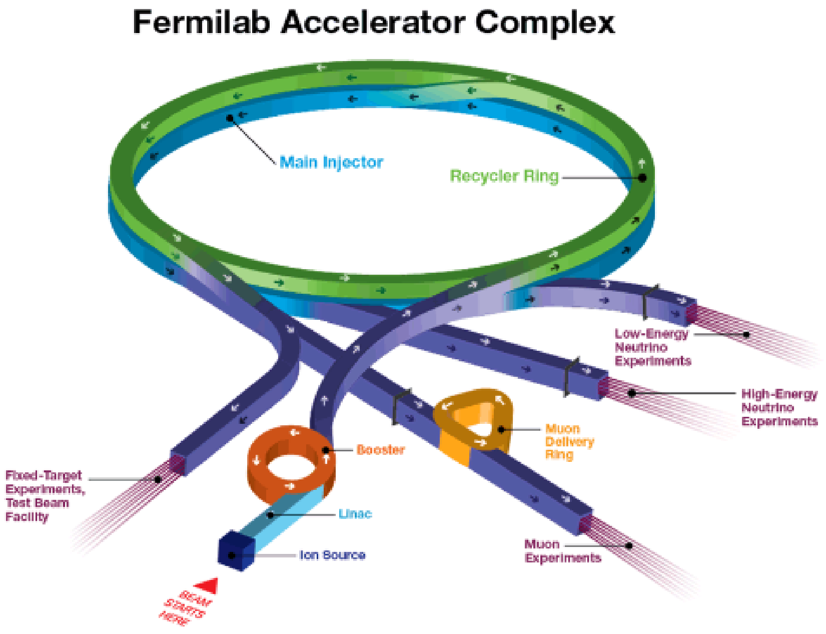

Figure 2.1 A schematic diagram of the current Fermilab accelerator complex.

Graphic is courtesy of Fermilab, http://www.fnal.gov/pub/science.

2.1.1 The Main Injector

A schematic of Fermilab accelerator complex and the NuMI beam facility is presented in Figure 2.1. The figure portrays different components of the facility that will be mentioned in this section. The origin of the beam is H^- ions that get accelerated to 400 MeV in the linac. The electrons are stripped off the ion and the protons are fed to the booster ring, which accelerates the proton beam to 8 GeV. The beam in the booster is bunched and segmented to produce batches of $\sim$ 4 x 10^{12} protons. Six batches, with 4 x 10^{12} protons each, are injected one after another from the Booster to the Recycler ring. These proton batches are fed into recycler using a slip-stacking method where six successive booster batches are injected in a train followed by six more in a different orbit [39]. The slip-stacking process doubles the number of protons in all six batches. The intensity of six batches now achieve approximately 4.8 x 10^{13} protons. Next the batches are delivered to the Main Injector (MI) ring where the protons get accelerated to 120 GeV. The NuMI beam-line extracts six batches of approximately 4.8 x 10^{13} 120 GeV protons from the Main injector. We refer each extraction of protons a neutrino spill. The MI injection and acceleration cycle takes 1.33 seconds, that typically makes an interval of 1.33 s and each neutrino spill has a time span of 10 μs with a structure of six batches inside.

2.1.2 Focusing Horns and The NuMI Beamline

Upon exiting the main injector, the beam spill is directed to the NuMI target hall. The target consists of a series of 48 graphite fins, each 24 mm long, with a small gap between consecutive fins. The total target length is 1.2 m [40], 2 pion interaction lengths. The collisions between the accelerated protons and the target produce a secondary meson beam. The meson beam is primarily composed of $\pi^{\pm}$ with a contamination of $K\pm$ and K_L.

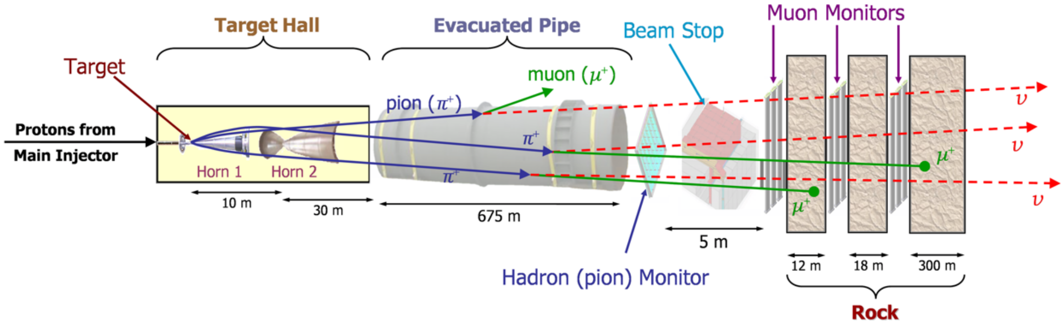

Figure 2.2 Diagram showing NuMI beam components.

The cartoon of the beam components is taken from [41].

The charged mesons produced are then focused towards the decay pipe using two magnetic horns placed downstream of the end of the target. The inner conductors of horns are parabolic in shape. The horns act as a lens with the focal length proportional to the momentum of the pion. The current through the horns is 200 kA. Changing the current direction within the focusing horns changes the direction of the magnetic field and therefore the sign of the mesons that are focused. Operating the horns with forward or reverse horn current focus positively or negatively charged mesons respectively. Downstream of the horns is a 675 m decay pipe. The resulting beam of charged mesons then enters the decay pipe filled with 0.9 atm helium. In the decay pipe, the positively and negatively charged mesons decay predominantly to neutrinos (ν_μ) or anti neutrinos ($\bar{\nu}_\mu$) respectively through the following decay modes:

$$\begin{aligned} \pi^+ &\to \mu^+ + \nu_\mu; \qquad \pi^- \to \mu^- + \bar{\nu}_\mu \quad (BR.\ 99.98\%), \\ K^+ &\to \mu^+ + \nu_\mu; \qquad K^- \to \mu^- + \bar{\nu}_\mu \quad (BR.\ 63.55\%). \end{aligned} \tag{2.1}$$

The beam then passes through the hadron monitor, the beam absorber, muon monitors and about 240 meters of rock. This is to to absorb any remaining muons, hadrons, and charged particles to leave a pure neutrino/anti neutrino beam. After the rock, the beam arrives at the NOνA near detector before it continues traveling through the Earth's crust for 810 km to reach the NOνA far detector. A cartoon illustrating all the previous stages of the NuMI beamline is shown in Figure 2.2.

2.1.3 **Off-axis Experiment Design**

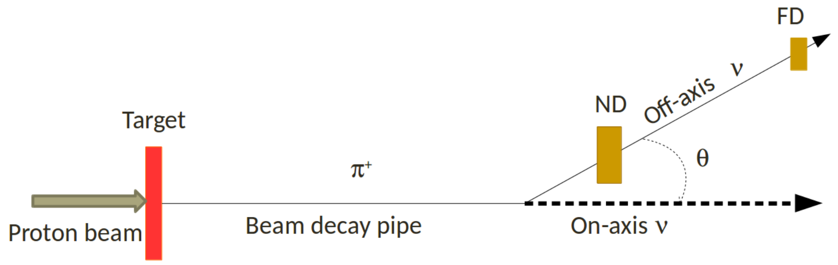

Figure 2.3 Off-axis neutrino beam schematics.

The detectors for the current generation of long baseline accelerator based neutrino oscillation experiments are located slightly off the center of the neutrino beam axis, shown in Figure 2.3. For NOvA, both the detectors are at 14 mrads off-axis of the NuMI beam as displayed in Figure 2.3. This choice comes from the analysis of Lorentz boosted decay kinematics of the $\pi\pm/K\pm$ that produces neutrino beam. We will take a short overview of the decay kinematics of the dominant mode $\pi^{\pm} \rightarrow \mu^{+} + \nu_{\mu}$ and how the decay shapes the choice of off axis.

This two-body decay process occurs isotropically producing mono-energetic neutrinos in the rest frame of pion. The neutrino energy in the COM frame can be calculated by the four momentum of the involved particles. When boosted into the lab frame the parent particle $\pi^{\pm}$ is not at rest and muons and neutrinos travel in the direction of the parent particle. In the lab frame the energy of the neutrino produced by pion decay (E_{ν}) is given by

$$E_{\nu} = \frac{(0.43)E_{\pi}}{1+\gamma^{2}\theta^{2}}, \tag{2.2}$$

where E_{π} and m_{π} are the energy and the mass of the parent pion, $\gamma = E_{\pi}/m_{\pi}$ and θ denotes the angle between the pion and outgoing neutrino direction. For $\theta = 0$, i.e. on-axis neutrinos, $E_{\nu} \propto E_{\pi}$, causing the E_{ν} distribution to be as broad as E_{π} distribution that comes out of magnetic horns. For non zero values of θ, E_{ν} falls off for very large values of E_{π}. Figure 2.4 shows the E_{π} spectrum for four off-axis angles ($\theta = 0$ mrads, $\theta = 7$ mrads, $\theta = 14.6$ mrads and $\theta = 21$ mrads). The plot also shows with the increase of off-axis angle the E_{ν} spectrum is almost horizontal with respect to pion energy causing the neutrino energy not to have strong dependence on the parent pion energy. In addition Figure 2.5 shows that at 14 mrad, the beam configuration produces a narrow energy neutrino beam peaked at 2 GeV with approximately 4 times more neutrinos than on-axis scenario. The combination of neutrino energy and baseline length for the FD means that the ν_{μ} is at oscillation minimum.

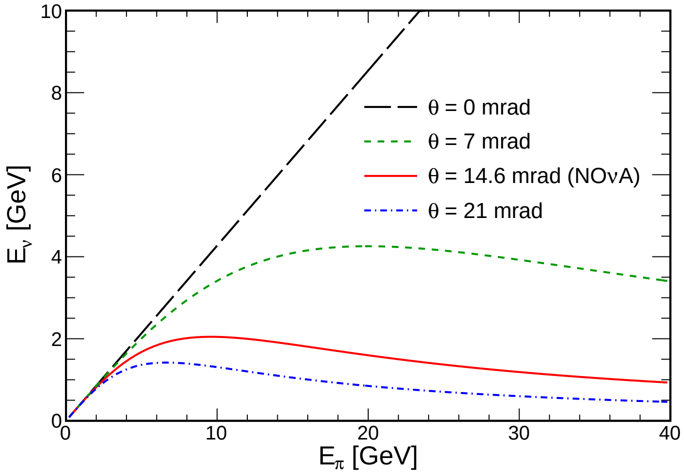

Figure 2.4 Neutrino energy distribution as a function of parent pion energy at different off-axis angle.

The figure is taken from [42].

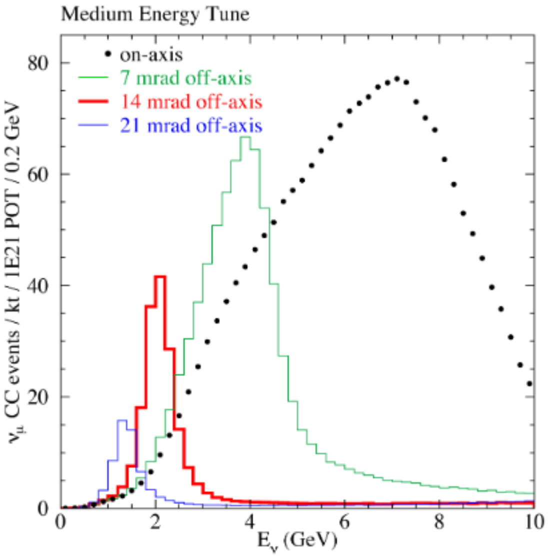

Figure 2.5 The off-axis beam at $\theta =$ 14.6 mrad results in relatively narrower energy distribution of neutrinos.

The figure is taken from [42].

2.2 NOνA Detectors

2.2.1 **Detector Design**

The Near Detector (ND) is located 1 km from the NuMI beam at Fermilab and the Far Detector (FD) is at a distance of 810 km downstream of NuMI in Ash River, MN, as shown in Figure 2.6. The distance is set for the ν_μ first oscillation minimum. The ND sits approximately 105 m underground in a cavern with negligible cosmic exposure during beam spills. The roof of the far detector hall is covered with concrete and barite, which is effectively equivalent to having 3 m of rock above it. The NOvA detectors are functionally identical in order to minimize systematic uncertainties in the near to far extrapolation. Both the detectors are 65% active tracking calorimeters. The detectors are designed to measure neutrino interactions in the few GeV energy regime and to identify individual particles produced in neutrino interactions. The NOvA detectors are constructed from low Z materials (primarily carbon). They have a radiation length of approximately 40 cm which is equivalent to the length of 7 NOνA cells (characteristic scale in the longitudinal dimension of fully contained electromagnetic showers) and the Moliere radius (characteristic scale in the transverse dimension of fully contained electromagnetic showers) is equivalent to the width of approximately 2 NOvA cells. This allows an electromagnetic shower to develop over sufficient planes and cells to be distinguished from muons, charged pions, and protons, which appear in the detector as non-showering particle tracks. This particular feature of the detector also aids to the distinction between electromagnetic showers from two photons that originate from π^0 decays from those that originate from electrons. Separating ν_eCC events that leave an electron induced shower is of particular importance since NOνA sees significant number of photon induced showers from π^0 which are a major background of ν_e appearance. The construction common among both detectors and the details specific to the far and near detectors will be discussed in the following sub-sections. For more details, please see the Technical Design Reports of NOνA [42].

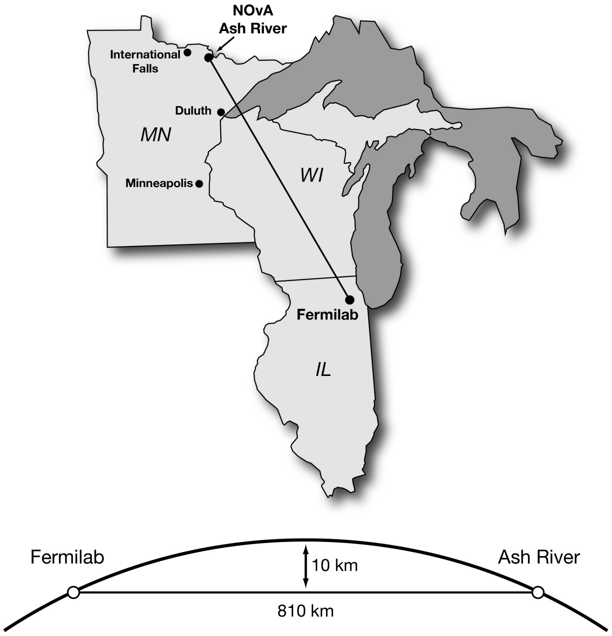

Figure 2.6 The diagram shows the geographical location of two NOνA detectors.

2.2.2 The Basic NOvA Detector Elements

The NOνA Cells and PVC Extrusions

Both detectors are based on a cellular structure. Cells are produced by extruding polyvinyl chloride (PVC) to form a rectangular rigid structure of interior cross section of 3.9 cm × 6.0 cm with 2 to 4.5 mm of thick walls outside. Each cell is filled with liquid scintillator and within the cell is a polystyrene looped wavelength shifting (WLS) fiber. Cells are made of PVC to provide the detector structural support while maintaining the low-Z design goal. The PVC is mixed with titanium dioxide, TiO_2 to attain 90% reflectivity for 430 nanometer wavelength light. The higher reflectivity allows more photons to reflect within a cell several times and increases the probability of absorption of light in the WLS fiber.

Sixteen cells are put together side by side to form An extrusion is comprised of sixteen cells side by side, shown in Figure 2.7, with each cell separated from the next by 3.3 mm of PVC. Two extrusions are glued together side by side to form a planar unit of 32 cells called a module as shown in Figure 2.8. One end of the module is capped by the end plate to contain the liquid scintillator inside and the other end is connected to a Hamamatsu avalanche photodiode (APD). PVC is approximately 30% of the total NOνA detector mass.

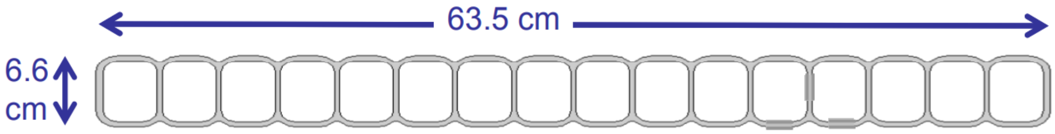

Figure 2.7 Cross section view of an extrusion (16 cells) in NOνA with a width of 63.5 cm and depth of 6.6 cm.

The picture is taken from [42].

Liquid scintillator

The detector is filled with liquid scintillator held within the cells. This liquid scintillator accounts for approximately 65% of the detector mass. The unit cell is filled with scintillator whose chemical composition is 5.23% pseudocumene (1,2,4- Trimethylbenzene) + 94.63% mineral oil +$\sim$ 1% wavelength shifting (WLS) agents. The WLS agents used are - (PPO(2,5-Diphenyloxazole)+ bis-MSB (1,4-bis-(o-methyl-styryl-)-benzene)). The scintillator emits light with a spectrum peaked between 360 - 390 nm when charged particles pass through. WLS agents absorb the light emitted by the

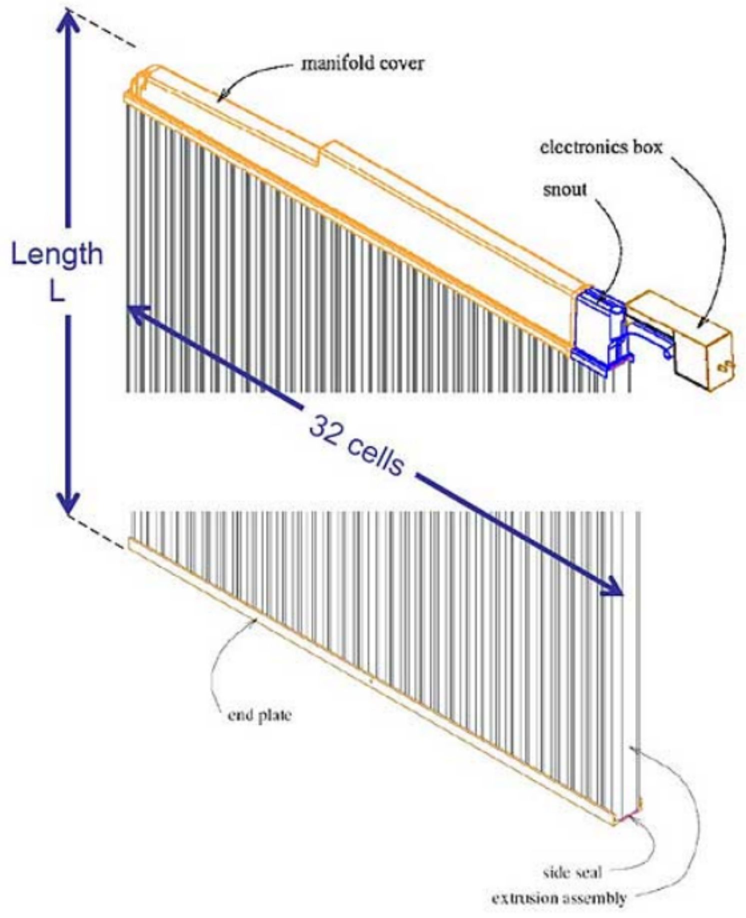

Figure 2.8 A side on view of an extrusion module constructed from two extrusions of a total of 32 cells, an end plate, a side seal, a manifold cover, a snout and an electronics box.

The picture is taken from [42].

scintillator and shift the initial wavelength of photons to 400 - 450 nm to be picked up by the optical fiber.

WLS fiber

Within the cell there is 0.7 mm WLS fiber looped at non-instrumented end of the cell as shown in Figure 2.9. Both ends of the WLS fiber are connected to one pixel of a 32 pixel APD at the instrumented side of the cell. The fiber core is made of polystyrene with refractive index 1.59 mixed with R27 dye (as the wavelength shifter). Charged particles passing through a cell produce scintillation light that reflects off the edges of the cell several times. A fraction of the scintillation light (photons) impinges on the WLS fiber. The fiber absorbs light primarily in the blue and UV spectrum (400 – 450 nm light). The absorbed wavelength of the light gets shifted to green spectrum (490 – 550 nm light). The fiber then re-emits photons in the green spectrum, shown in Figure 2.10. Some of these green photons are trapped inside the fiber by internal reflection and get transported to the fiber ends where they are measured by the APD. As light travels down the fibre it is attenuated with light in the range 520 – 550 nm preferentially surviving.

Avalanche Photo Diode (APD)

The light that exits the WLS fibre ends is detected by an APD. An APD converts a light signal into an electronic signal pulse. Fig.2.11 shows a photograph of an APD containing an array of 32 pixels. Each APD pixel is interfaced with both ends of a looped WLS fibre from a single cell. Thus each pixel reads out a single cell. The NOvA APD has an 85% quantum efficiency. The high quantum efficiency is necessary because it allows the observation of faint light signal from the other end of 15 m long FD cells in NOνA. Each APD is connected to a front end board that prepares the signals from the APD for the data acquisition system. The ND cells are 4.2 m long

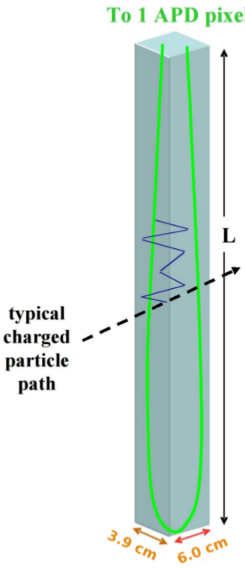

Figure 2.9 A schematic view of a NOνA cell, filled with liquid scintillator and a flourescent green wavelength-shifting fiber.

Taken from NOνA internal repository.

in the near detector and 15.2 m long in the FD. Fiber ends from a single cell are connected to one pixel of the APD, pictured in Figure 2.11.

2.2.3 Detector Assembly

The NOvA detectors are constructed from collection of cells described in section 2.2.2. A module is made of 32 cells i.e. two extrusions glued together (also discussed in section 2.2.2). Several modules are glued together to make a plane. In each plane the modules are either vertically or horizontally aligned. The cells in the adjacent planes are orthogonally rotated with respect to the previous plane as shown in Figure 2.12. This alternating orientation of the detector planes gives two independent detector views. With cells aligned horizontally, the detector measures the vertical view and

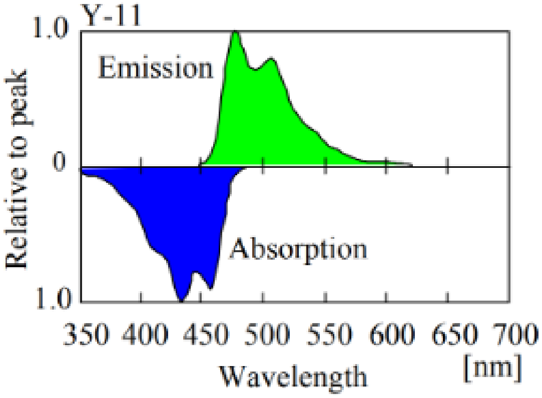

Figure 2.10 Fiber absorption and emission shape is shown as a function of wavelength.

Taken from NOνA internal repository.

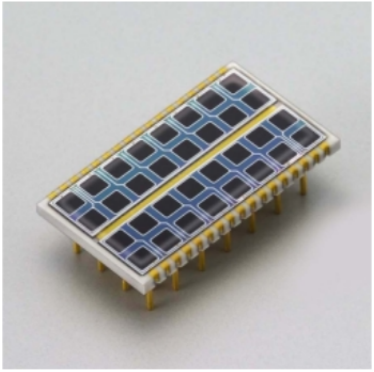

Figure 2.11 An APD containing an array of 32 pixels.

The figure is taken from [43] .

with cells aligned vertically, it measures the horizontal view. These different 2D views allow for 3D reconstruction of a particle position inside the detector. Fig.2.13 shows the 3-D as well as 2-D views of a neutrino event in the NOνA detector, made of alternate planes. Though all the fibers from each cell in the module are separated from each other, they are connected to a single optical connector at the fiber ends. This optical connector attaches the module to an avalanche photo diode (APD), shown in Fig.2.11.

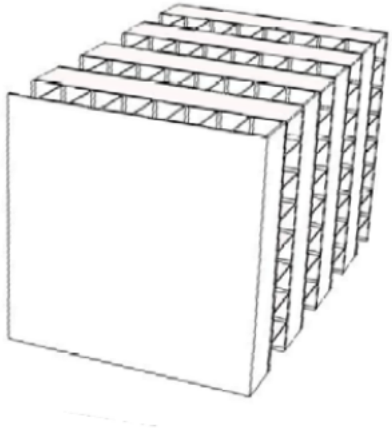

Figure 2.12 The alternating orientation of the cells within the stacked planes of NOνA detector.

The figure is taken from [42].

2.2.4 NOνA Far Detector and Near Detector

The 14 kton FD is built on the surface above sea level. Each plane in the FD consists of 12 modules and a block contains 32 planes. There are a total of 28 blocks and 896 planes and 344,064 cells in the FD. Approximately 65% of the detector mass comes from liquid scintillator and 35% comes from PVC. The FD, due to its location, sees a significant number of cosmic rays. The background due to cosmic rays is mitigated

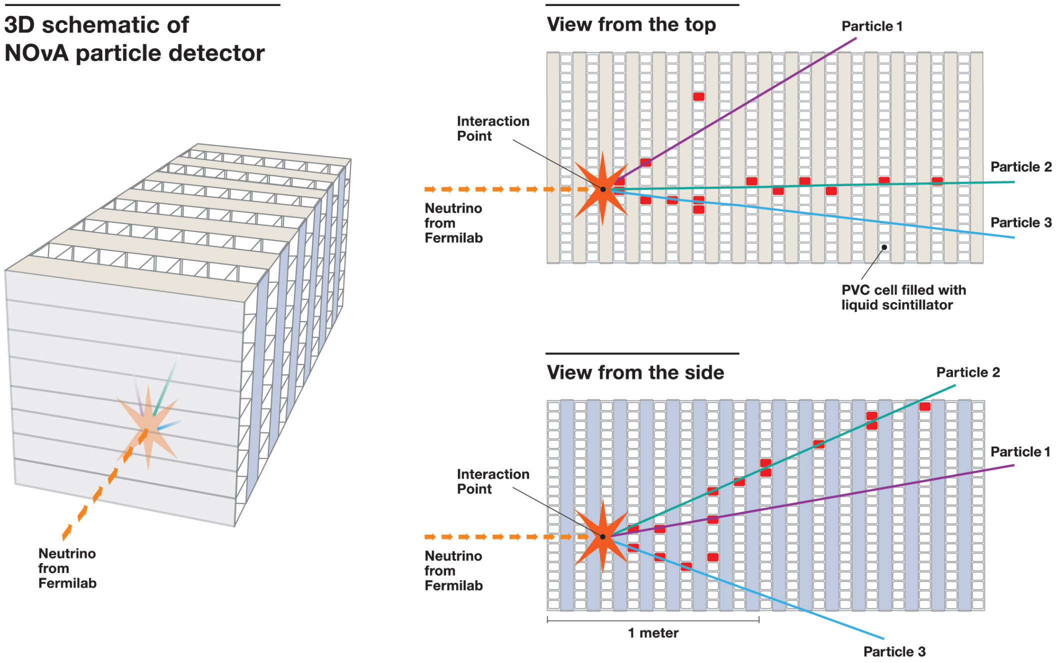

Figure 2.13 NOνA detectors are made up of planes, made of cells, put in alternate fashion. Two 2-D views of an event can be reconstructed from alternate planes as shown on the right hand side of the diagram.

Taken from NOνA internal repository.

by a shielding overburden of barite above the detector.

The ND weighs 330 tons. In the ND, a plane is made up of 3 modules. Thirty two planes constitute a block. Near detector is made up of total 8 blocks, 214 planes and 20,192 cells. The near detector has a slightly more complicated structure. We divide the entire ND into 2 region, fully active region and a muon catcher. There are 6 blocks of 32 planes in the fully-active region. The muon catcher is 3 modules wide and 2 modules tall and shorter than the fully-active region of the ND. It consists of 10 4-inch steel planes interleaved with 22 active planes. More details about the muon catcher can be found in the technical drawings [44]. The near detector is 105 m underground and 1.015 km from the NuMI target. ND therefore sees a higher flux of

Table 2.1 Hardware specifics about NOνA detectors.

	Far Detector	Near Detector
Cells per Module	32	32
Modules per plane	12	3(3,2)
Cells per Plane	384	96(96,64)
Planes per Block	32	32(n/a)
Number of blocks	28	6(2)
Number of Cells	3,44,064	18,432 (1,760)
Number of Planes	896	192 (22 + 10 steel)
Cell Depth [cm]	5.64	5.64
Cell Width [cm]	3.6	3.6
Cell Length [cm]	1550	399 (399, 274)
Detector X Dimension Extents [cm]	-780 to 780	-200 to 200
Detector Y Dimension Extents [cm]	-780 to 780	-200 to 200 (-200 to 70)
Detector Z Dimension Extents [cm]	0 to 5,962	0 to 1,280 (1,280 to 1,560)
Detector Mass [ton]	14,363	293
Liquid Scintillator [gal]	2,674,000	41,140

Detector parameters are obtained from [45], [46].

NuMI neutrino events and a lower flux of cosmic rays compared to the FD. Table 2.1 summarizes the parameter values for the near and far detectors. Figure 2.14 shows the structure of the detectors.

2.3 OVERVIEW OF DATA ACQUISITION (DAQ) SYSTEM

The main task of NOνA DAQ system [47] is to accumulate data collected from the detector and store the relevant data into hard disks permanently for offline analysis. There are charged and neutral, both particles produced when a neutrino interacts inside the detector. These particles travel through the detector and have further interactions. These interactions often create photons. How these photons reach APDs, the primary light measuring electronics, is already described in Sec.2.2.2. An APD continuously reads photon signals from 32 individual cells in the detector by looking at changes in voltages. The APDs are kept at a voltage of $\sim$ 425 V and

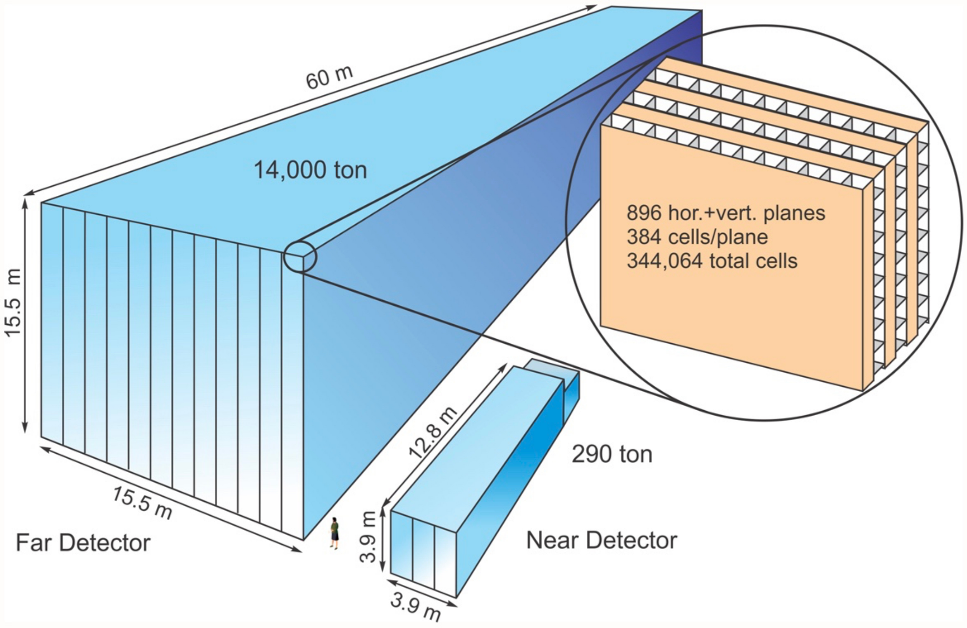

Figure 2.14 NOνA detectors - Far detector and near detector.

Picture taken from [42].

run at a gain of 100. To suppress the noise mostly due to the generation of thermal electron-hole pair, the APDs are kept at very low temperature. This is achieved by mounting a device called thermoelectric cooler (TEC) to the APD. A thermocouple measures the APD temperature and a feedback loop maintains the APD at $-15°$ C to get a stable gain. Each NOνA APD is connected to a Front End Board (FEB). FEB houses avalanche photo diode (APD), application-specific integrated circuit (ASIC), analog to digital converter (ADC) and field programmable gate array (FPGA). The signal from the APD is sent to the ASIC where it is shaped and amplified by a factor of one hundred. ASIC shapes the APD output so that a physics hit can be read out on a timescale comparable to the clock tick. The ASIC output is then propagated

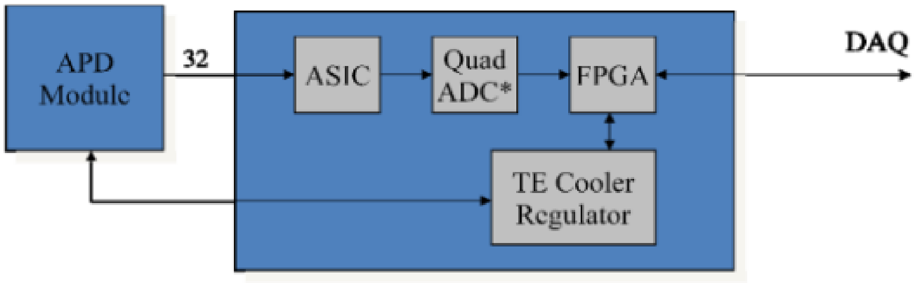

Figure 2.15 A schematic of the NOνA front end electronics.

An APD, furthest left, is the basic detection element. The APD drives an ASIC which shapes signal photon pulses into a waveform that can be read on time-scales similar to the clock tick. The shaped pulse then travels through an ADC which digitizes the signal. That then passes through an FPGA, which compares the ADC to a threshold, deciding whether to pass the signal along to the DAQ. There is also a thermo-electric cooler which interacts with the APD, keeping it at a constant temperature for a stable gain.

to an analog-to-digital converter (ADC) to digitize the signal. The digitized signal is passed to field programmable gate array (FPGA). A threshold is applied in FPGA. Hits that pass threshold are time stamped for each hit in the channel. A diagram of the FEB is shown in Figure 2.15.

The FEB transmits the digitized signals to a Data Concentrator Module (DCM). Each DCM receives inputs from 64 FEBs. There are 168 DCMs in the FD and 14 in the ND. Each DCM collects all the information from the connected FEBs during a 50μs time window called microslice [48]. A DCM accumulates 100 microslices, amount to 5 ms of data, called a millislice. The millislices from each DCM are sent to a computer in a buffer farm. After these data are transferred to the buffer farm the microslices from all the DCMs are sorted and combined by time into 500 μs events. These events are stored on the buffer farm for 30 minutes. The data is hold in the buffer so that it can be searched for various trigger conditions. Events that pass

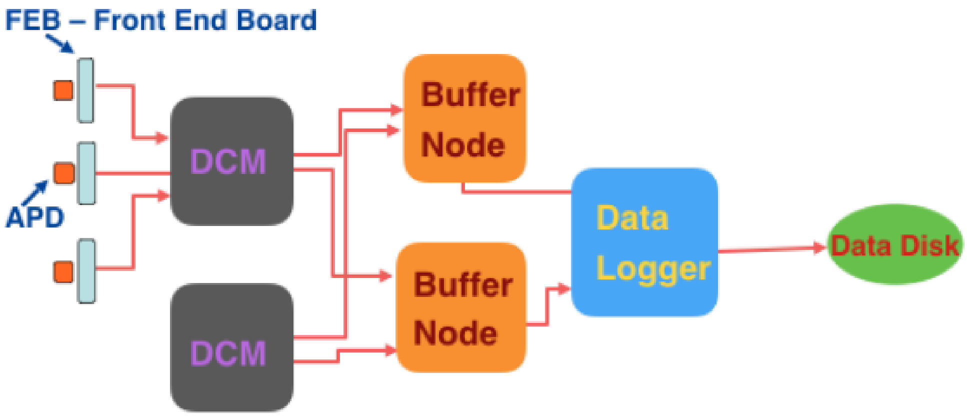

Figure 2.16 A cartoon of DAQ data flow.

different trigger conditions are copied from the buffer node to a permanent storage disk. Figure 2.16 gives an overview of how a signal received by an APD reach data disk through different components of DAQ.

2.4 Near Detector Timing Peak

The ND is 100 m underground, so the cosmic interaction rate in the ND is negligible. But the ND sees a high rate of neutrinos, for example, 3-4 neutrino interactions per NuMI spill. Therefore, the activity registered in the detector is mostly due to the interaction of neutrinos. We learned from the previous sections that the NuMI trigger window is 500 μs and the neutrino interactions occur within the 10 μs of NuMI spill covering almost the center of the trigger window. The timing of the NuMI beam in the ND can be observed after collecting a few spills of NuMI data. The beam spill in the 500 μs trigger window is found to span $218 - 228$ μs (Figure 2.17), consistent with the expectation. Because of the large statistics of NuMI interactions in the ND, we are also able to observe 6 batches of proton (Figure 2.17) in NuMI spills.

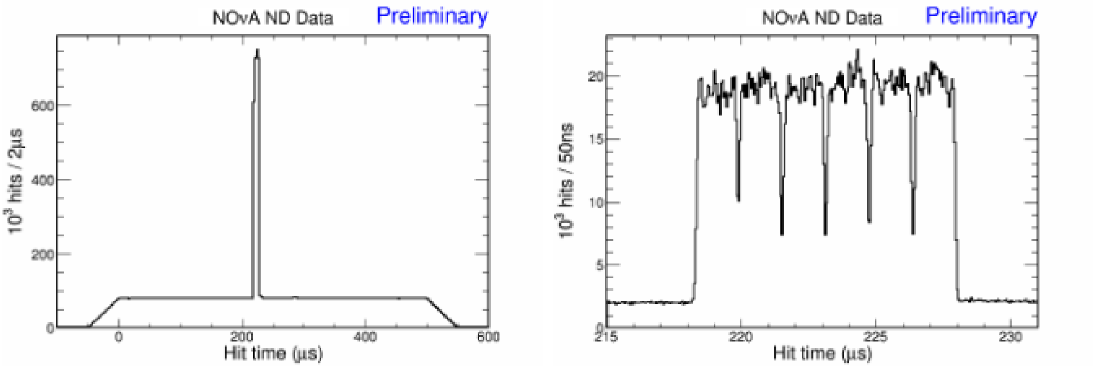

Figure 2.17 Near Detector timing peak, the left plot is over the full $500\mu s$ beam window and the right one is zoomed to show the NuMI beam structure.

2.5 CHAPTER SUMMARY

This chapter presents an overview of the NOνA beam line and the detectors. The chapter also includes a summary of the NOνA DAQ system that is responsible for various monitoring tools to ensure good quality of data for physics analysis. More on DAQ data format can be found in [48]. NOνA experiment is long baseline neutrino oscillations experiments. It has been designed and optimized to detect ν_e-CC interactions. The cells size and low z material gives NOνA a capability to differentiate π^0 and electron initiated showers and thereby a good selection efficiency over backgrounds. Use of near detector helps in canceling most of the systematic uncertainties.

Chapter 3

Reconstruction

The reconstruction of 2 track candidate events starts with a collection of above threshold APD signals collected by DAQ. Processed and calibrated signals produce a set of hits in the detector, termed CellHits. To extract useful physics information from the hits, we need to associate hits with particle trajectories and then identify the particle. These cellhits contain spatial, time, charge information about the hits. Because of the NOνA cell structure, a cellhit can only read 2-D information about the particle trajectory. The plane number gives the z coordinate of a cellhit and also provides us with either x coordinate or y coordinate depending on if the cell is vertical or horizontal. Thus a cellhit defines only 2-D view of a particle trajectory. To learn the exact location we need to build 3-D view of the particle trajectory inside the detector i.e. the x-z view of a cell must be correlated with the corresponding y-z cell view. The task of the reconstruction is to associate hits with the same physics interaction it came from and organize them into track or cluster objects. The kinematics information attached to those objects helps us identify various particles like μ, π^+, π^- etc. that in turn lead to identify various interactions such as $\nu_e CC$, $\nu_\mu CC$.

Reconstructing a physics event in data is a multi-step process. Each step has an associated module, a C++ class which performs a specific task on the input file. Every module [details are in later sections] is run in sequence. The required modules to perform the analysis presented in this thesis are

1. DAQ2RawDigit (data only) - converts raw data to a convenient format for further processing.

2. CalHit - writes hit information in a form more convenient for analysis.
3. Slicer4D - groups hits in time and space.
4. CosmicTrack - takes slice hits and makes tracks for cosmic-ray interactions.
5. KalmanTrack and KalmanTrackMerge - takes slice hits and makes tracks for ν interactions.

Each of these modules is explained in the following sections.

3.1 DAQ2RawDigit

This module is run over data that directly comes from the NOνA detectors. The initial information that comes out of the detector is saved in a format that is convenient and compact for the data acquisition system (DAQ). DAQ2RawDigit is run over an input .raw file that comes out of DAQ and convert it to a .root format for efficient reconstruction and to make the initial data compatible to the rest of the data analysis software. The output file primarily contains a collection of hits, called raw digits, for each interaction. At this stage raw digits are hits with their location in electronic coordinates. Those raw digits include information about the hit, position, pulse height and time.

3.2 CalHit

The module takes in raw digits straight from the output of DAQ2RawDigit module and creates cell hits. CalHit associates each hit with a detector cell and a detector plane. If a hit comes from channels deemed bad by the BadChannel service, software that monitors detector performance, CalHit will remove the hit. Too many or too few determine if a channel is considered good or bad for a period of detector running. CalHit uses attenuation and absolute calibration information to convert pulse height measurements to the energy deposited in the cell i.e. GeV, as described in Chapter 4. CalHit also determines the precise time of the hit in nanoseconds.

3.3 SLICER4D

In the NOνA detector, data are recorded in trigger windows of length 500 μs. The collection of hits that occurs within the specified time interval is called an event. An event may contain multiple physics interactions. The neutrino beam spill is for only 10 μs and is roughly at the center of the data readout window (500 μs). There are approximately 3-4 neutrino interactions that ND sees from each beam spill and interactions are often confined to specific regions of the ND. Thus, the challenge is to separate each neutrino interaction that occurs within each beam spill in ND from each other. In the FD, neutrino interactions are rare but a readout window typically sees $50 - 70$ cosmic rays. The reconstruction tool used to cluster contiguous hits in time and space from the collections of hits is Slicer4D. The produced cluster of hits are called slices. Slicing in NOνA is based on the DBSCAN (Density-Based Spatial Clustering of Application with Noise) algorithm [49], which groups together hits with high density that are potentially related to each other. The algorithm applies a scoring system to cluster hits based on the distance in time and space from other hits in the trigger window. Any hit that does not get clustered is defined as a noise hit.

Finally, if the Slicer works perfectly, each slice would correspond to one physics interaction (mostly neutrino interaction in ND and cosmic ray in FD) and would remove hits originating from electronic noise and from other interactions. For more information, see the technical note [50]. These slices are then, fed to different reconstruction chain to reconstruct event candidates. Figures in 3.1 show examples of slicing in the near and far detector. Note that the dots in the same color indicate hits clustered in the same slice by slicer and different colors represent different slices occurred at different time in 500 μs readout window.

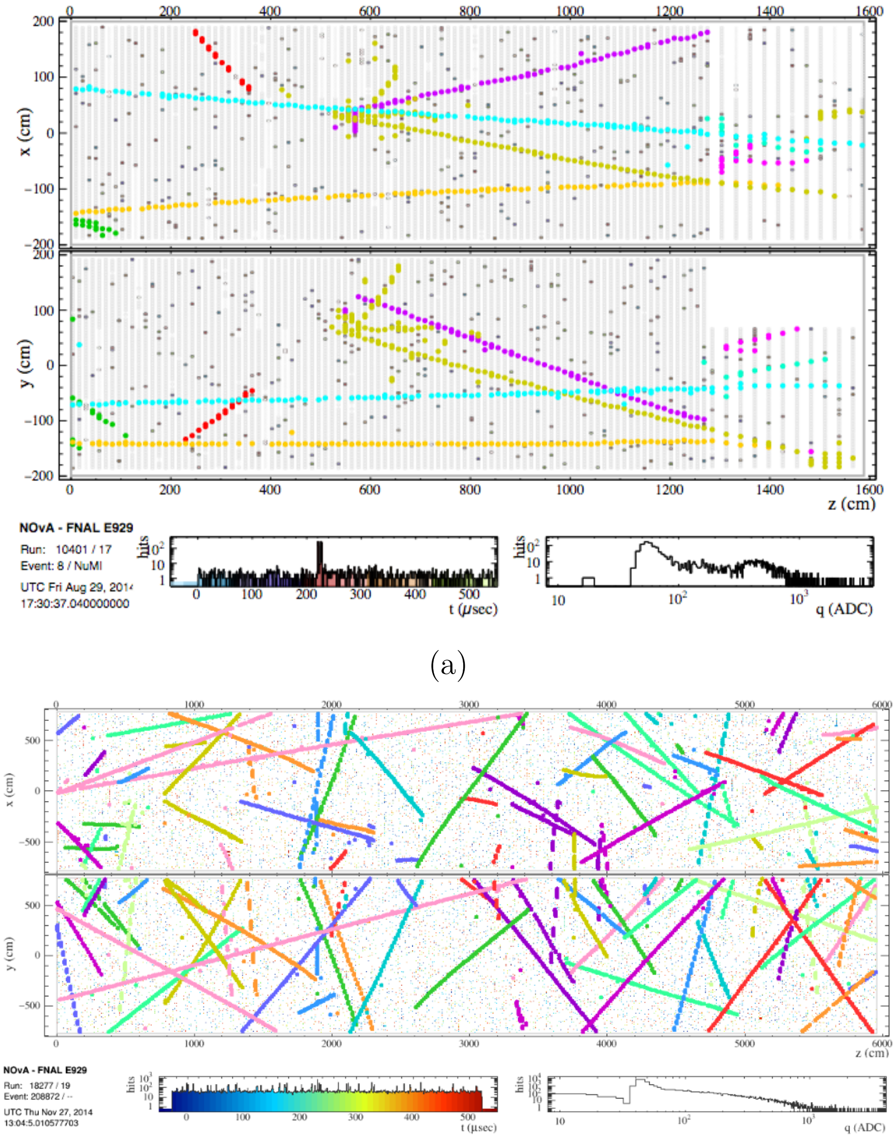

(a)

(b)

Figure 3.1 The event display of ND and FD after slicing.

(a) The display is zoomed in on the 10 μs time window for a near detector spill to display neutrino activity. Slices are indicated by hits with the same color from the same slice.
(b) Far detector 500 μs time window shows cosmic rays. The dots in the same color indicate hits that have been clustered together in the same slice by slicer.

3.4 TRACKING

A track is defined as a mostly contiguous string of cell hits that would result from the energy deposited by a single, non-showering particle. Tracks are reconstructed from individual slices. The goal of the tracking is to take the detector hits that belong to the same slice and reconstruct the trajectory of individual particles in the detector. This is useful in identifying particles that deposit energy with a track like signature, such as muons, pions. There are two kinds of tracking algorithms used, described in following two subsections:

3.4.1 Cosmic Tracking

The tracking is performed on slices (as described in the previous section). As the name suggests, cosmic track algorithm is optimized for finding high energy vertical tracks fitted from the hits produced by cosmic particles (mostly muons) coming from atmosphere in the detector. The algorithm makes use of a basic straight line-type fitter by fitting a line along the trajectories in either view (X-Z or Y-Z) of the detector. The fitter minimizes the distance between the hits and the fit line and removes hits that are greater than some distance from the line about 10 cm ($\sim$ 2 cells). By removing those hits, most of the noise hits are removed. Figure 3.2 shows a cartoon of such tracking approach. The tracks formed are 2-D tracks and are found in each view of the detector. The two tracks found in both the views are combined to form 3-D tracks. More details on cosmic tracker can be found in [51].

3.4.2 KalmanTrack and KalmanTrackMerge

The trajectories of charged particles within a neutrino interaction are reconstructed using a technique based on the Kalman filter algorithm [52, 53]. The Kalman tracking algorithm produces reconstructed tracks called Kalman tracks. KalmanTrack is a module that takes in clusters of hits from Slicer and groups the cell hits corresponding

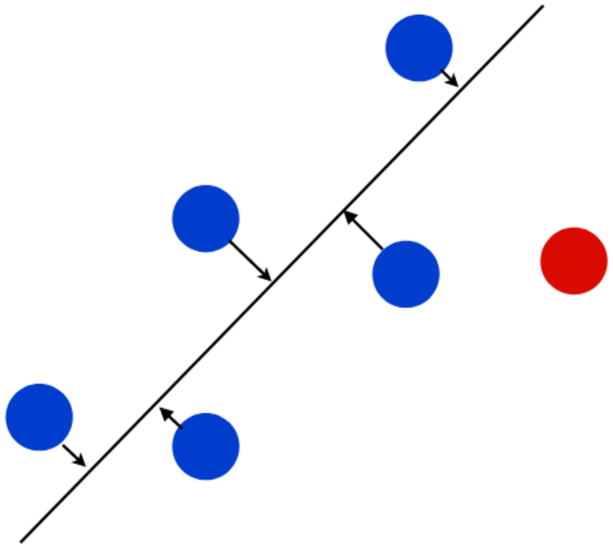

Figure 3.2 A diagram of Cosmic tracking approach.

The colored circles represent cosmic hits. The solid black line is the straight line-type fitter that optimizes the distance between a given hit and the fit line. The red hit is rejected for being far from the fitter.

to a single view (either vertical or horizontal). Within each view seeds are created with a pair of hits that are less than 3 planes apart. These seeds form a test track. To predict the next adjacent hit the test track is then propagated to the next plane using the current value of the track position and slope. Any hits found in the next plane consistent with being on the test track or close to the predicted location are added to the track. After a hit is added to the track the slope and intercept of the track get updated with the new measurement. The process continues to the next plane and is repeated until no more hits are left to add to the track. See Figure 3.3 for a diagram of this tracking approach.

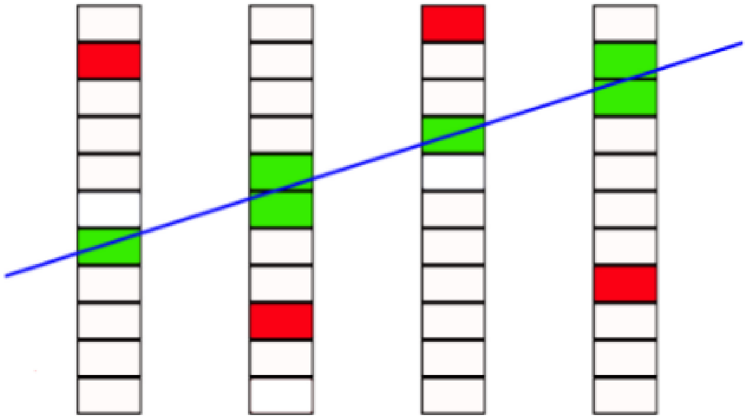

Figure 3.3 Diagram of tracking approach of 2D Kalman tracks.

The colored rectangles represent a hit in a given plane. The green hits are included on the track based on an estimate of position and slope of the solid blue line. The red hit is inconsistent and not part of the track. This process will repeat for the next plane until there's no hit left to be added on the track.

These 2D tracks continue to propagate until they cross 3 consecutive planes in a view without adding a hit. This track finding process initially starts from the downstream end of the detector, where particles emerging from a neutrino interaction are relatively more separated than they are in the upstream and proceeds upstream. After a complete track is found, the procedure is repeated, but now in the reverse direction i.e. starting from the other end of the found track. This is to determine if any of the previously added hits should now be rejected. The procedure continues to create more 2D test tracks in each view independently. With at least 4 track hits a test track is promoted to being a valid track.

After all the 2D tracks have been made in each view independently, KalmanTrack-Merge looks at two consistent 2D tracks from different views and tries to merge them into one 3D track. The information from the 3D tracks and unmatched 2D tracks are written out to the file. This information includes the start position of the most upstream (lowest z) part of the track, the end position of the most downstream (highest z) part of the track and all the hits associated with each track. Additional information about the tracking algorithms can be found in internal NOνA document [54] or the thesis by Raddatz [55].

3.5 Chapter Summary

The signal for our current analysis is charged particles initiate a track like signature in the NOνA detector. To identify tracks, NOνA has developed the event reconstruction tools and particle-ID algorithms. The reconstruction of particle in NOνA starts from calibrating the hits using the cosmic muons (Calibration is elaborately described in Chapter 4). After this, events for the current analysis is reconstructed through the slicer and Kalman tracking algorithms to get the global and kinematics based features of the event. Then an event is processed through particle identification algorithms so that an event can be classified under a particular particle hypothesis.

Chapter 4

Calibration

4.1 Calibration

To extract physics out of the detector hits, we need to convert a hit into an energy deposition in those cells based on the amount of light measured. An APD converts the light to an electronic signal and an ADC converts the electronic signal to a digital number. The digital number is sent to FPGA (discussed in section 2.3) where it is converted into a count of photo electrons (PE). The DAQ prescribes a methodology to record the PEs above some threshold. But before using those signals to extract physics, they must first be calibrated so that neutrino energies can be reliably reconstructed. This procedure is accomplished in two sequential steps:

1. Attenuation Calibration that corrects for light attenuation in a cell.
2. Absolute Calibration that converts the corrected ADC value to a standard energy unit (MeV).

The steps above are elaborated in next sections.

4.2 Attenuation Calibration

The attenuation calibration is performed for each cell in both NOvA detectors. NOvA cells are quite long, 15.7 m in the far detector and 3.9 m in the near detector. So photons collected by the fiber from particles that pass through the far end of a cell (from APD) are attenuated as they travel to register the response to APD. Therefore, there are variations in response along the length of the fiber in the same cell and variations in response among different cells as well. Attenuation calibration is applied to correct for these variations so that all hits across different regions of the detector can be compared on equal footing. To correct for this effect, attenuation calibration translates ADC values into a new unit called corrected Photo Electron (PECorr).

The attenuation calibration uses cell hits from cosmic ray muons that pass through the entire detector. The track reconstruction used for cosmic muons for calibration purpose is called CosmicTrack algorithm, described in section 3.4.1. The detector response to these cell hits divided by path length through the cell i.e. PE/cm, provides an uncalibrated response per cm. To provide an accurate path length, calibration uses tricell hits, shown in Figure 4.1. A tricell hit refers to the interior hit of the 3 contiguous hits that belong to 3 consecutive cells in the same plane. This criteria allows the path length through the cell to be precisely measured from the cell width and the angle of the track. The calibration starts with a set of tricell hits selected from cosmic tracks. Then the tricell response is plotted as a function of the distance from the center of the cell along the fiber, referred as W. For each cell, a two dimensional histogram of PE/cm vs W is made and the mean PE/cm value is stored as a profile histogram. An example of such 2D histogram is shown in Figure 4.2. The profile of this plot is taken and fit is then performed. For the central portion, the shape of the attenuation correction is of two exponentials. To fit the “roll off" section at the near and far ends of a cell, LOcally WEighted Scatter plot Smoothing (LOWESS) algorithm [56] is applied. An example of the attenuation fitting procedure is shown in Figure 4.3. The fit curve provides information of PECorr across the W range of a cell. This procedure is repeated for every cell in the detector. PECorr values are used to correct the detector response [57, 58]. Figure 4.4 shows the corrected detector response.

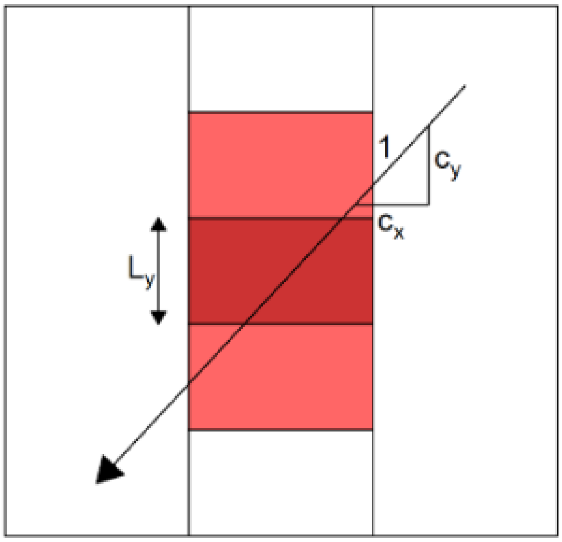

Figure 4.1 Diagram of a tricell hit.

Diagram of a tricell criteria in the detector where three consecutive cells in a plane have been hit. The track length through the inner cell is reconstructed by $L_y/\cos\theta_y$ using the diagram's nomenclature. This outer cells in the triplet do not hold this relation, so only the middle, dark red cells are used in calibration.

4.3 Absolute Calibration

Attenuation calibration converts ADC value to corrected photo electrons (PECorr). Absolute calibration offers a prescription to translate the PECorr into energy deposit in standard units, MeV. This method also relies on tricell hits from cosmic muons, but uses muons that stop inside the detector with the presence of a Michel electron at the end of the track. Stopping muons are used since we can accurately estimate the muon energy loss in the detector using the Bethe-Bloch formula. After selecting muon tracks, the $PECorr/cm$ is plotted as a function of the distance to the endpoint of the track, shown in Figure 4.4. It is observed that the MIP region of the track exists

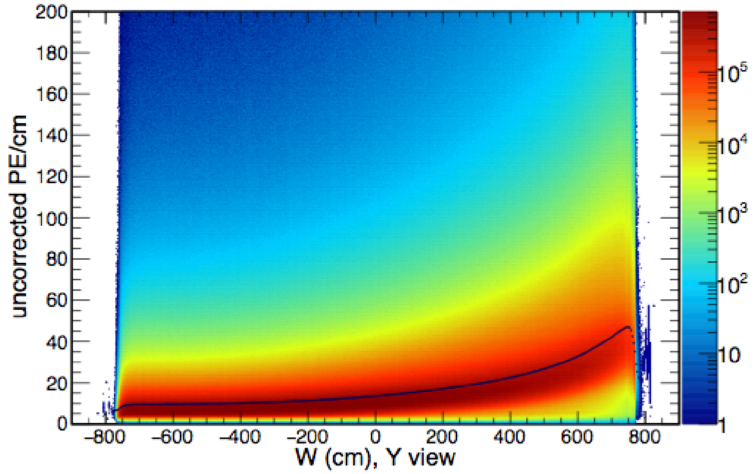

Figure 4.2 The figure shows the 2D distribution of PE/cm vs W for through going cosmic muons.

The mean PE/cm value for each value of W in the Y view cells is shown by the black data points. Figure taken from [57].

in the 100–200 cm range from the end of the track, where dE/dx is approximately constant. Hits more than 200 cm or less than 100 cm from the end point begin to influence dE/dx due to the relativistic rise or Bragg peak of the Bethe-Bloch equation. Thus, hits in the 100-200 cm range from the track endpoint are used as the standard candle for absolute calibration. An average response (mean $PECorr/cm$) in this range is calculated. Scaling the mean $PECorr/cm$ of this sample to the Monte Carlo (MC) prediction of the mean of the distribution of true energy deposits in this track window provides a conversion factor between the mean $PECorr/cm$ and the true energy deposited in the scintillator for muons. In other words, absolute energy calibration is a factor that takes in the units called $PEcorr/cm$ and converts it to a physical energy scale measured in MeV/cm. The conversion factor used in this analysis is approximately 1.4 MeV / cm. Figure 4.5 shows the calibrated dE/dx distribution of stopping muons in NOvA's far detector. The absolute calibration

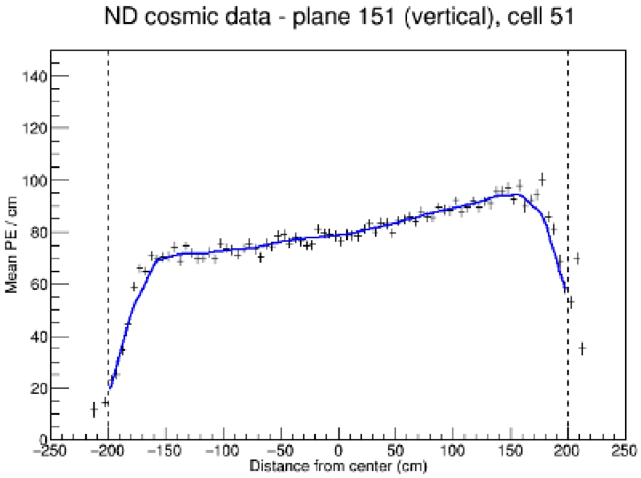

Figure 4.3 The diagram plots the mean PE/cm vs W profile.

The mean PE/cm varies with the distance measured relative to the centre of the cell. The blue curve shows the attenuation calibration fit for a cell in the near detector (plane 151 and cell 51) in the ND. The data is shown in black. Figure taken from [57].

method and the advancement over different analysis are discussed in technical notes and papers [59, 60, 61].

4.4 Timing Calibration

The NOvA experiment consists of two detectors separated by 810 km. The electronic components of these two detectors must be precisely synchronized in time to be able to identify interactions within a detector . Both the detectors must be externally synchronized with the neutrino beam clock to correlate candidate events from the neutrino beam. Any component of the detector or beam uses GPS for time stamp. The timing offset between beam spill and neutrino interactions in ND, FD are determined from data. The aim of the timing calibration is to achieve internal and

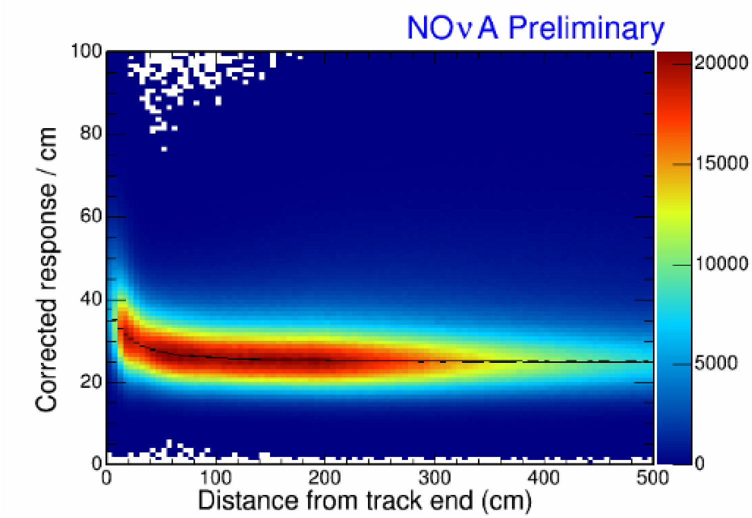

Figure 4.4 Displayed is the corrected detector response ($PECorr/cm$) as a function of distance from the track end.

This plot is used for absolute energy calibration in the far detector. for cosmic ray muons that stopped inside the detector. The black fit points show the mean of the fit to the distribution for each vertical bin. Values between 100 and 200 cm from the end of the track are considered the MIP region and used for the absolute energy calibration in far detector data.

external synchronization. The internal timing calibration measures and accounts for timing offsets between electronics regions of the detector. detailed info can be found here [62].

4.5 Chapter Summary

This chapter presents an overview of calibrating the NOνA detectors using cosmic data.

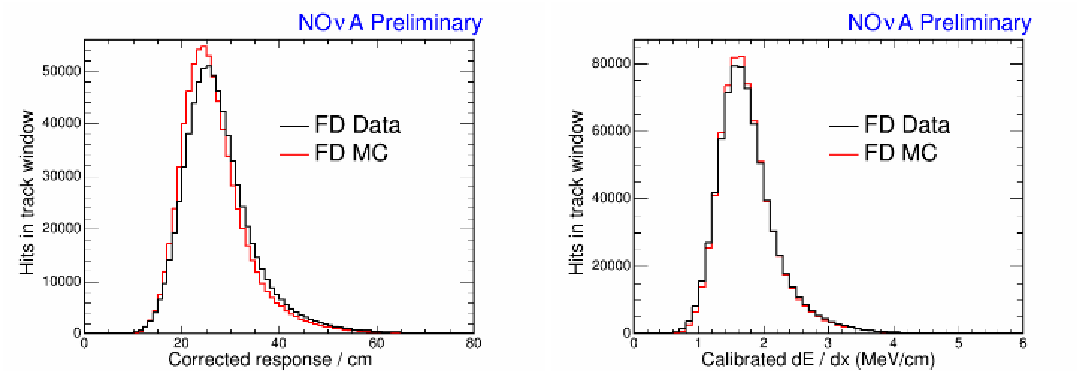

Figure 4.5 The plots show the distribution of $PECorr/cm$ between data and MC before and after applying absolute calibration.

Note the data and MC figures on the left don't perfectly align. This is before applying absolute calibration. On the right is calibrated MeV/cm, after absolute calibration applied. The data and MC show relatively better agreement after applying absolute calibration.

CHAPTER 5

EVENT SELECTION

We describe here the initial selection of "$\nu N \rightarrow 2track$" events recorded in the NOνA near detector. This selection is based on the final state event topology we are going to study in this analysis. We classify the event selection in two categories. The first category, data quality, requires the detector to record quality NuMI spill data and ensures that the data used is of sufficiently good quality for this analysis. The second category, containment and fiducial, relies on different reconstruction/analysis cuts to reject events that have particles escaping the detector and improves the accuracy of the reconstructed muon neutrino energy. The motivation for skimming only 2-tracks in the final state is to get relatively small data sample that contains only what we want to analyze. The skimmed dataset is used for particle identification among the particle trajectories within an event.

5.1 ANALYSIS PERIOD

The Near Detector began collecting data on August 18th, 2014 and only operated as a complete detector due to its smaller size. The data used in this dissertation span a time period from the starting period of data taking until Jan. 2017. The data is registered as official Production3 Near Detector dataset. There's a total of 12,478 files and 28,465,324 events in the entire dataset.

After a long accelerator shutdown between May of 2012 and September of 2013, the beam was commissioned and operated typically between 200 to 280 kW between March and September of 2014. After another accelerator shutdown the beam began operating at 300 kW in November 2014 and ramping to 400 kW by April 2015 with a peak of 520 kW. The full 700 kW beam power started in 2016. The beam was configured to run neutrinos during the data taking period.

The quality of our physics is impacted by the quality of our beam, the quality of our detector and the reconstruction of our physics events inside the detector. Section 5.1 will address the beam and data quality cuts and section 5.2 will focus on reconstruction and analysis pre-selection cuts.

5.2 DATA QUALITY CUTS

Data quality cuts ensure that the beam and the detector were in a reliable state at the time of data taking. High quality data starts with requiring high quality beam. This requires the beam to be of high intensity, hits the target and the trigger be in time with beam spill provided by the accelerator. The information on beam related metrics is hosted centrally in the intensity frontier database (IFDB) from where it can be retrieved by all the experiments on the NuMI beam. The selection cuts that are applied on beam spills are listed in Table 5.1.

The Near Detector sees 3–4 neutrino interactions per NuMI beam spill. The data taken with the detector is primarily organized by run. A run is a contiguous period of data taking with a single detector configuration. During a run, manually-set detector configurations do not change. A run is split into subruns with a typical Near Detector subrun lasting an hour. A run ends when it has 64 subruns or when the total run duration is 24 hours, or when the detector stops taking data. A subrun ends when it has a duration of 1 hour or the file size is 1 GB, or the detector stops taking data. For the near detector, subruns are often 1 hour. The subrun quality metrics are designed to remove data in case of significant or repeated failures of hardware during the span of a subrun. The near detector good subrun selection is based on simple independent cuts listed below. I developed the "good subrun selection algorithm" for

Table 5.1 Beam Quality Spill Cuts

Cut	Description	Motivation
$\|\Delta SpillTime\| < 0.5 sec$	Time of trigger recorded by the detector to be within 0.5 sec of a trigger time in IFDB	To ensure the trigger time recorded by the detector match the Intensity Frontier beam DataBase (IFDB).
POT of spill $> 2 \times 10^{12}$	Protons on target for the spill must be greater than 2×10^{12}.	To reject any of the low intensity beam that is unlikely to cause any interaction.
-202 < Horn Current < -198	The current within the focusing horns must be between -202 and -198 kAmps.	To focus π^+ in to the decay pipe.
0.02 < X Position < 2.00	The horizontal position of the beam must be between 0.02 and 2.00 mm.	To hit the target exactly where we are expecting
0.02 < Y Position < 2.00	The vertical position of the beam must be between 0.02 and 2.00 mm.	To hit the target exactly where we are expecting.
0.57 < X Width < 1.58	The horizontal width of the beam must be between 0.57 and 1.58 mm.	To ensure the beam hits the target on axis.
0.57 < Y Width < 1.58	The vertical width of the beam must be between 0.57 and 1.58 mm.	To ensure the beam hits the target on axis.

NOνA data quality group. The algorithm was applied to select the dataset to run the first oscillation analyses on. Detailed information can be found in [63].

- **Detector Size:** All four diblocks are required to be in good working condition for a subrun to be selected. A diblock is considered good if all the DCMs in it are operating optimally, i.e. when it contains 12 good Data Concentrator Modules (DCM). A good DCM must have at least 56 good Front End Boards (FEB) or fewer than 9 misbehaving FEBs. A good FEB contains at least 26 good pixels (at most 6 bad pixels).
- **Subrun duration:** subrun $>$ 1000 spills.
- **Timing Peak:** The timing peak is defined as the time when majority of the data comes from the numi beam. We check if the detector is synchronized with beam by applying the following cuts on timing peak (see section 2.4).
  - 217 μs $\leq$ timing peak start $\leq$ 219 μs,
  - 227 μs $\leq$ timing peak end $\leq$ 229 μs.
- **Empty Spills:** Fraction of empty spills (no proton in a spill) in subrun $< 3\%$.
- **Slice Rate:** 3.5 $<$ number of slices / spill [2.5 x 10^{13} PoT/spill equiv.] $<$ 5.5.
- **MIP Rate:** 12 Hz $<$ median number of signal ADC hits / 1000 spills [2.5 x 10^{13} PoT/spill equiv.] $<$ 20 Hz.

The subruns that pass data quality cuts are termed as good subrun. During the analysis period 11,456 good subruns were found out of a total of 12,478 subruns with an efficiency of 91.80%.

5.3 Reconstruction and Analysis Cuts

5.3.1 Basic Quality Cuts

Basic quality checks are imposed to ensure the detector was performing normally and that events are able to be reconstructed. To ensure the slice contains some physics interaction, we require that the slice has more than 20 hits. To remove primarily vertical events, presumed to be cosmic background, we require that the slice has hits in at least 4 contiguous planes.

5.3.2 Containment and Fiducial Cuts

The selection requires to have only 2 3D-Kalman tracks or 2 2D-Kalman tracks in one view and one 2D Kalman track in other view. With the containment cuts we want to ensure the neutrino events reside entirely inside the detector where as the fiducial requirements make sure the that the ν interaction vertex originates inside the detector. In this analysis we select events with 2 tracks sorted by length in descending order. We call the first one “long track" and the second one “short track". The majority of the 2 track events are expected to originate from charged current interactions (ν_μCC). Majority of CC interactions contain μ since the beam is configured to run in the ν_μ mode. Thus we expect the long track to be primarily from muons and the short track to be a proton or a pion. Selection of containment is based on muon, proton and charged pion expected in data.

Long Track containment :

For containment, we want to make sure the long track does not have hits in the outside layers of the near detector. Also particles may escape the detector without leaving energy in the active region while passing through the dead material. The goal of the containment is to determine the minimum distance from the edge where the probability of missing a hit for long track is very low.

Because NUMI beam mostly contains ν_μ, we expect the charged lepton, responsible for long track in the near detector, to be primarily a μ. To derive how deep do we need to go from the edge to make a long track well contained in the near detector, we analyzed the properties of cosmic muons in far detector(FD). Because FD is on the surface, there's an abundance of cosmic ray muons entering the detector from outside. Most of these muons go through the detector while some stop inside. The start position of a cosmic track was studied separately in x and y direction. Figure 5.2 displays the start x and start y position of a cosmic track. The peak at $|760|$ cm in the zoomed histograms reflect the detector edges. We also observe a second, wider peak in almost all of the zoomed histograms. The second peak is the contribution from the orthogonal view. In Figure 5.1, cells with open ends are instrumented for read out purpose, as shown in Figure 2.8. The instrumented sides of the horizontal planes are misaligned with the vertical planes. The misalignment causes the detector to register muon start points at farther than $|760|$ cm. leading to a second peak in the histograms.

A closer look at the zoomed histograms reveal the start position of cosmic track exponentially decays inside the detector. Because we observe two peaks in every zoomed start co-ordinate histogram, we have a choice to make an exponential fit to either of these peaks. Fitting the second peak would give us relatively large decay constant, that in turn, would result in relatively large distance from the edge of the detector. The larger decay constant will ensure we are deep enough inside the detector so no neutrino can escape.

The goal now is to calculate the distance a cosmic muon travels in the far detector from the edge to the center where the probability of finding the first hit is very very small. The distance is determined using an exponential fit to the start co-ordinates of cosmic tracks near detector edges. The exponential fit, drawn in red curve, holds the form $p_0 \cdot \exp^{p_1 \cdot (x-p_2)} + p_3$, where p_0, p_1, p_2, p_3 are fit parameters and x represents

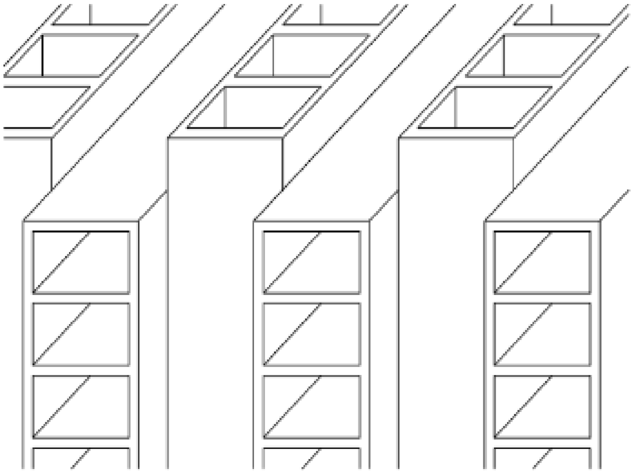

Figure 5.1 A sketch of the orthogonal structure of the NOνA detectors.

The alternating vertical and horizontal planes is shown. They are filled with liquid scintillator. The open ends are capped for instrumentation. The neutrino beam is incident from the left. The end of the vertical planes are misaligned with the end of the horizontal planes. Figure is taken from [64].

the co-ordinate. The parameters extracted from 4 fits are reported in Figure 5.3. These fit information are used to determine the containment requirement. We chose the probability to be 0.004. This is the same probability of a muon traveling some distance without leaving a hit in the detector, if the muon was produced inside. We calculate the distances in x and y direction from the edge of the far detector. Since the near detector and far detector are identical in material composition, we can apply the same constraints in the near detector.

For the containment in the z direction we use the near detector. The origin of the z coordinate is defined as the center of the front face of the first plane of the detector. The near detector has a muon catcher with steel plates (see section 2.2.4). The muon catcher has a coarser resolution than the active part of the detector. Finally the

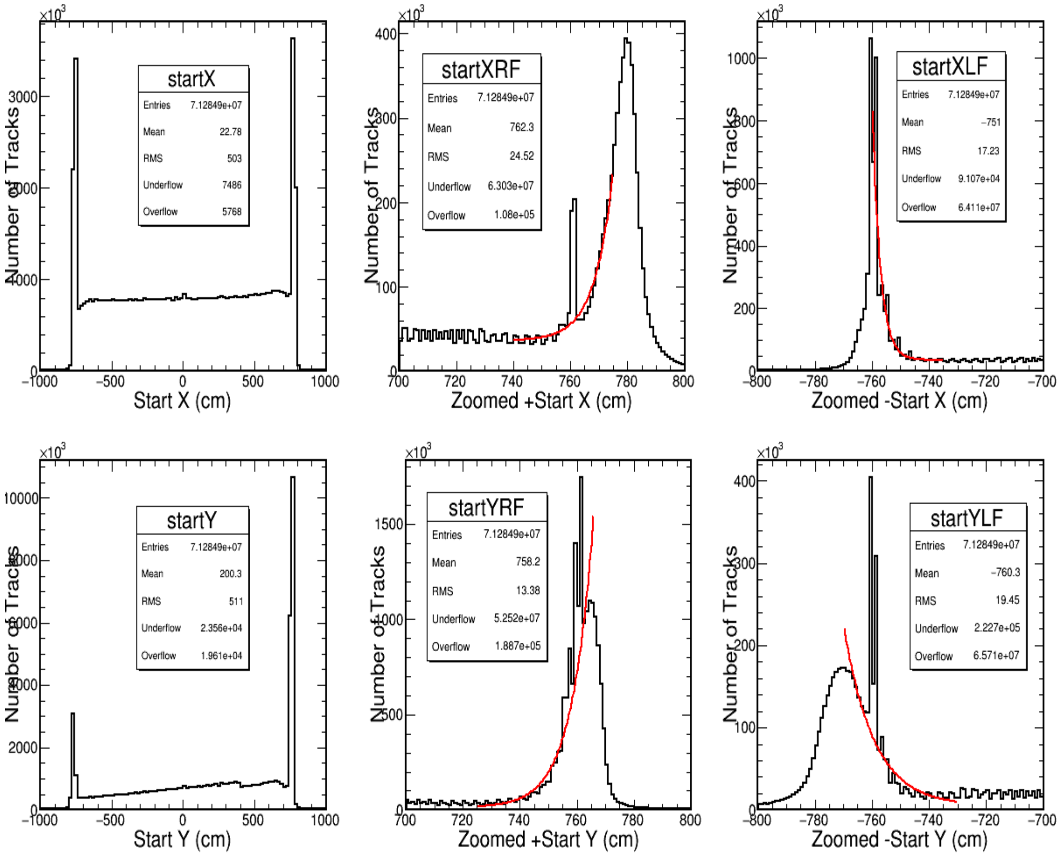

Figure 5.2 The figure displays the start co-ordinates of cosmic muons in the far detector.

The top row shows the distribution of start x co-ordinate. The left plot spans the entire x coordinate, the middle and the right plot zooms in the positive and negative edges of the x axis respectively. The bottom row shows the same characteristics of the plots but in the start y co-ordinate.

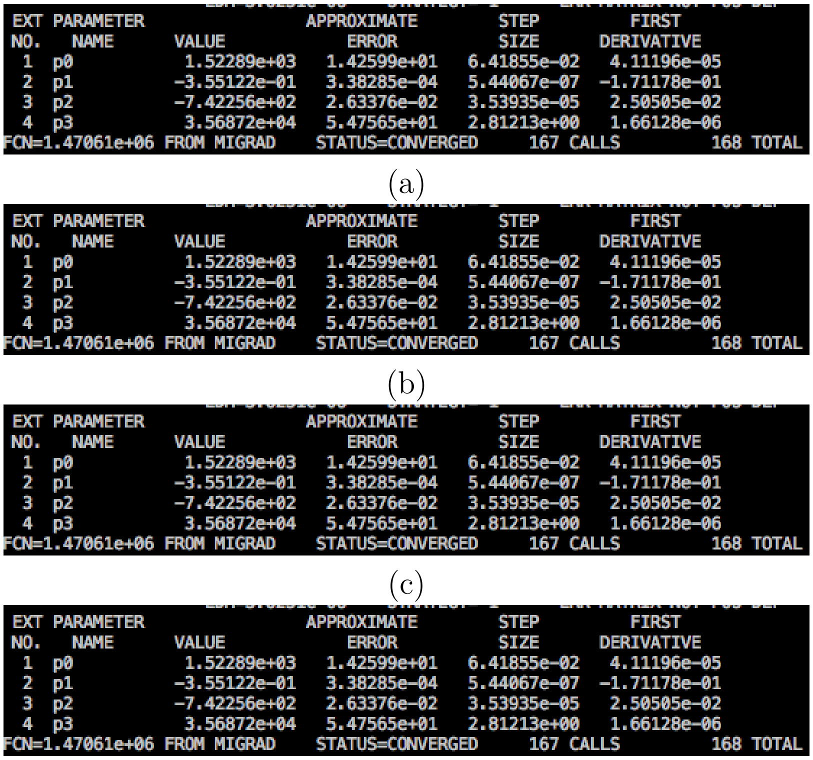

```
 EXT PARAMETER                APPROXIMATE        STEP         FIRST
 NO.   NAME      VALUE            ERROR          SIZE      DERIVATIVE
  1  p0           1.52289e+03   1.42599e+01   6.41855e-02   4.11196e-05
  2  p1          -3.55122e-01   3.38285e-04   5.44067e-07  -1.71178e-01
  3  p2          -7.42256e+02   2.63376e-02   3.53935e-05   2.50505e-02
  4  p3           3.56872e+04   5.47565e+01   2.81213e+00   1.66128e-06
FCN=1.47061e+06 FROM MIGRAD    STATUS=CONVERGED     167 CALLS         168 TOTAL
```

(a)

```
 EXT PARAMETER                APPROXIMATE        STEP         FIRST
 NO.   NAME      VALUE            ERROR          SIZE      DERIVATIVE
  1  p0           1.52289e+03   1.42599e+01   6.41855e-02   4.11196e-05
  2  p1          -3.55122e-01   3.38285e-04   5.44067e-07  -1.71178e-01
  3  p2          -7.42256e+02   2.63376e-02   3.53935e-05   2.50505e-02
  4  p3           3.56872e+04   5.47565e+01   2.81213e+00   1.66128e-06
FCN=1.47061e+06 FROM MIGRAD    STATUS=CONVERGED     167 CALLS         168 TOTAL
```

(b)

```
 EXT PARAMETER                APPROXIMATE        STEP         FIRST
 NO.   NAME      VALUE            ERROR          SIZE      DERIVATIVE
  1  p0           1.52289e+03   1.42599e+01   6.41855e-02   4.11196e-05
  2  p1          -3.55122e-01   3.38285e-04   5.44067e-07  -1.71178e-01
  3  p2          -7.42256e+02   2.63376e-02   3.53935e-05   2.50505e-02
  4  p3           3.56872e+04   5.47565e+01   2.81213e+00   1.66128e-06
FCN=1.47061e+06 FROM MIGRAD    STATUS=CONVERGED     167 CALLS         168 TOTAL
```

(c)

```
 EXT PARAMETER                APPROXIMATE        STEP         FIRST
 NO.   NAME      VALUE            ERROR          SIZE      DERIVATIVE
  1  p0           1.52289e+03   1.42599e+01   6.41855e-02   4.11196e-05
  2  p1          -3.55122e-01   3.38285e-04   5.44067e-07  -1.71178e-01
  3  p2          -7.42256e+02   2.63376e-02   3.53935e-05   2.50505e-02
  4  p3           3.56872e+04   5.47565e+01   2.81213e+00   1.66128e-06
FCN=1.47061e+06 FROM MIGRAD    STATUS=CONVERGED     167 CALLS         168 TOTAL
```

(d)

Figure 5.3 The figure displays the fit parameters for various plots in Figure 5.2.

Each of (a), (b), (c) and (d) shows 4 different fit parameters. (a), (b), (c) and (d) represent parameters for top middle, for top right, bottom middle and bottom right figures in Figure 5.2.

muon catcher is shorter in height than the active region. This has been taken into account while placing a cut in the end z position of a track. A track z end position is less than 1275 cm or has a y position less than 55 cm when crossing from the active region to the muon catcher.

Short Track Containment :

The short track, by choice of selection, is shorter than the long track. We apply the same containment criteria for the end x, y and z coordinates of the short track.

The cartoons in Figure 5.4 and Figure 5.5 display the containment region. All the containment criteria for both the tracks are listed in Table 5.2.

Fiducial Requirement :

The short track is mostly populated by protons and charged pions. Thus, we consider the hadron interaction length to calculate fiducial selection cuts for short track. Hadronic particles can undergo scattering processes through nuclear interactions. Our detector is composed of scintillator and PVC. The hadronic interaction length in this composite material is approximately 88 cm. Thus, we require the short track to start from 90 cm from the edge of the detector from x and y direction. The start of the short track also represents interaction vertex where the long track starts from. So we apply the same fiducial requirement for the start x and y coordinates of the long track.

Both, the long track and the short track, are required to start between 20 and 844 cm in the z direction. The high z requirement is based on the starting point of a 3 GeV muon inside the detector that stops at the end of the detector. In other words, we project back a 3 GeV muon from the end z of the detector to find out where it started in the z direction. This starting point coincides with the high z requirement. The cartoons in Figure 5.4 and Figure 5.5 display the fiducial region. The fiducial requirements for both the tracks are listed in Table 5.2. The determination of containment and fiducial is unique contribution to NOνA. This data driven selection can be used for future use.

5.3.3 Forward Moving Requirement :

We require the z_{start} coordinates of both the tracks are less than their corresponding z_{end} coordinates. This ensures that an interaction is moving forward toward downstream of the detector with time.

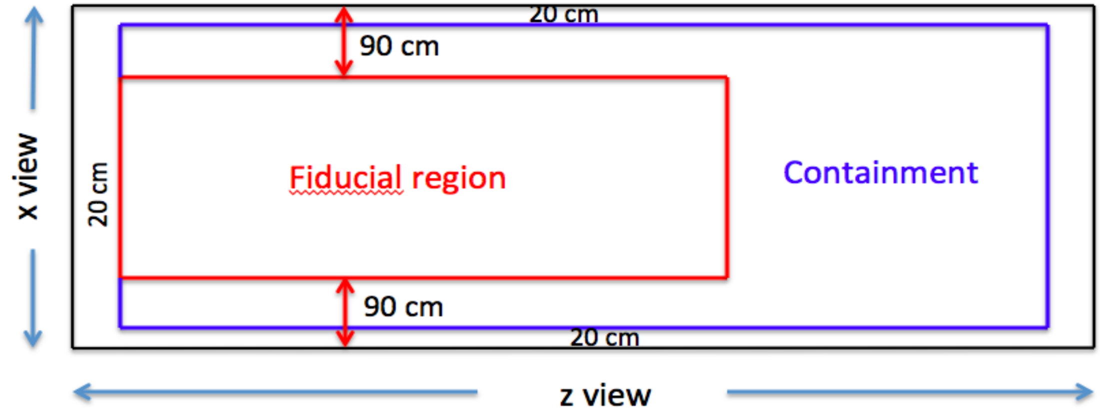

Figure 5.4 Near Detector containment and fiducial region in x-z view. The numbers are not representative of x and z scales.

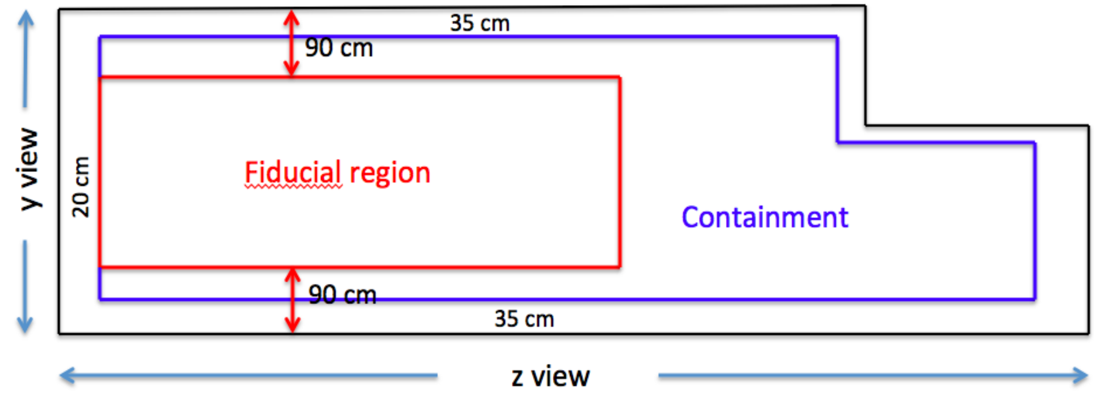

Figure 5.5 Near Detector containment and fiducial region in y-z view. The numbers are not representative of y and z scales.

Table 5.2 Containment and Fiducial selection criteria

	Start X (cm)	Stop X (cm)	Start Y (cm)	Stop Y (cm)	Start Z (cm)	Stop Z (cm)
Long track	$\|x\|$ <110	$\|x\|$ <180	$\|y\|$ <110	$\|y\|$ <165	>20 and <844	either <1275 or enters the muon catcher.
Short track	$\|x\|$ <110	$\|x\|$ <180	$\|y\|$ <110	$\|y\|$ <165	>20 and <844	either <1275 or enters the muon catcher.

5.3.4 **Vertex Requirement :**

The selection requires that the two tracks start within 10 cm of radial distance from each other to ensure both the tracks start from the same vertex. Ten cm is motivated by giving the reconstructed vertices a resolution of cell width.

5.3.5 **Energy Related Requirement :**

Both charged current and neutral current interactions may produce a 2-track topology but accompanied by either a neutron or a neutrino. Since we cannot reconstruct a neutron or a neutrino in the detector, these events mimic the signal of current analysis. Such neutrino interactions may deposit some energy outside of the two tracks. These kind of events reflect a different topology than what we are looking for. So we require that the total visible energy of two tracks carry 95% of the slice energy.

Remaining 2-track Sample

We can also plot the number of selected events as a function of the different cuts to show how much data is lost with each cut. For this plot, I broke the cuts into 5 different categories. The first cut was Basic Quality Cuts (section 5.3.1), the second was Two Track Requirement (first paragraph of section 5.3.2), the third was Containment

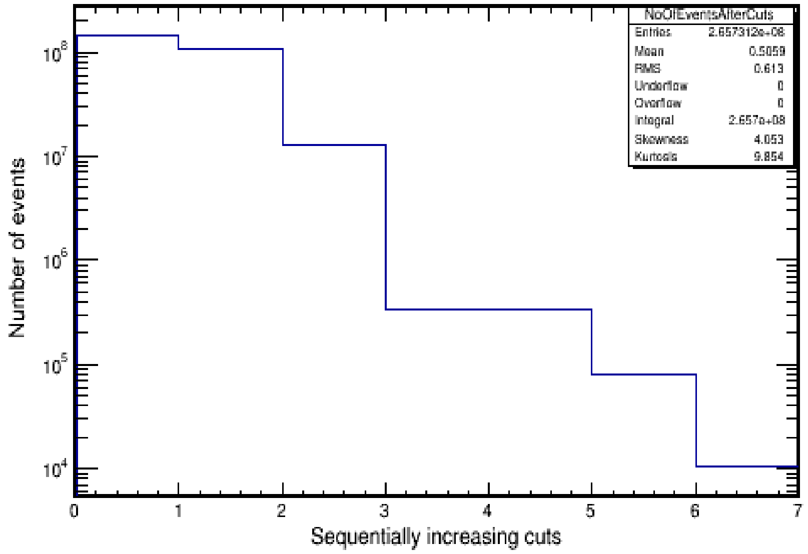

Figure 5.6 Cut progression for Data. The lines illustrate the remaining tracks after a cut.

and Fiducial Cuts (see section 5.3.2), the fourth was Forward Moving Requirement (see section 5.3.3), the fifth was Vertex Requirement (see section 5.3.4) and the last was Energy Related Requirement (see section 5.3.5). The different cuts are enumerated in the plot below as cuts 1 through 6 and 0 represents “No Cut". Figure 5.6 shows the effect of each cut on the data. We started with 28,465,324 events and we selected around 12,038 2-track events after all cuts are applied. In Figure 5.7, we present the number of selected events over accumulated POT for different run numbers. There are a 3/4 outliers in the the distribution with around 20 events per run but the number of selected events for the rest of the plot is roughly constant over time.

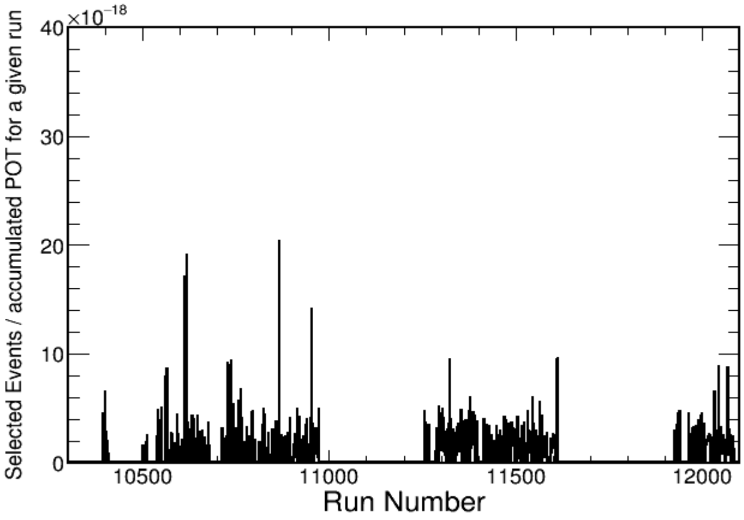

Figure 5.7 Selected events / POT vs run number .

5.4 Selection for Stopping Rock Muons

In NOνA the neutrino beam passes through 240 meters of rock before passing through the near detector. Frequently the neutrinos interact with the rock outside the detector and produce muons. These muons travel forward and enter through the front face of the detector. So we have an abundance of pure rock muon sample in the near detector. We select those rock muons stopped inside the detector and study the energy loss rate, dE/dx, of those contained muons. The study of the stopping muon will be used for calibration purpose in the Analysis chapter. Selection of these events in the near detector start with the data quality cuts described in section 5.2. The additional selection criteria of the stopping muons is outlined in the next subsections.

5.5 Reconstruction and Analysis Cuts for Rock Muons

The basic quality cuts are applied next. These cuts are same as described in section 5.3.1. The neutrino interactions with the rock upstream of the detector results in a single muon track in the detector. So the selection requires to have only one reconstructed 3D Kalman track.

5.5.1 **"Through the Face" Cut**

There exists tracks, result from interactions within the detector, that have a vertices close to the front detector planes. This cut ensures we avoid those tracks and also makes sure that the muon entered the detector through its front face. We require the reconstructed start of the track to have $z < 5$ cm.

5.5.2 **Containment Cuts**

Selecting tracks whose reconstructed end point is contained within the detector is one way of selecting stopping muons. These cuts are designed for the start and end points of the tracks to be contained within the detector. This is to further exclude tracks that are entering or exiting through the sides, top or bottom of the detector.

- The z_{end} cut of the reconstructed track is designed to completely exclude the μ catcher region of the detector. We impose Stop $Z < 1275$ cm.
- We require $|StartX| < 110$ cm and $|StopX| < 180$ cm to exclude tracks exiting through the sides.
- We require $|StartY| < 110$ cm and $|StopY| < 165$ cm to exclude tracks exiting through the sides.

The containment criteria for x and y co-ordinates follow the same principles as long track containment in section 5.3.2. Figure 5.8 shows the number of selected events as a function of the different cuts. For this plot, I broke the cuts into 3 different categories. The first cut was Basic Quality Cut (section 5.3.1), the second was Through the Face cut (section 5.5.1), the third was Containment Cut (see later in section 5.3.2). The different cuts are enumerated in the plot below as cuts 1 through 3 and 0 represents

"No Cut". We started with 28,465,324 events and we selected around 336,676 rock muon events after all cuts are applied.

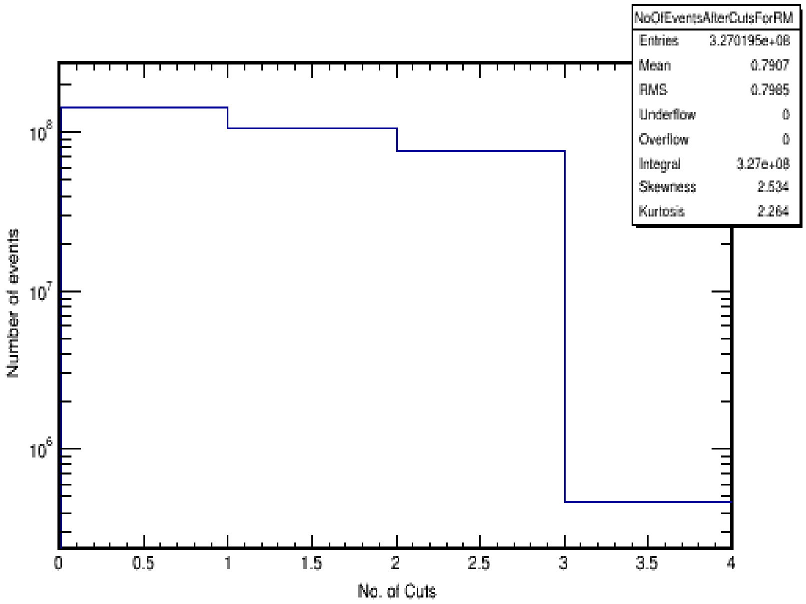

Figure 5.8 Cut progression for Data. The lines illustrate the remaining tracks after a cut.

CHAPTER 6

PARTICLE IDENTIFICATION

We need to identify the particles involved in our 2-track analysis sample. The majority of those tracks are comprised of $\mu^{\pm}$ with significant $\pi^{\pm}$ and proton population originating from different CC and NC interactions. In this chapter, first, we describe how we isolate calibration sample from stopping rock muon data and second, we present how the calibration sample is used to identify μ and proton in our 2-track analysis data as described in section 5.3.

6.1 CALIBRATION SAMPLE FROM ROCK MUON DATA

The front face of the near detector, is downstream of rock where many beam neutrinos interact. Neutrino interactions in the rock upstream of the front face of the near detector produce abundant muons that penetrate the near detector with very little contamination from other charged particles, for example, $\pi^{\pm}$, p. The selection of this rock muon data sample is described in section 5.5. Here we split the rock muon data into two subsets. The first half of the data is used for muon calibration purpose while the second half confirms the validity of the calibration.

6.1.1 Muon Identification (MID) using Michel Electrons

There are a total of 336,676 rock muon events found. We use first 168,338 events to identify pure muon and to obtain the energy loss rate (dE/dx) of those muons. To select the stopping muons, we have selected those tracks whose reconstructed end point is contained within the detector, described in section 5.4. We then look for Michel electrons coming from muons. A Michel electron is an electron produced when a muon decays at rest:

$$\mu^- = \nu_\mu + \bar{\nu}_e + e^- . \tag{6.1}$$

Michel electrons are useful for identifying muons by tagging the delayed energy deposited by an e^- at end point of a muon track. Michel electrons (MEs) are an indicator of a muon in a neutrino interaction. Muons decay to electrons with a lifetime (τ_{free}) of 2.1969811 ± 0.0000022 μs [65]. The timescale for identifying MEs is significantly longer than the timing resolution of hits of a given physics slice and also the time between physics slices in the ND. So the CellHits from Michel electrons are rarely included in the slice considered as parent physics slice and thus are not reconstructed in the primary chain of reconstruction algorithms. The algorithm for detecting Michel electrons is called the MEFinder [66]. The algorithm starts by finding a vector of candidate ME hits in the noise slice. A noise slice is any slice either tagged by Slicer4D as a noise slice or defined as number of cells ≤ 10. Hits within a noise slice must have $ADC \geq 50$ to remove electronics noise. To qualify as candidate ME hits, they must fulfill both, temporal and spatial requirements. A candidate hit is required to occur within 10μs of the mean time of the parent physics slice and also be within 40 cm of some hit in a physics slice. Once the collection of Michel hit candidates is found, the hits are clustered together using DBScan clustering algorithm [49]. MEFinder outputs two different ME clusters, TrkME and SlcME. The reconstructed Michel cluster is saved as a TrkME if it lies within a 20 cm sphere surrounding the endpoint of a reconstructed Kalman track in the physics event. The Michel electron is then associated with that track. The output TrkMEs are added into the art file during reconstruction. TrkMEs have a high purity sample that will be used for calibration and precision checks in the next chapter.

Michel electrons are not the only time-delayed physics process associated with neutrino interactions. There could be various non-Michel physics activity tagged by

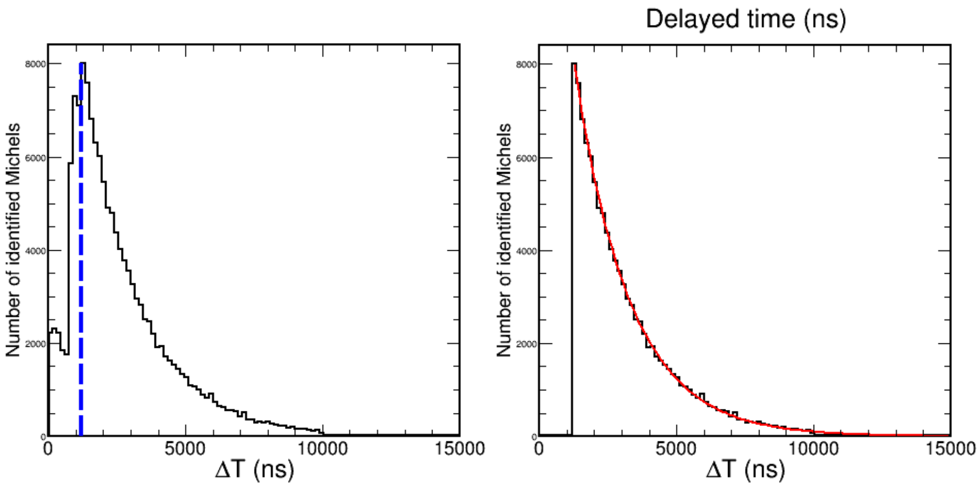

(a) (b)

Figure 6.1 The Δt distribution for reconstructed Michel clusters.

(a) The Δt distribution for Michel clusters reconstructed in the near detector for selected rock muon data. The cut is placed at $\Delta t \geq 1200$ ns and marked by blue dotted line. Events with $\Delta t < 1200$ ns are discarded to remove the any contamination caused by other activities.
(b) The muon decay data is shown with the exponential fit.

MEFinder algorithm. To further make sure we select pure muon tracks, we assign a further requirement over samples of selected muon tracks. We require the difference in time (Δt) between the track end hit and the ME cluster to be larger or equal to 1200 nanosecond ($\Delta t \geq 1200$ ns) to improve the sample purity. The Michel electron requirement and the $\Delta t \geq 1200$ ns removes 72% of the rock μ candidates. Though this cut throws away many muon events yet preserves large statistics after the cut. With this cut we expect to obtain a high purity muon sample that will be studied in the section below. Figure 6.1 right plot shows the resulting Δt distribution fitted to an exponential, $\frac{dN}{dt} = Ae^{\frac{-t}{\tau}}$. The fitting result yields a mean lifetime of $\tau = (2.00 \pm 0.18)$ μs, consistent with the μ lifetime.

6.1.2 Muon dE/dx Template

Muons in our detectors lose energy (dE/dx) following the Bethe-Bloch equation [67]. For muons which stop inside the detector the energy at various points along its track can be found. The fact that the energy loss is maximum just before a particle comes to complete rest can be used to distinguish muons from other particles. Once we select those rock muons stopped inside the detector we can study the energy loss rate, dE/dx, of those contained muons. The present analysis explores the dE/dx of selected muons at last 5 planes from the end of the track. A value of dE/dx is calculated by summing the total calibrated visible energy in a plane associated with the reconstructed track and dividing by the total path length in active material that the track goes through in that plane. The dE/dx measurement is performed on a plane level, instead of a cell by cell level, in order to avoid potential problems with the calculation of active path length that might result from reconstruction or alignment uncertainties. Using the dE/dx shape information from last 5 planes of a muon track will make it possible to distinguish muon from other particles in our analysis sample. In Figure 6.2, dE/dx is measured for last 5 planes starting from the end of the track. Five planes from the end of the track are considered only to exploit the "Bragg peak". Since the Bragg peak is pronounced in last few planes for a proton, it allows one to discriminate μ from a proton. There exists little information beyond 5 planes from the end to discriminate from one particle to other. Among the last 5 planes, we throw away information from the last plane. Since we don't know where the particle stops within a cell, we cannot extract any useful information out of it. Thus the distribution of measured dE/dx values for only 4 planes will be used in the next section to calibrate our analysis sample.

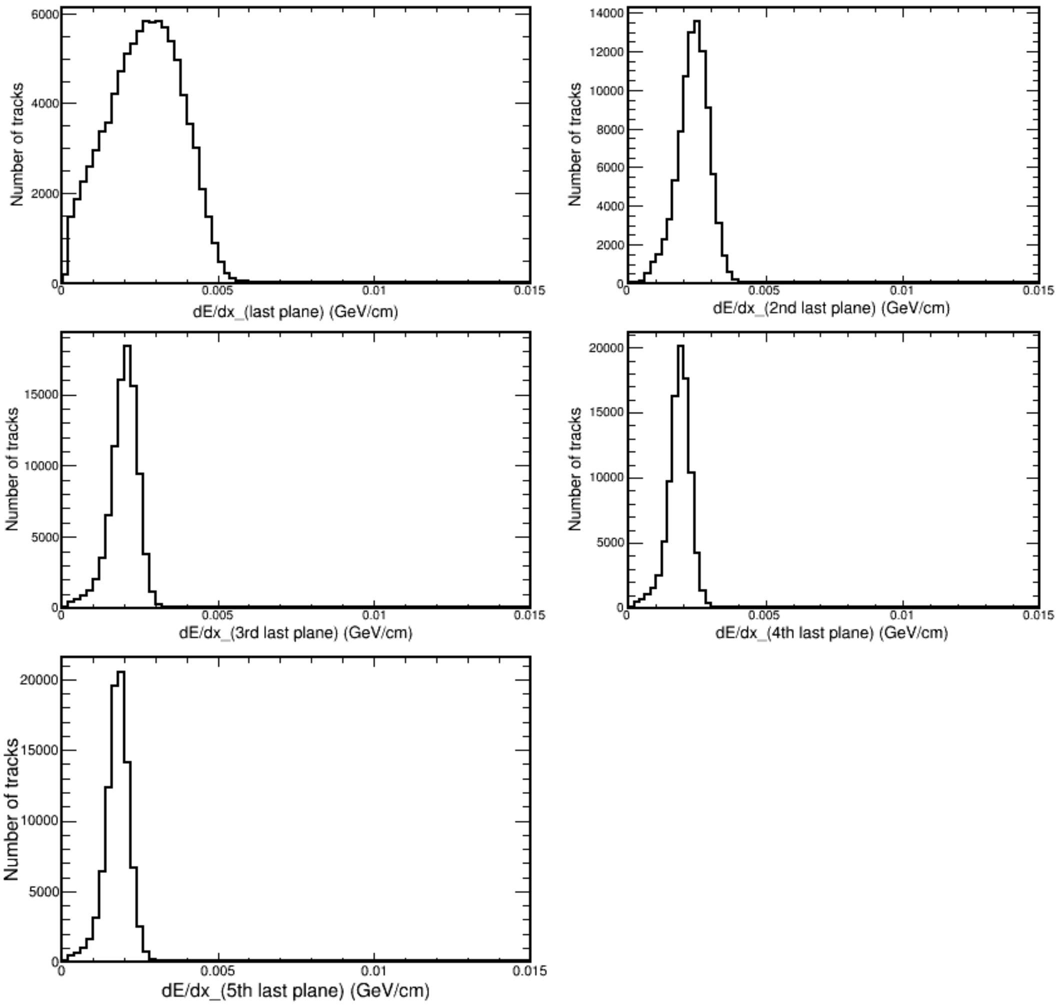

Figure 6.2 The distribution of muon dE/dx for last 5 planes is shown in the figure.

Top left: last plane from the end of the track, Top right: the 2nd last plane, Middle left: the 3rd last plane, Middle right: the 4th last plane, bottom: the 5th last plane.

6.2 Performance of MID in Confirmation Sample

We have dedicated section 6.1 to develop muon dE/dx template using the “first” half (i.e.168,338 events) of 336,676 rock muon events found in section 5.5. In this section we will address the question how efficiently we use this muon template to identify muon from a random data collection. In order to check the validity of the MID technique we use the “later” half (i.e.168,338 events) rock muon events. We apply Michel electron cut (described in section 6.1.1) on the dataset. As it stands, the sample we are currently discussing has the same selection cuts applied as calibration sample and thus guarantee that it contains muon. However, this sample remains untouched so far for the calibration purpose. We aim to check the performance of MID on this sample. What we want to confirm is, if the second set of data, upon applying identification procedure, follows the same behavior as the calibration sample.

6.2.1 **Muon Identification Variable**

The variable dE/dx log-likelihood (LL) is used to classify how close a reconstructed track’s energy deposit is like a muon. dE/dx is determined for last five planes, as discussed in section 6.1.2. As mentioned earlier, only last 5 planes of a given track are considered since those planes have discriminating power to separate different MIP particles. Because we don’t know where the muon stops in the last plane, dE/dx is discarded for the last plane of every track studied and thus, not included in the analysis.

We follow up the dE/dx measurements with what is the probablity that the energy deposition profile of any given track characterize the behavior of muons in the NOνA detector. The probability, $\mathcal{P}_i$, of a particle to have the measured dE/dx at a specific plane i from the end of the track is calculated from histograms created using muon data events from Figure 6.2. This is illustrated with a single example considering the 2nd from the last plane. First, the algorithm measures the energy deposit for the 2nd from the last plane of a track. Using the dE/dx information the probability at that specific plane is found from the normalized dE/dx histogram stored for the 2nd from the last plane for muon track. The same method is followed to find the probability for the rest of the 3th, 4th and 5th last planes. The energy measurements are performed at each plane independently. Thus the total probability for a certain particle to behave like a muon can be written as,

$$\mathcal{L} = \prod_{i=2}^{5} \mathcal{P}_i, \tag{6.2}$$

where i denotes the last 2nd to 5th plane. All these 4 planes are counted in the Log Likelihood (LL). The total log likelihood for the considered particle is calculated by

$$LL_{\text{total}} = \sum_{i=2}^{5} \log \mathcal{P}_i. \tag{6.3}$$

6.2.2 Performance

Following the procedure above we find out the log likelihood of confirmation sample. Next we compare it with the the log likelihood of the calibration sample. Once we overlay these two log-likelihood plots, we expect to see an excellent agreement in both, overall shape and normalization. Figure 6.3 shows very good agreement of the log-likelihood plots between calibration and confirmation sample. To compare these two histograms quantitatively, a χ^2 test is performed. We obtain a value of $\chi^2/NDF = 57.23/59$ from the test. This χ^2 and NDF allows us to evaluate the probability (P value) that the two distributions come from the same parent distribution. The P value for the comparison is 0.53. The value confirms the behavior of calibration sample as we expect it.

6.3 PARTICLE DETECTION USING LOG-LIKELIHOOD

The primary goal of this thesis is to identify ν_μ 2-track topology $\nu_\mu + n \to \mu^- + p$. In such events one would expect two tracks originating from the reconstructed primary vertex, one of them identified as a muon, the other one as a proton. Chapter 5 describes selection of 2-track events originate from the same vertex. This section

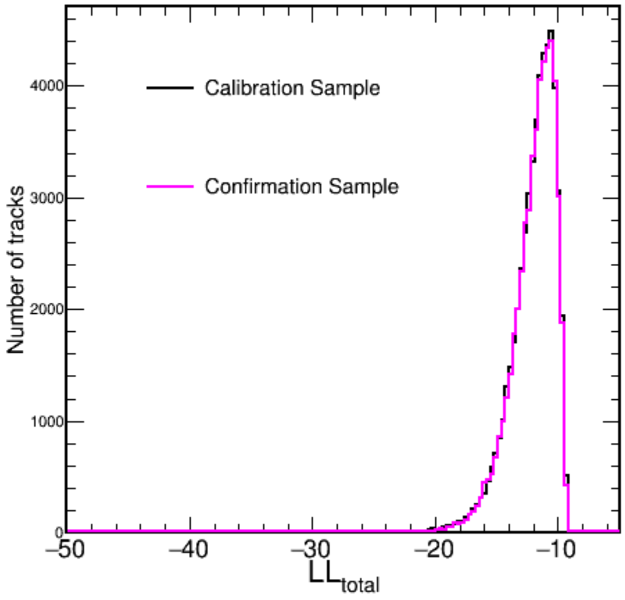

Figure 6.3 dE/dx LL_{total} distribution for calibration sample is overlaid on that of confirmation sample.

attempts to identify events where one of the track is a muon and the other one is a proton using the log-likelihood method .

6.3.1 Identifying Particles

For the ease of work flow we will first analyze the short track sample of 2-track events. Considering different CC and NC interactions, the short track is most likely populated by one of the 3 particles : either a proton or a muon or a pion. It appears to be highly challenging to distinguish a pion from a muon in a data driven fashion. So the analysis will focus on distinguishing a proton from a muon.

The dE/dx distributions for last 5 planes for a short track are shown in Figure 6.4. Note that we throw away information on very last plane. For the rest of the plots we observe there are two distinct peaks in each of those distributions. Furthermore the peak on the right moves left as we move farther from the end of the track. If compared with the distributions of Figure 6.2, it appears that the left peak of the distributions in Figure 6.4 coincides with the muon peak from calibration sample. The idea is to fit the muon in the muon-like peak of the short track sample and extract proton. To carry this idea forward we make use of log-likelihood. With the energy deposition at a given plane, we can calculate the log-likelihood of a short track using the method derived in section 6.2.1. The right plot of Figure 6.5 is the log-likelihood distribution for the short track events and the left plot is that of calibration sample. Log-likelihood returns a value between -50 and 0. A fine observation again reveals that the calibration peak occurs at the same place as the right peak of the short track sample in Figure 6.5. This leads us to recognize the sharp peak in the short track sample at log-likelihood value of -10 and close as muonic. Based on this observation we can claim the right peak of Figure 6.5 right plot is more muon-like and the left peak of the same figure is more proton like. The next step would be relating the observation to a fitting procedure that aims to fit the muon log-likelihood distribution to that of the short track.

The procedure involves two steps. The first step is to determine the range of the fitting and the second one is performing it. Since the peak occur at -10 for both the plots, the range -14 to -8 for the fitting region seem reasonable. In order to fit in that specified range we also need a scaling factor to apply on calibration sample. This scaling factor is determined by following the minimum χ^2 technique. χ^2 is calculated by

$$\chi^2 = \sum_i \frac{(s \times LL_i^{\text{calib}} - LL_i^{st})^2}{\sigma_i^2}, \tag{6.4}$$

where s is a scaling factor, LL_i^{calib} represents the bin content of the ith bin from calibration plot, LL_i^{st} represents the same but from the short track data and σ_i^2 is the variance, defined by the following equation

$$\sigma_i^2 = (\sigma_{\text{calib}}^2 + \sigma_{\text{st}}^2), \tag{6.5}$$

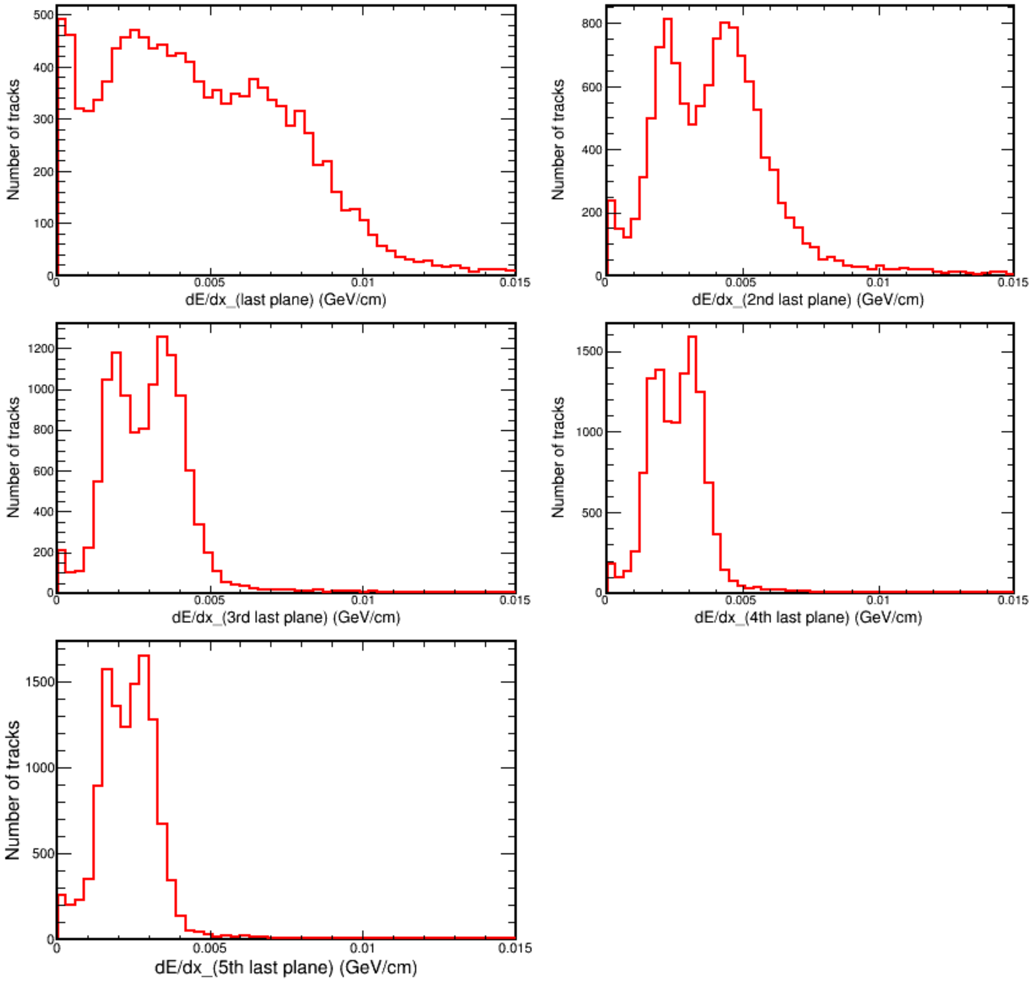

Figure 6.4 The distribution shows “short track” dE/dx for different planes.

Top left: last plane from the end of the track, Top right: the 2nd last plane, Middle left: the 3rd last plane, Middle right: the 4th last plane, bottom: the 5th last plane.

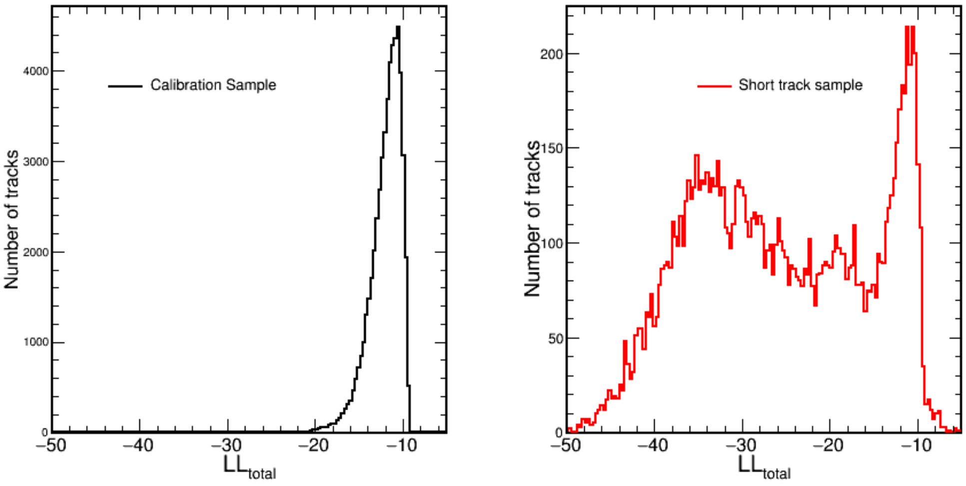

Figure 6.5 Left: Presented is the diagram of LL_{total} for calibration sample. Right: The plot in red represents LL_{total} for short track data.

where $\sigma_{\text{calib}} = \sqrt{s \times LL_i^{\text{calib}}}$ and $\sigma_{\text{st}} = \sqrt{LL_i^{st}}$. The measured χ^2 is the summation of individual contribution of χ^2 in each bin in the range of $-14 \leq LL_{total} \leq -8$. A scale factor s is now determined by minimizing χ^2. The value of s from the fit is applied to the LL_{total} distribution of muon to normalize that of the short track. With the fitting a total of χ^2/N_{dof} of 66.9763/20 is achieved. The resulting distribution is shown on left of Figure 6.6. At this point a pertinent question to ask would be if we can extract a proton template out of the short track data. To address this we subtracted the muon log-likelihood from the short track log-likelihood after performing the fitting procedure to extract only protons. The Figure that results from this method is displayed in Figure 6.6. With this we separate candidates into muon and proton population.

So far the technique we have followed to separate muon from proton is statistical. Next we would like to attempt to identify particle types such as a proton or muon event by event. One way to do this would be to make a selection based on log-likelihood values of an event. We choose the value $LL_{total} = 16$ and we require any

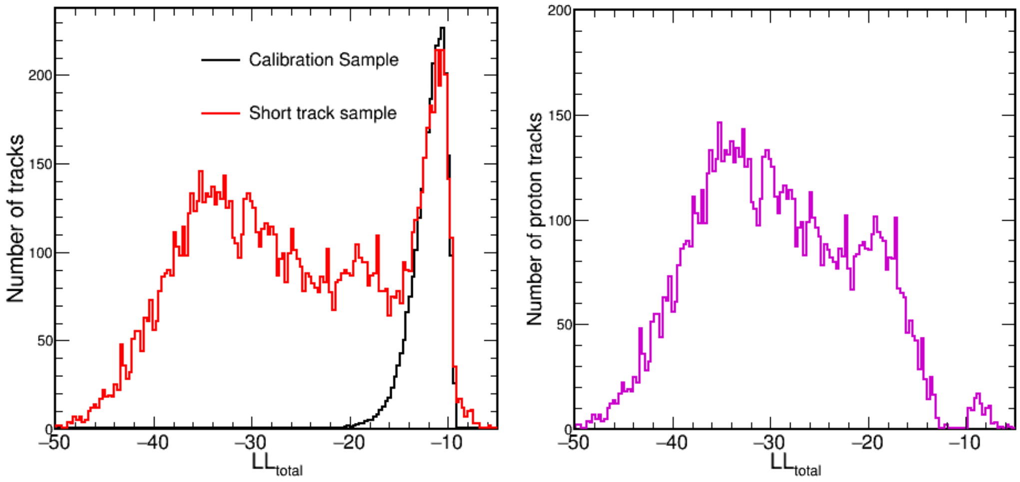

(a)

(b)

Figure 6.6 The left diagram displays the LL_{total} for short track sample overlaid with that of calibration sample. The right diagram showcases LL_{total} for proton.

(a) LL_{total} of short track data is drawn in red color. A fitting procedure is then performed using the LL_{total} of calibration sample. The calibration sample is scaled down to fit the peaks of both the sample in the range $-14 \leq LL_{total} \leq -8$. The fitting technique uses minimum χ^2 method.
(b) Proton sample is derived by subtracting the muon LL_{total} from short track LL_{total}. The area under the purple curve represents proton population.

track with $LL_{total} > -16$ is considered as muon and $LL_{total} < -16$ as proton. We overlay the LL_{total} plots for muon, proton and short track in Figure 6.7. Though the right side of the blue dotted line is muon side the left side is for proton, there's some overlap between proton and muon in the range. This overlap introduces some contamination on both sides.

After we have achieved the technique to identify a proton and a muon, we will move on to consider long track events. The same method, as described in section 6.2.1 is followed to calculate log-likelihood of long tracks. dE/dx for last few planes for the long track sample are displayed in Figure 6.8. Using this information the LL_{total} is calculated and displayed in Figure 6.9. The red dotted line at $LL_{total} = -16$ marks

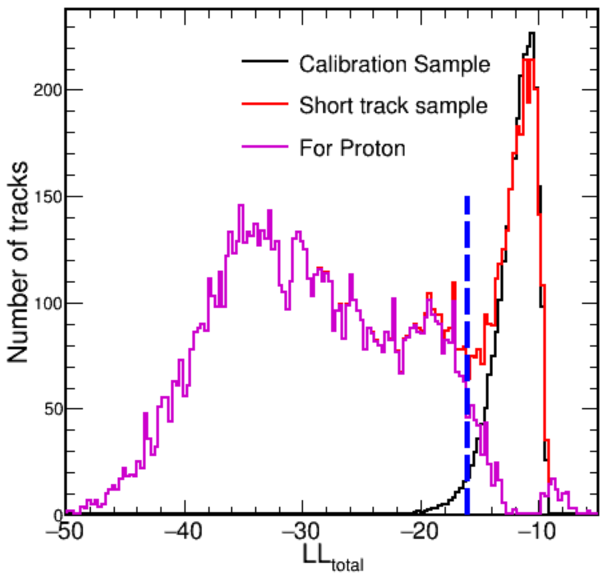

Figure 6.7 The figure displays the LL_{total} of short track overlaid with that of calibration and proton sample.

The purple represents proton curve and the black line is scaled down muon curve. The red line shows the result when overlaid both samples together. The blue dashed vertical line indicates the separation of candidates into a muon and proton population.

a distinction between muons on the right side and protons on the left. With that said, there's still a small amount of contamination underlying in the muon track. To determine the underlying proton contamination on the muon track, we subtract the muon from the long track sample.

6.3.2 Efficiencies and Uncertainties

Efficiency For Identifying Proton

The proton efficiency is defined by

$$\epsilon_p = \frac{\text{Number of correctly identified protons}}{\text{Total Number of protons}}. \tag{6.6}$$

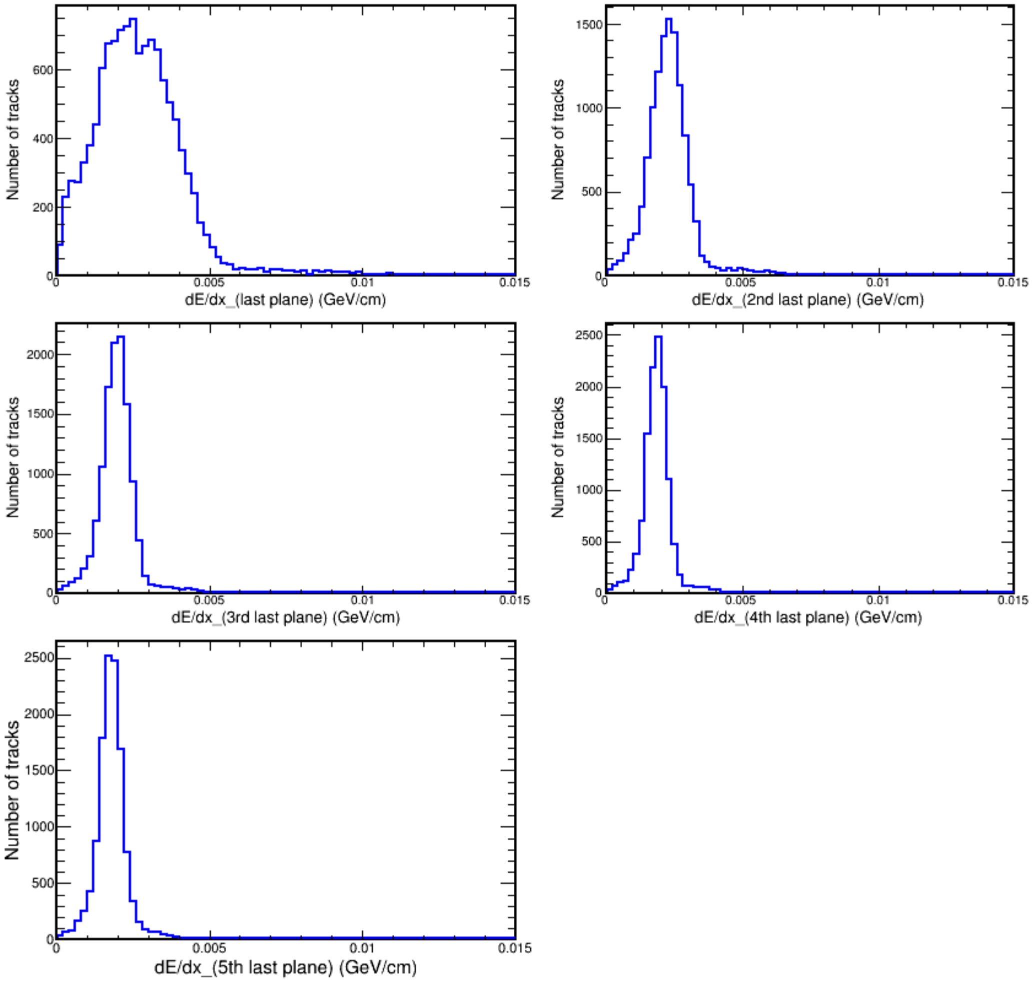

Figure 6.8 The distribution shows “long track” dE/dx for different planes.

The distribution displays “long track” dE/dx for different planes. Top left: last plane from the end of the track, Top right: the 2nd last plane, Middle left: the 3rd last plane, Middle right: the 4th last plane, bottom: the 5th last plane.

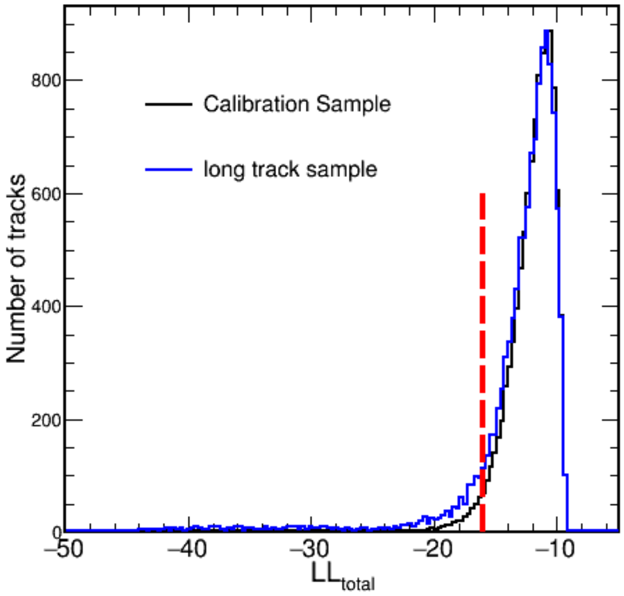

Figure 6.9 The muon curve (black line) is scaled down to fit the long track (blue curve). The red dashed vertical line separates the muons on the right side from other candidates on the left.

We write the ϵ_p in terms of integrals under different curves from Figure 6.7 so we can visualize the measured integral as

$$\epsilon_p = \frac{\int_{-50}^{-16} \text{Proton Curve}}{\int_{-50}^{-5} \text{Proton Curve}}. \tag{6.7}$$

The proton efficiency for the entire dataset is found to be 97.08%.

Efficiency For Identifying Muon

The muon efficiency is defined by

$$\epsilon_{\mu^-} = \frac{\text{Number of correctly identified muons}}{\text{Total number of muons}}. \tag{6.8}$$

We write the ϵ_μ in terms of integrals under different curves from Figure 6.9 so we can visualize the measured integral as

$$\epsilon_{\mu^-} = \frac{(\int_{-16}^{-5} \text{Long Track Curve} - \int_{-16}^{-5} \text{Proton Contamination from Long Track Curve}}{\int_{-50}^{-5} \text{Muon Curve}}. \tag{6.9}$$

The muon efficiency is measured as 96.70%.

Uncertainties on Efficiencies

The uncertainty is propagated following the standard rules. The denominator in Equation 6.7 can be rewritten as :

$$\begin{aligned}\epsilon_p &= \frac{\int_{-50}^{-16} \text{Proton Curve}}{\int_{-50}^{-5} \text{Proton Curve}} \\ &= \frac{\int_{-50}^{-16} \text{Proton Curve}}{(\int_{-50}^{-16} \text{Proton Curve} + \int_{-16}^{-5} \text{Proton Curve}}. \qquad (6.10)\end{aligned}$$

To estimate the uncertainty on efficiency, we rewrite Equation 6.10 by replacing the numerator with i and the denominator with $i+m$. i stands for particles identified and m stands for the same particle but misidentified. Thus the elements of the efficiency can be written as

$$\epsilon_p = \frac{i}{i+m}. \qquad (6.11)$$

The uncertainty now can be calculated using the following formula

$$\delta\epsilon_p = [(\frac{\delta\epsilon}{\delta i})^2\ \delta i^2 + (\frac{\delta\epsilon}{\delta m})^2\ \delta m^2)]^{\frac{1}{2}}, \qquad (6.12)$$

where

$$\frac{\delta\epsilon}{\delta i} = \frac{2i+m}{(i+m)^4} \quad \textit{and} \quad \frac{\delta\epsilon}{\delta m} = \frac{i}{(i+m)^2}. \qquad (6.13)$$

Replacing the differentials of Equation 6.12 with Equation 6.13 and plugging in the values for i and m, the uncertainties associated with the proton efficiency is calculated as:

$$\epsilon_p \pm \delta\epsilon_p = 97.08\% \pm 2.0\%. \qquad (6.14)$$

Following the same technique the uncertainty on muon efficiency calculation is found

$$\epsilon_{\mu^-} \pm \delta\epsilon_{\mu^-} = 96.70\% \pm 1.6\%. \qquad (6.15)$$

This suggests that the selection efficiency of finding a muon and a proton outweighs the negative impact of misidentifying a muon as proton and a proton as a muon. The above efficiencies will be used in calculating the cross-section ratio.

6.4 CHAPTER SUMMARY

In this chapter we have outlined how we determine the identity of a particle seen in our sample and measured the efficiency for that particle once a track is found. In the next chapter we will use this information to determine the cross section ratio.

CHAPTER 7

ANALYSIS RESULT

7.1 MEASUREMENT OF CROSS-SECTION RATIO

A total of 12038 CCQE 2-track candidate events have been selected in the data sample, discussed in chapter 5. In chapter 6 we have achieved the ability to identify each particle of all 2-track events. This equips us to calculate the cross-section ratio. The cross section ratio we are going to measure is expressed as,

$$R_\sigma = \frac{\sigma(\nu_\mu n \to \mu^- p)}{\sigma(\nu_\mu n \to \text{2track})}. \tag{7.1}$$

First, we will focus on the denominator. The experiment cannot measure the fundamental interaction but only the final state particles after nuclear effects. All we observe for $\sigma(\nu_\mu n \to \text{2track})$ topology is two tracks originating from the reconstructed primary vertex. Events with such a topology can arise due to various interaction processes. We will take a look at those processes, listed in Table 7.1, so we can break down $\sigma(\nu_\mu n \to \text{2track})$ into specific observable final states.

There are many more that gives rise to 2-track event but are not listed in the table. Of all those processes that majorly contribute to the all 2-track events in the range NOνA operates are CCQE and CCRES and NCRES. So we write Equation 7.1 by splitting $\sigma(\nu_\mu n \to \text{2track})$ into different major components:

$$\begin{aligned} R_\sigma &= \frac{\sigma(\nu_\mu n \to \mu^- p)}{\sigma(\nu_\mu n \to \text{2track})} \\ &= \frac{\sigma(\mu^- p)}{\sigma(\mu^- p) + \sigma(p\pi^-) + \sigma(\mu^-\pi^+) + \sigma(\pi^+\pi^-) + \sigma(\mu^+\mu^-)}, \end{aligned} \tag{7.2}$$

Table 7.1 Interactions that contribute to 2 tracks in the final state

	Interaction type	Interaction detail	Final state observables
1	CCQE	$\nu_\mu + n \to \mu^- + p$	the most obvious.
2	CCRES	$\nu_\mu + n \to \mu^- + n + \pi^+$	neutron is invisible producing only 2-tracks.
3	CCRES	$\nu_\mu + p \to \mu^- + p + \pi^+$	the pion can be reabsorbed in the nucleus leaving only 2 tracks.
4	NCRES	$\nu_\mu + n \to \nu_{\mu^-} + p + \pi^-$	neutrino is invisible, leaving only 2 tracks.
5	NC	$\nu_\mu + n \to \nu_{\mu^-} + \pi^+ + \pi^-$	neutrino is invisible, leaving only 2 tracks.
6	NC	$\nu_\mu + n \to \nu_{\mu^-} + \mu^+ + \mu^-$	neutrino is invisible, leaving only 2 tracks.
7	CCCoherent	$\nu_\mu + A \to \mu^- + A + \pi^+$	low-Q^2 interactions produce no nuclear recoil with only 2 tracks.

where we have used the notation that only includes the final state particles. Because this analysis cannot distinguish a muon from a pion, we write 1st and 2nd term in the denominator as $\sigma(\nu_\mu n \to \mu^- p)$ and the last 3 terms in the denominator as $\sigma(\nu_\mu n \to \mu^- \pi^+)$. With the same reasoning the numerator is not just $\mu^- p$ but it is a mixture of $\mu^- p$ and $\pi^- p$. This allows us to rewrite the Equation 7.2 as

$$R_\sigma = \frac{\sigma(\nu_\mu n \to \mu^- p)}{\sigma(\nu_\mu n \to \mu^- p) + \sigma(\nu_\mu n \to \mu^- \pi^+)}. \tag{7.3}$$

The cross-section is estimated using

$$\sigma = \frac{(N^{\text{data}}_{\text{selected}} - B)}{\epsilon \times \Phi \times N_{\text{nucleons}}}, \tag{7.4}$$

where $N^{\text{data}}_{\text{selected}}$ and B represent the number of selected events and the estimated number of background events, ϵ is the signal selection efficiency, Φ stands for neutrino flux and N_{nucleon} is the number of nucleon targets in the fiducial volume. Since our analysis is measuring cross-section ratio, the denominator $N_{\text{nucleons}} \times \Phi$ cancel each other while computing the ratio. Inserting Equation 7.4 in Equation 7.3, we can rewrite Equation 7.3 :

$$R_\sigma = \frac{\frac{N^{(\mu^- p)}_{\text{selected}} - B^{(\mu^- p)}}{\epsilon_{\mu p}}}{\frac{N^{(\mu^- p)}_{\text{selected}} - B^{(\mu^- p)}}{\epsilon_{\mu p}} + \frac{N^{(\mu^- \pi^+)}_{\text{selected}} - B^{(\mu^- \pi^+)}}{\epsilon_{\mu \pi}}}. \tag{7.5}$$

Again, $\epsilon_{\mu p}$ can be written as a product of ϵ_μ and ϵ_p for the current analysis technique. Equation 7.5 now takes the form

$$R_\sigma = \frac{\frac{N^{(\mu^- p)}_{\text{selected}} - B^{(\mu^- p)}}{\cancel{\epsilon_{\mu}} \times \epsilon_p \times \cancel{\epsilon_{geom}}}}{\frac{N^{(\mu^- p)}_{\text{selected}} - B^{(\mu^- p)}}{\cancel{\epsilon_{\mu}} \times \epsilon_p \times \cancel{\epsilon_{geom}}} + \frac{N^{(\mu^- \pi^+)}_{\text{selected}} - B^{(\mu^- \pi^+)}}{\cancel{\epsilon_{\mu}} \times \epsilon_{\pi+} \times \cancel{\epsilon_{geom}}}}. \tag{7.6}$$

Equation 7.6 equips us with all the pieces required to compute the cross-section ratio. We will take a detailed look at each term in the ratio expression. Now we proceed to calculate the individual terms in Equation 7.6.

Calculating $[N^{(\mu^- p)}_{\textbf{selected}} - B^{(\mu^- p)}]$

We obtain the $N^{(\mu^- p)}_{\text{selected}}$ by using the PID, developed in previous chapter, to select a μ^- and a p from 2-track events in various combination as shown in Table 7.2 and Figure 7.1. The last column in Table 7.2 lists various combinations of two tracks, one being a muon and the other a proton. Adding up, a total of 8776 "muon-proton" is found. A correction factor, B, is calculated to account for the purity from Figure 6.7.

Table 7.2 Characterizing $\mu^- p$ events.

	μ^- ID	pID	Types of Events found
Long Track Short Track	1 0	0 1	muon-proton found
Long Track Short Track	0 1	1 0	proton-muon found

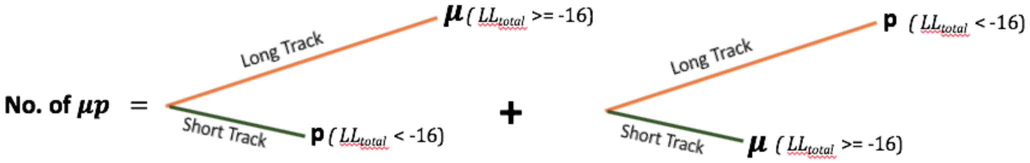

Figure 7.1 Characterizing $\mu^- p$ events.

$$\begin{aligned} B^{(\mu^- p)} &= \int_{-50}^{-16} \text{Muon(Calibration) Curve} + \int_{-16}^{-5} \text{Proton Curve} \\ &= 422.0. \end{aligned} \tag{7.7}$$

If we denote $(N_{\text{selected}}^{(\mu^- p)} - B^{(\mu^- p)}) = \text{obs.}(\mu^- p)$, the uncertainty on $\text{obs.}(\mu^- p)$ is determined by

$$\begin{aligned} \delta\left(\text{obs.}(\mu^- p)\right) &= \sqrt{N_{\text{selected}}^{(\mu^- p)} + B^{(\mu^- p)}} \\ &= \pm 95.90. \end{aligned} \tag{7.8}$$

Table 7.3 summarizes the features of the selected muon-proton samples.

Table 7.3 Related numbers on $\mu^- p$ selection.

Sample	Total number
Selected μ^- p [$N^{(\mu^- p)}_{\text{selected}}$]	8776.0 ± 93.68
Bkg. $B^{(\mu^- p)}$	422.0 ± 20.54
$N^{(\mu^- p)}_{\text{selected}}$ - $B^{(\mu^- p)}$	8354.4 ± 95.90

Calculating $[N^{(\mu^-\pi^+)}_{\textbf{selected}} - B^{(\mu^-\pi^+)}]$

Due to their similar mass, disentangling a pion from a muon is difficult. This analysis does not try to differentiate between a muon and a pion. For now, this has been dealt with applying a subtle logic to our 2-track analysis sample. We use the same selection criteria for selecting a pion as a muon. If our selection can identify one track as muon and the other one as "non-proton" but as "muon", we call the event a $\mu\pi$. With that said, one could argue that particular event could be a $\mu\mu$ by virtue of selection criterion. The PID is run to select a μ^- and a π^+ from 2-track events as shown in Table 7.4 and Figure 7.2. We found a total of 2417 $\mu^-\pi^+$ events.

Table 7.4 Characterizing $\mu^-\pi^+$ events.

	μ^- ID	pID	Types of Events found
Long Track	1	0	muon-pion found
Short Track	1	0	

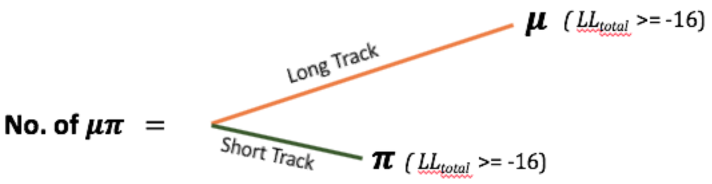

Figure 7.2 Characterizing $\mu^-\pi^+$ events.

A correction factor B is calculated to account for the purity from Figure 6.7.

$$\begin{aligned} B^{(\mu^-\pi^+)} &= \int_{-16}^{-5} \text{Proton Curve} \\ &= 312.52. \end{aligned} \tag{7.9}$$

Denoting $(N^{(\mu^-\pi^+)}_{\text{selected}} - B^{(\mu^-\pi^+)}) = \text{obs.}(\mu^-\pi^+)$, the uncertainty on obs.$(\mu^-\pi^+)$ is calculated as,

$$\begin{aligned} \delta\left(\text{obs.}(\mu^-\pi^+)\right) &= \sqrt{N^{(\mu^-\pi^+)}_{\text{selected}} + B^{(\mu^-\pi^+)}} \\ &= \pm 52.24. \end{aligned} \tag{7.10}$$

Table 7.5 summarizes the features of the selected muon-pion samples.

Table 7.5 Numbers on $\mu^-\pi^+$ selection.

Sample	Total number
Selected $\mu^-\pi^+$ [$N^{(\mu^-\pi^+)}_{\text{selected}}$]	2417 ± 49.16
Bkg. $B^{(\mu^-\pi^+)}$	312.52 ± 17.67
$N^{(\mu^-\pi^+)}_{\text{selected}} - B^{(\mu^-\pi^+)}$	2104.48 ± 52.24

Obtaining ϵ_{μ^-} and ϵ_p

The efficiencies and related uncertainties are discussed in section 6.3.1 and summarized in Table 7.6.

Table 7.6 Efficiencies of identified particles

	Efficiency	Uncertainty
ϵ_p	97.08%	2.0%
ϵ_{μ^-}	96.70%	1.8%

Computing R_σ

The calculated values derived from the expressions above result in $R_\sigma = 0.798$. The fractional uncertainty δR_σ is computed by propagating the fractional errors in the numerator and the denominator of R_σ. This results in

$$\frac{\delta\ R}{R} = 0.031 \tag{7.11}$$

$$\rightarrow \qquad \delta R = 0.798 \times 0.031 = 0.024. \tag{7.12}$$

A full data analysis yield the following cross-section ratio

$$R = 0.798 \pm 0.024, \tag{7.13}$$

where the uncertainty is statistical only.

7.2 KINEMATIC DEPENDENCE OF CROSS-SECTION RATIO

The previous section computes the cross-section ratio after subtracting off the background and the efficiency correction. In this section, we want to understand the kinematic dependence of the measured cross-section ratio on muon final state kinematics. First, the kinetic energy (T_μ) of muon is considered as one of the final state muon kinematics. We ask what the kinetic energy distribution of muon from signal-like events look like. For all the signal-like events, the dataset is divided into two at the mean of the distribution. Each dataset is then subsequently split into two at the means of the new distributions. The purpose is to distribute the signal-like events into 4 different subsets equally populated. The events are finally grouped into 4 bins of μ kinetic energy, $0 < T_\mu < 0.7$ GeV, $0.7 < T_\mu < 1.1$ GeV, $1.1 < T_\mu < 1.6$ GeV and $1.6 < T_\mu < 4.0$ GeV. Once we divide our sample into 4 different bins, we plot 4 "log-likelihood" distributions for muons corresponding to events in each bin. The log-likelihood distributions allow us to calculate the expected number of signal and background for the individual bin. The cross section ratio is measured using a formula described in Equation 7.4 in each bin of the kinetic energy of muon. The cross-section ratio measurement as a function of muon final state kinematics is shown in Figure 7.3 and the values are reported in Table 7.7. The data shown here are drawn only with the statistical uncertainties.

The same analysis technique is followed to investigate the ratio in various kinematic region of angles of outgoing muons with respect to beam axis. The result of the analysis is presented in Figure 7.4 and reported in Table 7.8.

7.3 SYSTEMATIC UNCERTAINTIES

To finish the analysis, we must understand and quantify the systematic errors. Systematic errors allow us to determine the uncertainty our measurement has due to approximations and unknowns in our analysis. The sources of systematic uncertainties, considered for now and discussed below, in this analysis will have an impact on the final uncertainty of our measurement.

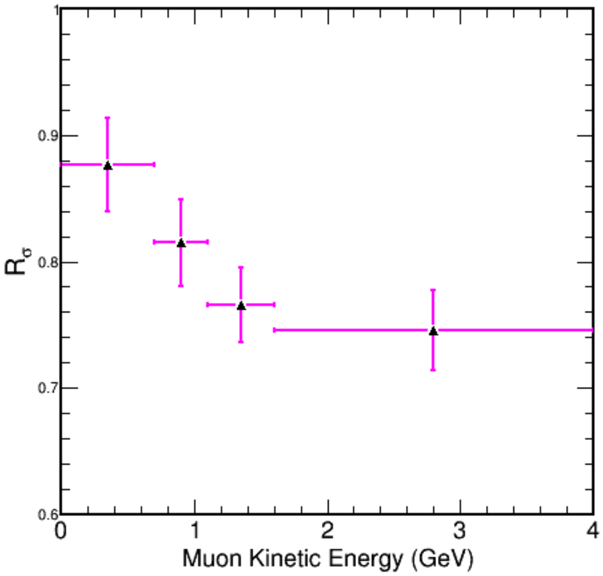

Figure 7.3 The figure displays the cross-section ratio measurement as a function of muon kinetic energy in variable bin width.

The data, only with statistical uncertainty, is shown in magenta.

Table 7.7 Reported is the measured cross-section ratio values for variable T_μ bins and the corresponding uncertainties.

T_μ **(GeV)**	R_σ	**Stat Unc.**
(0.0, 0.7)	0.876	±0.036
(0.7, 1.1)	0.814	±0.033
(1.1, 1.6)	0.765	±0.029
(1.6, 4.0)	0.746	±0.031

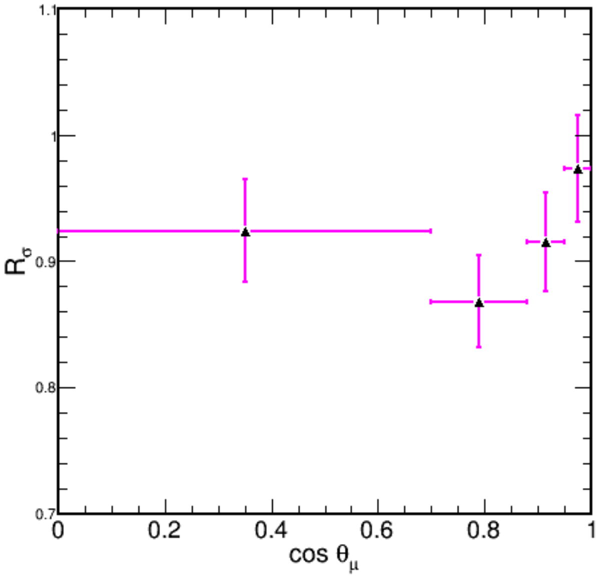

Figure 7.4 The figure shows the cross-section ratio measurement as a function of muon cosine theta in variable bin width.

The data, only with statistical uncertainty, is shown in magenta.

Table 7.8 Reported is the measured cross-section ratio values for different $\cos\theta_\mu$ bins and the corresponding uncertainties.

$\cos\theta_\mu$	R_σ	**Stat Unc.**
(0.0, 0.7)	0.924	±0.040
(0.7, 0.88)	0.868	±0.036
(0.88, 0.95)	0.915	±0.038
(0.95, 1.0)	0.973	±0.042

7.3.1 Absolute Energy Scale Offset

The calibration procedure described in chapter 4 determines the absolute energy scale that converts the attenuation corrected light signal measured in the cells to an energy deposited in the scintillator of the cell. How well the absolute energy scale was determined by this procedure, is a subject of uncertainty. Past studies with well known energy deposition such as the reconstructed π^0 mass peak in the near detector [68], Michel electron calibration study in the ND [69] show that a $\sim 5\%$ uncertainty exists in the absolute energy scale determined by the detector calibration. This uncertainty in the absolute energy scale gets propagated as we advance through the reconstruction chain and affects the estimated energy of selected events, for example, the selected muon energy, which is “not” based on track length. It would also shift any reconstructed track energy and therefore the reconstructed neutrino energy. The chances are high that it can hamper efforts to identify muons by looking at the energy deposition along the length of a track. So Shifts in absolute calorimetric energy scale of $\pm 5\%$ will be applied to account for the absolute calibration offset. The shifts and the corresponding values are given in Table 7.9 and 7.10.

7.3.2 Detector Composition

We will see more or less neutrino interactions and more or less energy deposition if our detectors are more or less dense than we expect. The extrusions and glue, that account for 36% and the scintillator, that accounts for 63% of the near detector mass, contribute to the uncertainties in the mass of the NOνA detector. The uncertainties on mass accounting, the elemental composition and the inhomogeneity in scintillator material can be the potential source to change the dE/dx, that eventually translates into the reconstructed energy of muon. These errors result in a 0.7% uncertainty [70]. Table 7.9 and 7.10 summarizes the errors and the effect on the cross section ratio.

7.3.3 Error on Particle Identification Parameter LL_{total}

The uncertainties on cut value of LL_{total}, used for particle identification, can potentially impact the signal and background distributions in every bin. To assess the impact this uncertainty has on the cross-section ratio measurement, we alter the value of LL_{total} by ±1. The corresponding uncertainties are summarized in Table 7.9 and 7.10.

Table 7.9 Reported is the measured cross-section ratio and the systematic uncertainties in variable bin width of T_μ.

Source of Uncertainty	**Variation**	T_μ (GeV) (0.0, 0.7)	T_μ (GeV) (0.7, 1.1)	T_μ (GeV) (1.1, 1.6)	T_μ (GeV) (1.6, 4.0)
Central Value		0.8761	0.8147	0.7658	0.7461
Abs. Calibration	±5%	−0.00003 −0.0046	+0.0127 −0.0035	−0.0033 −0.0006	+0.0064 −0.0089
Det. Composition	±0.73%	+0.0006 −0.0007	+0.0158 +0.0005	−0.0006 −0.0024	+0.0059 +0.0010
LL_{total}	±1	+0.0074 −0.0095	+0.0108 −0.0072	+0.0103 −0.0050	+0.0086 −0.0157

We report the central values of the cross-section ratio in 4 different T_μ bins. The sources of only systematic errors and the corresponding uncertainties are reported in comparison to the central values. All values are reported with large number of significant figures.

7.4 RESULT

We notice from Section 7.3 that the systematic uncertainties are very small. It is also apparent from Table 7.9 that the uncertainties are asymmetric for uniform variation of a given source of error. To select the uncertainties conservatively we pick the larger of the 2 uncertainties. The largest contributions to the systematic uncertainty in the measurement of cross section ratio in variable T_μ bins are presented in Table 7.11.

Table 7.10 Reported is the measured cross-section ratio and the systematic uncertainties in variable bin width of $\cos\theta_\mu$.

Source of Uncertainty	**Variation**	$\cos\theta_\mu$ (0.0, 0.7)	$\cos\theta_\mu$ (0.7, 0.88)	$\cos\theta_\mu$ (0.88, 0.95)	$\cos\theta_\mu$ (0.95, 1.0)
Central Value		0.9242	0.8682	0.9152	0.9737
Abs. Calibration	±5%	$< 10^{-6}$	$< 10^{-6}$	$< 10^{-6}$	$< 10^{-6}$
Det. Composition	±0.73%	$< 10^{-6}$	$< 10^{-6}$	$< 10^{-6}$	$< 10^{-6}$
LL_{total}	±1	$+0.0059$ -0.0080	$+0.0063$ -0.0076	$+0.0030$ -0.0033	$+0.0009$ -0.0017

We report the central values of the cross-section ratio in 4 different $\cos\theta_\mu$ bins. The sources of only systematic errors and the corresponding uncertainties are reported in comparison to the central values. All values are reported with large number of significant figures.

We recombine all the selected uncertainties from each source by adding them in quadrature. The result leads to a total uncertainty, assuming all the systematic errors are uncorrelated. The combined (stat.+syst.) uncertainties in different kinetic energy bins of muon are presented in Table 7.11. The total uncertainties (stat.+syst.) from these shifts are also shown in Figure 7.5. For each population in the Figure, the cross-section ratio spectrum in the near detector is drawn with the resulting uncertainty shown as a vertical line.

Given that the effects of absolute calibration and detector composition are negligible in Table 7.10, no systematic error will be taken for those source of uncertainties. Only the larger of LL_{total} uncertainty contributes to the systematic uncertainty in the measurement of cross section ratio in variable $\cos\theta_\mu$ bins, presented in Table 7.12. The total uncertainty (stat.+syst.) from all the shifts is determined following the same technique as before and is shown in Figure 7.6. The result for the total cross section ratio is 0.798±0.024 (stat) ±0.009 (syst). In describing the result to be found, the Figures and Tables are conveyed in the following pages.

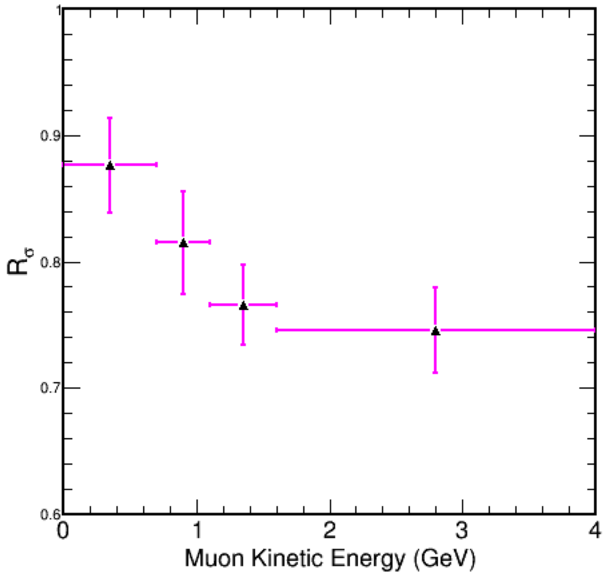

Figure 7.5 Shown here is the cross-section ratio measurements as a function of variable bin width of muon kinetic energy.

The data is presented with combined uncertainty (stat.+syst) and is shown in magenta.

7.5 SUMMARY

We have analyzed data from the NOνA near detector to obtain the ratio of cross section, $R_\sigma = \frac{\sigma(\nu_\mu n \to \mu^- p)}{\sigma(\nu_\mu n \to 2\text{track})}$. We obtain a value of $R_\sigma = 0.798 \pm 0.024$ (stat) ± 0.009 (syst). Furthermore, we have determined the cross section ratio values in each bin of muon kinetic energy and the cosine angle of the muon. These results are model independent and may be compared with predictions from various theoretical models of nuclear effects in ν interactions.

Table 7.11 Reported is the cross-section ratio measurement in variable bin width of T_μ.

Uncertainty				
Source of Uncertainty	T_μ (GeV) (0.0, 0.7)	T_μ (GeV) (0.7, 1.1)	T_μ (GeV) (1.1, 1.6)	T_μ (GeV) (1.6, 4.0)
Central Value	0.8761	0.8147	0.7658	0.7461
Abs. Calibration	-0.00003	+0.0127	-0.0006	+0.0064
Det. Composition	+0.0006	+0.0158	-0.0006	+0.0059
LL_{total}	+0.0074	+0.0108	+0.0103	+0.0086
Combined Syst. Uncertainty	0.0074	0.0229	0.0103	0.0122
Stat. Uncertainty	0.0369	0.0339	0.0299	0.0316
Combined Uncertainty (Stat. + Syst.)	0.0376	0.0409	0.0316	0.0338

We report the central values of the cross-section ratio in 4 different T_μ bins. The sources of errors and the corresponding largest uncertainties are reported in comparison to the central values. The statistical uncertainty is also shown in the Table. Last row computes the combined [stat.+syst.] uncertainties corresponding to each central value of the cross section ratio. All values are reported with large number of significant figures.

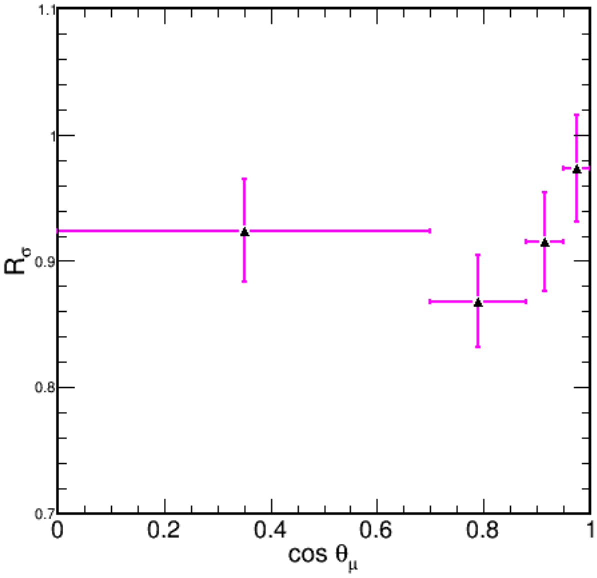

Figure 7.6 Shown here is the cross-section ratio measurement as a function of variable bin width of muon angle w.r.t. the beam axis.

The data is presented with combined uncertainty (stat.+syst) and is shown in magenta.

Table 7.12 Reported is the measured cross-section ratio in variable bin width of $\cos\theta_\mu$.

Uncertainty				
Source of Uncertainty	$\cos\theta_\mu$ (0.0, 0.7)	$\cos\theta_\mu$ (0.7, 0.88)	$\cos\theta_\mu$ (0.88, 0.95)	$\cos\theta_\mu$ (0.95, 1.0)
Central Value	0.8761	0.8147	0.7658	0.7461
LL_{total}	+0.0059	+0.0063	+0.0030	+0.0009
Combined Syst. Uncertainty	0.0059	0.0063	0.0030	0.0009
Stat. Uncertainty	0.0406	0.0362	0.0386	0.0421
Combined Uncertainty (Stat. + Syst.)	0.0410	0.0367	0.0387	0.0421

We report the central values of the cross-section ratio in 4 different $\cos\theta_\mu$ bins. The sources of errors and the corresponding largest uncertainties are reported in comparison to the central values. The statistical uncertainty is also shown in the Table. Last row computes the combined [stat.+syst.] uncertainties corresponding to each central value of the cross section ratio. All values are reported with large number of significant figures.

Bibliography

[1] W. Pauli. “Dear radioactive ladies and gentlemen”. In: *Phys. Today* 31N9 (1978), p. 27.

[2] ETH Library’s Knowledge Portal. *Wolfgang Pauli and modern physics.*

[3] C.L. Cowan et al. *Science 124 (1956) 103.*

[4] G. Danby et al. *Phys. Rev. Lett., 9:36, 1962.*

[5] K. Kodama et al. *Phys. Lett., B504:218, 2001.*

[6] B. Pontecorvo. “Inverse beta process”. In: *Camb. Monogr. Part. Phys. Nucl. Phys. Cosmol.* 1 (1991), pp. 25–31.

[7] Ziro Maki, Masami Nakagawa, and Shoichi Sakata. “Remarks on the Unified Model of Elementary Particles”. In: *Progress of Theoretical Physics* 28.5 (1962), pp. 870–880. eprint: `/oup/backfile/content_public/journal/ptp/28/5/10.1143/ptp.28.870/2/28-5-870.pdf`.

[8] K. Nakamura and S. T Petcov. *Neutrino Masses, Mixing and Oscillations.*

[9] R. N. Mohapatra and A. Y. Smirnov. “Neutrino Mass and New Physics”. In: *Ann. Rev. Nucl. Part. Sci.* 56 (2006), pp. 569–628. arXiv: `hep-ph/0603118 [hep-ph]`.

[10] M. Thomson. “Modern particle physics”. In: *Cambridge University Press, pages 8* (2013).

[11] Boris Kayser. “Neutrino Oscillation Phenomenology”. In: *Neutrinos in particle physics, astrophysics and cosmology. Proceedings, 61st Scottish Universities Summer School in Physics, SUSSP61, St. Andrews, UK, August 8-23, 2006.* 2008, pp. 51–64. arXiv: `0804.1121 [hep-ph]`.

[12] H. Nunokawa et al. “ CP Violation and Neutrino Oscillations.” In: *Prog. Part. Nucl. Phys, pages 8, 12, 13* (2007).

[13] B.P. Speakman. “ Atmospheric Electron Neutrinos in the MINOS Far Detector”. In: *PhD thesis, University of Minnesota,* (2007).

[14] P. Adamson et al. “Combined analysis of ν_μ disappearance and $\nu_\mu \to \nu_e$ appearance in MINOS using accelerator and atmospheric neutrinos”. In: *Phys. Rev. Lett.* 112 (2014), p. 191801. arXiv: `1403.0867 [hep-ex]`.

[15] K. Abe et al. “Observation of Electron Neutrino Appearance in a Muon Neutrino Beam”. In: *Phys. Rev. Lett.* 112 (2014), p. 061802. arXiv: `1311.4750 [hep-ex]`.

[16] R. B. Patterson. “The NOvA Experiment: Status and Outlook”. In: (2012). [Nucl. Phys. Proc. Suppl.235-236,151(2013)]. arXiv: `1209.0716 [hep-ex]`.

[17] Bei-Zhen Hu. “Recent Results from Daya Bay Reactor Neutrino Experiment”. In: *Proceedings, 50th Rencontres de Moriond Electroweak Interactions and Unified Theories: La Thuile, Italy, March 14-21, 2015.* 2015, pp. 229–234. arXiv: `1505.03641 [hep-ex]`.

[18] F. P. An et al. “Spectral measurement of electron antineutrino oscillation amplitude and frequency at Daya Bay”. In: *Phys. Rev. Lett.* 112 (2014), p. 061801. arXiv: `1310.6732 [hep-ex]`.

[19] Y. Abe et al. “Indication of Reactor $\overline{\nu}_e$ Disappearance in the Double Chooz Experiment”. In: *Phys. Rev. Lett.* 108 (13 2012), p. 131801.

[20] J. K. Ahn et al. “Observation of Reactor Electron Antineutrinos Disappearance in the RENO Experiment”. In: *Phys. Rev. Lett.* 108 (19 2012), p. 191802.

[21] L. Wolfenstein. “ Neutrino oscillations in matter.” In: *Phys. Rev. D, 17:2369–2374* (May1978).

[22] S. P. Mikheyev et al. “Resonant amplification of ν oscillations in matter and solar-neutrino spectroscopy.” In: *Il Nuovo Cimento C, 9(1):17–26,* (1986).

[23] A. Yu. Smirnov. “The MSW effect and matter effects in neutrino oscillations”. In: *Phys. Scripta* T121 (2005), pp. 57–64. arXiv: `hep-ph/0412391 [hep-ph]`.

[24] Davide D’Angelo. “Low Energy Neutrino Measurements”. In: *Pramana* 79 (2012), pp. 757–780. arXiv: `1211.5359 [hep-ex]`.

[25] J. N. Bahcall and M. Cribier. “The Standard Solar Model”. In: *Inside the Sun.* Ed. by Gabrielle Berthomieu and Michel Cribier. Dordrecht: Springer Netherlands, 1990, pp. 21–41. ISBN: 978-94-009-0541-2.

[26] John N. Bahcall, M. H. Pinsonneault, and Sarbani Basu. "Solar models: Current epoch and time dependences, neutrinos, and helioseismological properties". In: *Astrophys. J.* 555 (2001), pp. 990–1012. arXiv: `astro-ph/0010346 [astro-ph]`.

[27] Raymond Davis. "Solar Neutrinos. II. Experimental". In: *Phys. Rev. Lett.* 12 (11 1964), pp. 303–305.

[28] J. N. Abdurashitov et al. "Solar neutrino flux measurements by the Soviet-American Gallium Experiment (SAGE) for half the 22 year solar cycle". In: *J. Exp. Theor. Phys.* 95 (2002). [Zh. Eksp. Teor. Fiz.122,211(2002)], pp. 181–193. arXiv: `astro-ph/0204245 [astro-ph]`.

[29] F. Kaether et al. "Reanalysis of the GALLEX solar neutrino flux and source experiments". In: *Phys. Lett.* B685 (2010), pp. 47–54. arXiv: `1001.2731 [hep-ex]`.

[30] Y. Fukuda et al. "Evidence for oscillation of atmospheric neutrinos". In: *Phys. Rev. Lett.* 81 (1998), pp. 1562–1567. arXiv: `hep-ex/9807003 [hep-ex]`.

[31] Takaaki Kajita. "Atmospheric neutrinos". In: *Adv. High Energy Phys.* 2012 (2012), p. 504715.

[32] B. Aharmim et al. "Combined Analysis of all Three Phases of Solar Neutrino Data from the Sudbury Neutrino Observatory". In: *Phys. Rev.* C88 (2013), p. 025501. arXiv: `1109.0763 [nucl-ex]`.

[33] B. Aharmim et al. "Determination of the ν_e and total ^{8}B solar neutrino fluxes with the Sudbury neutrino observatory phase I data set". In: *Phys. Rev.* C75 (2007), p. 045502. arXiv: `nucl-ex/0610020 [nucl-ex]`.

[34] S. Abe et al. "Precision Measurement of Neutrino Oscillation Parameters with KamLAND". In: *Phys. Rev. Lett.* 100 (2008), p. 221803. arXiv: `0801.4589 [hep-ex]`.

[35] Bhabha H. J. and Heitler W. "The passage of fast electrons and the theory of cosmic showers". In: *Proceedings of the Royal Society of London A: Mathematical, Physical and Engineering Sciences* 159.898 (1937), pp. 432–458. ISSN: 0080-4630. eprint: `http://rspa.royalsocietypublishing.org/content/159/898/432.full.pdf`.

[36] Alexander Radovic. *Joint Experimental-Theoretical Physics Seminar at Fermilab on Latest Oscillation Results from NOνA.* Jan. 2018.

[37] Biswajit Adhikary, Ambar Ghosal, and Probir Roy. "mu tau symmetry, tribimaximal mixing and four zero neutrino Yukawa textures". In: *JHEP* 10 (2009), p. 040. arXiv: `0908.2686 [hep-ph]`.

[38] P. Adamson et al. “The NuMI Neutrino Beam”. In: *Nucl. Instrum. Meth.* A806 (2016), pp. 279–306. arXiv: `1507.06690 [physics.acc-ph]`.

[39] S. Shukla, J. Marriner, and J. Griffin. “Slip stacking in the Fermilab Main Injector”. In: *eConf, C960625:ACC015* (1996).

[40] D. Kalra. *NOνA Internal Technote no. 22328, 2017: Optimization of neutrino flux using NOνA target design.*

[41] Robert Miles Zwaska. “Accelerator Systems and Instrumentation for the NuMI Neutrino Beam”. PhD thesis. Texas U., 2005.

[42] D.S. Ayres *et al. The NOvA Technical Design Report.* Tech. rep. Oct. Fermilab Publication, 2007, pp. 25, 30, 31, 35, 36, 37.

[43] L. Mualem. “Apd test board v.2 operation.” In: *NOνA Internal Note 40, version 1* (2007).

[44] D.F. Friend and NDUG Block. “MUON Catcher and Mini-Block Transport Layouts”. In: *NOνA Collaboration Internal Document 9238-v5* (2013).

[45] J.W. Cooper. “CD-4 Closeout Project Overview Presentation”. In: *NOνA Collaboration Internal Document 12152-v1* (2014).

[46] K. Kephart. “Near Detector Under Ground (NDUG) Parameters”. In: *NOνA Collaboration Internal Document 9860-v2* (2014).

[47] Jaroslav Zálešák et al. “The NOνA Far Detector Data Acquisition System”. In: *Journal of Physics: Conference Series* 513.1 (2014), p. 012041.

[48] A. Norman. “NOνA DAQ Data Formats - Definitions”. In: *NOνA Collaboration Internal Document 4390* (2009).

[49] Jrg S. Martin Ester Hans peter Kriegel and Xiaowei Xu. “Density-based algorithm for discovering clusters in large spatial databases with noise, pages 226–231.” In: *AAAI Press* (1996).

[50] Michael D. Baird. “A Side By Side Comparison of Slicer, Cosmic Slicer, and Slicer4D”. In: *NOνA Collaboration Internal Technote no.9197, version 2* (2013).

[51] Brian Rebel. “Cosmic Ray Tracker”. In: *NOνA Collaboration Internal Technote no.4855* (2013).

[52] R. Fruhwirth. “Nucl.Instrum.Meth. A262 (1987) 444.” In: ().

[53] M. Regler and R. Frhwirth. “Reconstruction of charged tracks, Techniques and Concepts of High-Energy Physics V, edited by T. Ferbel”. In: *NATO ASI Series Vol. 20, pp. 407–499, Springer US* (1990).

[54] Nicholas J Raddatz. “KalmanTrack Technical Note”. In: *NOνA Internal Technote no. 13545* ().

[55] Nicholas Jacob Raddatz. “Measurement of Muon Neutrino Disappearance with Non-Fiducial Interactions in the NOνA Experiment”. PhD thesis. Minnesota U., 2016.

[56] William G. Jacoby. “LOESS: a nonparametric, graphical tool for depicting relationships between variables”. In: *19 (Dec. 2000), pp. 577–613* (2000).

[57] C. Backhouse and A. Radovic. “The Attenuation and Threshold Correction of the NOνA detectors”. In: *NOνA Internal (Private) Document, DocDB-13579, page 52* (2015).

[58] C. Backhouse and A. Radovic. “The Attenuation and Threshold Correction of the NOνA detectors”. In: *NOνA Internal (Private) Document, DocDB-13579, page 52* (2016).

[59] L. Vinton. “Calorimetric Energy Scale Calibration of the NOvA Detectors”. In: *NOνA Internal (Private) Document, DocDB-13579, page 52* (2015).

[60] D. P. Mendez. “Second Analysis Calorimetric Energy Scale Calibration of the NOνA detectors”. In: *NOνA Internal (Private) Document, DocDB-13579, page 53, 57* (2016).

[61] P. Adamson et al. “First measurement of muon-neutrino disappearance in NOvA, pages 53, 71, 77.” In: *Phys. Rev.* D93.5 (2016), p. 051104. arXiv: `1601.05037 [hep-ex]`.

[62] Evan David Niner. “Observation of Electron Neutrino Appearance in the NuMI Beam with the NOvA Experiment”. PhD thesis. Indiana U., 2015.

[63] J. Coelho et al. “Good Data Selection”. In: *NOνA Internal Technote no. 13546-v6* (2016).

[64] Chris Backhouse and Ryan Patterson. “Library event matching event classification algorithm for electron neutrino interactions in the nova detectors”. In: *NOνA Internal docdb-11869* (2016).

[65] C. Patrignani et al. “Chin. Phys. C40.10 (2016), p. 100001. DOI: 10.1088/1674-1137/40/10/100001.” In: *Review of Particle Physics* (2016).

[66] D. Pershey. “MEFinder Tech Note.” In: *NOνA Internal Technote no. 14789* (2015).

[67] K.A. Olive et al. “Review of particle physics. Chinese Physics C38, 090001,” in: *Review of Particle Physics* (2014).

[68] G. Davies. “Pi-zero cross-checks on fa (s15-05-07a).” In: *NOνA Internal Note 13379,version 2* (2015).

[69] C. Backhouse and R. Patterson. “Quick look at michel electrons in the nd and fd(calibration)”. In: *NOνA Internal Note 13340, version 1* (2015).

[70] Matthew Strait. “Muon energy scale systematic”. In: *NOνA Internal Note 20816-v21* (2019).